Fortschritt-Berichte VDI

Gerald Joy Alphonso Sequeira, M. Eng.
Kalyan, Indien

Prediction based activation of vehicle safety systems – A contribution to improve occupant safety by validation of pre-crash information and crash severity plus restraint strategy prediction

Prediction based activation of vehicle safety systems - A contribution to improve occupant safety by validation of pre-crash information and crash severity plus restraint strategy prediction

Dissertation
zur Erlangung des akademischen Grades

Doktoringenieur
(Dr.-Ing.)

von **M.Eng. Gerald Joy Alphonso Sequeira**
geb. am 11.12.1985 in Kalyan, Indien

genehmigt durch die Fakultät für Elektrotechnik und Informationstechnik
der Otto-von-Guericke-Universität Magdeburg

Gutachter:

1. Prof. Dr.-Ing. Ulrich Jumar

2. Prof. Dr. Valentin Soloiu

3. Prof. Dr.-Ing. Thomas Brandmeier

Promotionskolloquium am 02. August 2022

Fortschritt-Berichte VDI

Gerald Joy Alphonso Sequeira, M. Eng.,
Kalyan, Indien

Prediction based activation of vehicle safety systems – A contribution to improve occupant safety by validation of pre-crash information and crash severity plus restraint strategy prediction

VDI verlag

Sequeira, Gerald, M. Eng.

Prediction based activation of vehicle safety systems – A contribution to improve occupant safety by validation of pre-crash information and crash severity plus restraint strategy prediction

Fortschritt-Berichte VDI, Reihe 12, Nr. 817. Düsseldorf: VDI Verlag 2022.

170 Seiten, 46 Bilder, 26 Tabellen.

62,00 EUR / VDI-Mitgliederpreis: 55,80 EUR

The world of transportation is rapidly changing with the introduction of partial autonomy in vehicles and the race between the manufacturers to produce a fully automated passenger vehicle. In addition, to enhance driving comfort and reduce the driving workload, these automated vehicles are also visualized as an approach to reduce the majority of accidents that are caused by human errors. However, accidents do happen and there are also some likelihoods that these automated vehicles might fail. Especially in the initial introductory years, which highlights the need for passive safety systems in safeguarding the occupants. These vehicles typically employ forward-looking sensors for the perception of the surrounding environment, which presents an opportunity to use the information from these sensors to predict an upcoming inevitable crash and further estimate the passive safety action required for the predicted crash in the pre-crash phase. This work presents an approach to activate the vehicle safety systems based on the precrash prediction.

Acknowledgement

IV

Contents

Abstract

The world of transportation is rapidly changing with the introduction of partial autonomy in vehicles and the race between the manufacturers to produce a fully automated passenger vehicle. In addition, to enhance driving comfort and reduce the driving workload, these automated vehicles are also visualized as an approach to reduce the majority of accidents that are caused by human errors. However, accidents do happen and there are also some likelihoods that these automated vehicles might fail. Especially in the initial introductory years, which highlights the need for passive safety systems in safeguarding the occupants. These vehicles typically employ forward-looking sensors for the perception of the surrounding environment, which presents an opportunity to use the information from these sensors to predict an upcoming inevitable crash and further estimate the passive safety action required for the predicted crash in the pre-crash phase. This work presents an approach to activate the vehicle safety systems based on the pre-crash prediction. It focuses on the three major topics namely, crash validation, the geometry-estimation, and the crash severity and restraint strategy prediction. The topic of crash validation is administered by a proposal of a novel contact-based validation sensor along with the experimental investigations for comparison with other sensors. The results from the crash test highlight the time-benefit gained by using the proposed sensor. Additionally, the suggested sensor allows the feasibility to measure the initial position of impact and the dynamic positions of the contact points during the crash. For validation of a crash scenario, these dynamic positions measured using the proposed sensor can be compared to the predicted positions of the contact points based on the geometrical equations. For facilitating the prediction of the positions of these contact points, a unique methodology for estimating the geometry of the opponent-vehicle is developed. Moreover, based on the peculiar crash severity and restraint strategy prediction system discussed in this thesis, the required safety action to safeguard the occupant can be predicted in the pre-crash phase, which is ready to be activated on the validation. The architecture of the crash severity and restraint strategy uses two parallel approaches (vehicle level and occupant level) for robustness. The investigations carried out in this work show the potential of these models in the case of head-on collisions between two similar vehicles. Altogether, the work carried out in the thesis lays a good conceptual, theoretical, and experimental groundwork for introducing these systems in a series application phase.

Kurzfassung

Mit der Einführung teilautonomer Fahrzeuge und dem Wettbewerb zwischen den Herstellern zur Entwicklung eines vollautomatisierten Personenkraftwagens verändert sich die Welt des Verkehrs rasant. Um den Fahrkomfort zu erhöhen und die Arbeitsbelastung des Fahrers zu verringern, werden diese automatisierten Fahrzeuge auch als Ansatz zur Verringerung der meisten Unfälle gesehen, die durch menschliche Fehler verursacht werden. Nichtsdestotrotz können Unfälle geschehen, beispielsweise durch einen Ausfall dieser autonomen Systeme, was vor allem in den ersten Jahren der Einführung durchaus wahrscheinlich sein kann. Dies unterstreicht die Notwendigkeit passiver Sicherheitssysteme zum Schutz der Insassen auch bei teil- bzw. vollautonomen Verkehr. Diese Fahrzeuge verwenden in der Regel vorausschauende Sensoren für die Wahrnehmung der Umgebung, was die Möglichkeit bietet, die Informationen dieser Sensoren zu nutzen, um einen bevorstehenden unvermeidlichen Unfall vorherzusagen und die für den vorhergesagten Unfall erforderlichen passiven Sicherheitsmaßnahmen in der Phase vor dem Unfall abzuschätzen. In dieser Arbeit soll ein Ansatz zur Aktivierung der Fahrzeugsicherheitssysteme auf der Grundlage der Vorhersage vor einem Unfall vorgestellt werden. Die Arbeit konzentriert sich auf die drei Hauptthemen Crash-Validierung, Geometrie-Schätzung und Vorhersage der Crash-Schwere und Rückhaltestrategie. Das Thema der Crash-Validierung wird durch einen Entwurf eines neuartigen kontaktbasierten Validierungssensors zusammen mit den experimentellen Untersuchungen zum Vergleich mit anderen Sensoren behandelt. Die Ergebnisse aus dem Crashtest verdeutlichen den zeitlichen Vorteil, der durch den Einsatz des vorgeschlagenen Sensors erzielt wird. Darüber hinaus ermöglicht der vorgeschlagene Sensor die Messung der anfänglichen Position des Aufpralls und der dynamischen Positionen der Kontaktpunkte während des Aufpralls. Zur Validierung eines Aufprallszenarios können diese mit dem vorgestellten Sensor gemessenen dynamischen Positionen mit den auf der Grundlage der geometrischen Gleichungen vorhergesagten Positionen der Kontaktpunkte verglichen werden. Um die Vorhersage der Positionen dieser Kontaktpunkte zu erleichtern, wird eine neuartige Methodik zur Schätzung der Geometrie des gegnerischen Fahrzeugs entwickelt. Darüber hinaus kann auf der Grundlage des in dieser Arbeit erörterten Systems zur Vorhersage der Aufprallschwere und der Rückhaltestrategie die erforderliche Sicherheitsmaßnahme zum Schutz der Insassen in der Phase vor dem Aufprall vorhergesagt werden, die dann bei der Validierung aktiviert werden kann. Die Architektur der Unfallschwere- und Rückhaltestrategie verwendet zwei parallele Ansätze (Fahrzeug- und Insassenebene), um eine höhere Robustheit zu gewährleisten. Die in dieser Arbeit durchgeführten Untersuchungen zeigen das Potenzial dieser Modelle für den Fall von Frontalkollisionen zwischen zwei ähnlichen Fahrzeugen. Insgesamt bilden die in der Arbeit durchgeführten Arbeiten eine gute konzeptionelle, theoretische und experimentelle Grundlage für die Einführung dieser Systeme in einer Serienanwendungsphase.

X

Chapter 1

Introduction

Road transport is one of the major and effective modes of transport in the world. Ensuring the safety of the road users is of prime importance and the responsibility of the government, non-governmental organizations, and industry. Sadly, road accidents continue to be one of the prominent reasons for the loss of human life. It ranks 8th as the leading cause of death according to Association for Safe International Road Travel (ASRIT). Global statistics suggest about 1.35 million (according to the website of World Health Organisation-WHO) people die worldwide every year, with a life lost every 24 seconds. Additionally, about 20-50 million people suffer from long-term disabilities resulting from severe injuries from a road accident. Europen Union's target (28,500 fatalities) of halving the road fatalities between the years 2000 and 2010 was achieved in the year 2012 [21]. Moreover, though the numbers are reduced in recent years, the reduction is still at an unacceptable higher level than its expected target for the decade. A similar trend is also seen in the data from German road-accidents. In Germany, 3,046 people lost their lives and 65,244 people were severely injured in the year 2019 [22]. The numbers from Europe and specifically from Germany indicate difficulty to meet the target for the year 2020.

Apart from the loss of human life, road traffic accidents also result in physical injuries, psychological and financial losses. This has immediate and long-term consequences on the victims and their families. Owing to these reasons, the governmental bodies from most of the countries including Germany are working towards achieving *Vision-Zero*, i.e. zero deaths due to road fatalities [26]. Most of the accidents (over 90%) are caused by human errors due to overspeeding, overtaking, drunken driving, or driver distraction [27]. According to the Statistisches Bundesamt, inappropriate speed accounts for about 32% and is the prime factor in road accidents with fatalities in Germany. The natural limits to the human ability of perception, information processing, and responsiveness are seen as a major challenge for achieving the above vision [26]. In addition to this, external factors such as environmental conditions (low friction caused by ice, low visibility due to fog and rain, etc.) and insufficient reaction time for the driver will remain a part of road transport. This highlights the need for technological development and the
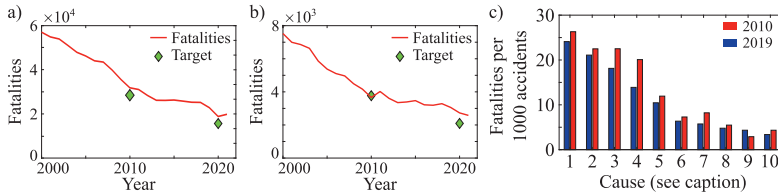
Figure 1.1: Road accident statistics: a) Europe wide statistics for road-fatalities [21], [23], b) German statistics for road-fatalities (the graph is created by using data on page number 55 from [24]), and c) Fatalities by cause of the accident – 1. Inappropriate speed 2. Incorrect road use 3. Overtaking errors 4. Influence of alcohol 5. Improper behavior towards pedestrians 6. Errors when passing 7. Ignoring priority 8. Leaving or entering a road, moving backward 9. Insufficient distance 10. Traveling side by side [25].

introduction of intelligent vehicles with integrated safety systems and automated driving functions. The motivation for the research work presented in the thesis stems from the above-discussed need and it focuses on the three sub-systems of the Pre-Crash Safety System (PCSS) described in Section 1.2.

1.1 History of vehicle safety

In the early 20th century, vehicle safety was mostly associated with the rigidity of the vehicle. In 1937, the Austrian-Hungarian engineer Béla Barényi invented the concept of the crumple zone. He observed that some materials are soft and easy to deform than others and divided the vehicle into three regions, a rigid safety cell or passenger compartment in the middle while the deformable crumple zones at the front and rear to absorb the impact from the crash. Around the 1950s, several researchers and physicians substantiated the benefit of using lap belts through their tests and insisted vehicle manufacturers provide seatbelts. In the year 1958, the three-point seatbelt, which secures both the upper and the lower body of the occupant was invented by Swedish engineer Nils Bohlin. Once the safety benefits of the seatbelts were noticed by the governmental agencies, it became a compulsory regulation for including seatbelts in passenger vehicles. Frontal airbags were offered as optional equipment with additional cost in the 1970s. A decade later, as the cost reduced, frontal airbags were offered as standard equipment in some of the passenger vehicles. Initially, vehicles mainly employed a single central crash sensor in the passenger compartment to detect a crash. The decision to activate the restraint system was made by an algorithm in the airbag control unit, which processes the deceleration signal measured by the sensor. This sensor architecture was termed as single-point sensing since no supplementary peripheral sensors besides the central sensor in the control unit were used for activating the vehicle safety systems.

With the increasing legal requirements like United Nations Economic Commission for Europe (UNECE) or Federal Motor Vehicle Safety Standards (FMVSS) regulations and market-need from voluntary safety rating tests from organizations like New Car Assessment Program (NCAP) and Insurance Institute for Highway Safety (IIHS), automotive manufacturers felt the need for new safety features in addition to the traditional seatbelts and frontal airbags. New safety technologies such as side airbags (curtain and torso airbags) to protect the occupants from side impacts and smart airbags (airbags with several activation stages [28]) which improve occupant safety in frontal collisions were introduced. They brought new requirements and challenges in crash sensing, which were met by using additional sensors, giving it the name multi-point sensing architecture. These additional sensors are usually installed around the central sensor, in the regions which are most likely to undergo deformation during the crash.
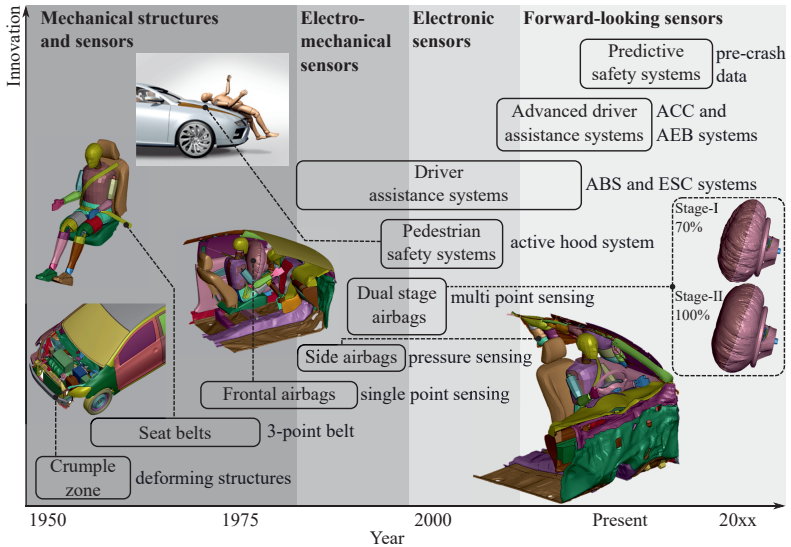
Figure 1.2: Chronology of innovation in the field of vehicle safety.

Simultaneously, the automotive industry found that controlling vehicle dynamics is a supplementary means for increasing vehicle safety. The primary goal of these systems was to assist the drivers and improve their driving comfort, hence called the Driver Assistance Systems (DAS). Anti-lock Braking System (ABS) was one of the first assistance systems introduced in series production by Bosch from the year 1978. ABS continuously monitors the rotating speeds of the wheels. When one of the wheels has a higher rotational speed as compared to others, the

system actuates the valve to increase the braking pressure on that wheel to slow it down. On the other hand, when one of the wheels rotates at a slower speed it reduces the braking pressure so that it catches up with the other wheels. This process of applying and releasing the braking pressure is done intermittently at a rate of about 15 cycles per second. In some years, the introduction of Electronic Stability Control (ESC) increased the safety potential of the DAS by reducing accidents due to the loss of steering control. ESC system continuously compares the driver's steering input with the lateral acceleration of the vehicle, yaw rate, and rotational speeds of wheels. When the actual direction of the vehicle (derived by the comparison parameters mentioned above) does not match with its steering input, ESC detects a probable loss of control, estimates the direction of the slipping or skid, and intervenes by applying brakes to individual wheels in a manner to generate torque in the opposite direction of the skid and thus bringing the vehicle in the driver's intended direction. DAS uses a gyroscope, yaw rate, acceleration, and wheel speed sensors to measure the status of the vehicle which limits its capability to control the instability events related to the vehicle. Figure 1.1 presents the above-discussed history in the form of the chronology of innovations with pictures.

With a substantial reduction in the cost and progress in the forward-looking sensor[1] technology, it was possible to acquire the information about the surrounding road-participants, and led to the development of Advanced Driver Assistance Systems (ADAS). Today's vehicles are already equipped with different systems such as Automatic Emergency Braking (AEB), blind-spot detection, lane assist and lane departure warning, etc. which are categorized into ADAS. These systems work on the information from either one or a combination of forward-looking sensors that scan the surrounding of the vehicle and assist the driver by either supporting in the driving task (steering, braking, and acceleration) or providing information or warnings about a critical driving scenario. The next goal of ADAS is to extend its capabilities to perform tasks related to active safety systems (systems that help to mitigate or prevent vehicle crashes). A step towards this goal has already been accomplished by the introduction of the AEB system, which applies emergency brakes in the case of a sudden appearance of an obstacle in the path of the vehicle and a probable collision is detected. The other option of avoiding an upcoming collision by evasive steering action in combination with braking and acceleration is still in research and development.

With the introduction of the forward-looking sensors, the idea to have information about the crash before the crash happens is now possible. The severity of an upcoming inevitable crash can be predicted based on the pre-crash information

---

[1]The word 'forward-looking sensor' in this thesis is used for a sensor that gives information to predict the forward-in-time or future states of the vehicle's surroundings. Sometimes in literature, these sensors are also termed as 'surrounding' or 'environmental' sensors. Radar, lidar, and camera are the most commonly forward-looking sensors presently used in the automotive industry.

such as velocity, position, orientation, dimension, etc. of the ego-vehicle[2] and the opponent. Based on the predicted severity, the decision about the required passive safety actions can be decided before the crash, and once the crash is validated the required safety action can be deployed. ADAS systems are termed as active systems that continuously monitor the driver's mistakes to avoid a collision, while passive systems such as airbags protect the occupant from injuries of an inevitable crash. Thus enhancing the traditional passive safety system (safety actions such as the deployment of airbags based on sensors measuring after the crash) to a new prediction based safety system is necessary. The ultimate vision of vehicle safety systems is an integration of both active (avoiding an accident) and passive (accident mitigation) safety actions to offer the most beneficial safety.

1.2 Problem formulation

To achieve the overall objective of *Vision-Zero*, technological development through automated driving with earlier information on safety-critical situations is indispensable. The *pre-crash vehicle safety problem* is a decision-making problem to answer the following questions,

- Is safety action required?

- If yes, which safety actions and at what time?

based on the pre-crash information available from the forward-looking sensors and additional sensors for validation. The researchers and industries have approached this problem by defining the architecture and different algorithms of the PCSS. The generic system architecture of a PCSS is suggested in [29]. This architecture, as sketched in Figure 1.3 shows the complete flow from signal acquisition through sensors to the safety actuators through different subsystems such as data fusion and object parameter estimation, inevitability model, crash severity and restraint strategy prediction, etc. included in a Pre-Crash Algorithm (PCA). In contrast to an ADAS system, a PCSS system combines the early recognition of critical driving situations with the safeguarding role of the restraint devices. It receives the raw data from different sensors, processes these data through several algorithms, and then compares the output from these algorithms to decide on the safety actions required.

   The brain of such a system is the PCA, which consists of three sub-algorithm modules in series. The role of the data fusion and object parameter estimation module is to estimate the object parameters such as geometry, velocity, angle of approach and position, the criticality of the object, etc. through the fused data. The parameters of the critical objects are then passed on to the inevitability model and crash parameter estimation, which anticipates the motion of the

---

[2]In this thesis, the word 'ego-vehicle' is the vehicle, which receives and processes the information about the surrounding objects such as vehicles, trees, pedestrians, etc. This information is provided by the forward-looking sensors installed on the ego-vehicle.
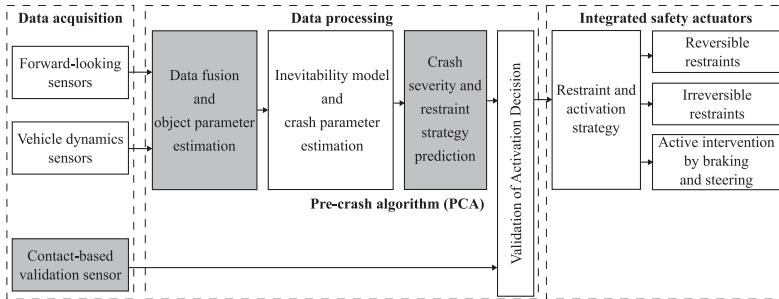
Figure 1.3: Generic system architecture of a pre-crash vehicle safety systems, adapted from [12], [29], [30].

critical objects and decides on the certainty of the crash and the corresponding crash parameters. Based on these parameters, the crash severity and the required restraint system are predicted and forwarded to the decision-making module to activate the actuators for safety action.

1.3 Thesis outline

In addition to the introduction, this thesis consists of a state of the art, three main chapters, and a conclusion. Each of the three main chapters is associated with the three sub-topics from the PCSS, which are marked by grey color in Figure 1.3. The second chapter gives a brief literature review on different sections of vehicle safety systems. It starts with a discussion on the basic passive safety sensors leading to forward-looking sensors and the challenges faced by them. In the next sections, the topics of trajectory planning, opponent-geometry estimation, and crash severity estimation are reviewed. This chapter is closed with the reasoning of the necessity for the research topics described in the main chapters in the summary section.

The third chapter deals with the topic of contact-based validation and the principal design and development of the sensor required for this validation. The *principal design* and *experimental investigation* are the highlights of this chapter. A comparison of the proposed sensor with the other sensors shows the time-advantage gained using the proposed sensor. The potential for improvement in vehicle safety using the proposed sensor is described in the final section.

The fourth chapter presents a *novel methodology to represent the geometry of the opponent-vehicle*. The estimation of the opponent-geometry is broken down into the divisions of arcs and lines along with finding the equations of each arc and line for its representation. Based on the different basic opponent-geometries, a *technique to predict the dynamic behavior of contact point positions* during the crash is given in the next section. The results from the prediction technique are

compared with the measurements from the crash-test explained in Chapter 3 in the fifth section while some conclusions are derived in the last section.

The fifth chapter deals with the topic of crash severity and restraint strategy prediction. At first, the topic of crash severity is introduced. This is followed by an adopted two-step methodology to collect the data for the investigation of different machine learning approaches. The highlight of this chapter is the novel *system architecture description* of the concerned prediction system. Next, the database learning methodologies used for training the *crash severity and restraint strategy prediction models* and their detailed investigations in different phases of prediction are presented. In the end, a probable prediction algorithm is described in the last section.

Finally, in the last chapter, the conclusion of the overall work is presented with the proposal for some insights on possible future work in this direction.

Chapter 2

State of the Art

Abstract

This chapter gives a brief overview of the different methods, principles, and concepts used in diverse fields of vehicle safety systems. In the first section, multi-point sensing architecture is used to describe the different presently used passive safety sensors. This is followed by a detailed review of the forward-looking sensors. The working principle, concepts, and challenges faced by these sensors are discussed in this section. Both sections are summarized by a comparison table highlighting the present capabilities of the sensors. Next, a literature review on the present methodologies used by various researchers in the field of trajectory planning, opponent geometry estimation, and crash severity estimation along with their strengths and limitations are discussed. The chapter is closed by giving a summary of all the topics, which highlights the necessity for validation of pre-crash information and a new methodology for predicting crash severity combined with the information on required safety action, such as the activation of irreversible safety systems like airbags.

Sensors are one of the most important parts of the vehicle safety systems, which provide crucial information based on which the decisions regarding safety actions are taken. A brief history of the vehicle safety systems was given in Section 1.1, which discusses the passive safety systems such as seatbelts and airbags along with their sensor architectures. Elaborating on the different passive safety sensors found in these systems, a comprehensive comparison based on their functioning is outlined at the beginning of this chapter.

2.1 Passive safety sensors

Figure 2.1 shows an example of multi-point sensing architecture for passive safety sensors with the customary positions of different sensor types that are currently used in today's vehicles. In this architecture, along with the central sensor, two additional sensors (one on the driver-side and the other on the passenger-side) are mounted near the crash-box to give early information about the crash for the front-crash detection. These sensors are usually termed Early Crash Sensors (ECS). In

addition to the advantage of the early information, this system can also approximate the position of the impact as driver-side, center, or passenger-side by comparing the signals from the two sensors. These sensors can either be acceleration-based [31] or structure-borne-sound (SBS) based [32], [33]. Acceleration-based sensors measure the sudden and severe deceleration of a car caused by an accident. SBS-based sensor is a more recent development, which can either be used in combination with the acceleration-based sensors or can replace them. These sensors measure the sound (acoustic emissions) generated by the deformation of the structures during the crash. This technology can distinguish between hard and soft crashes and is faster as compared to acceleration-based sensors. In some vehicles, a pressure-hose sensor [34] is installed in the foam material between the bumper-beam and bumper. This sensor is specially tuned to detect low-speed vehicle crashes such as impacts against pedestrians.
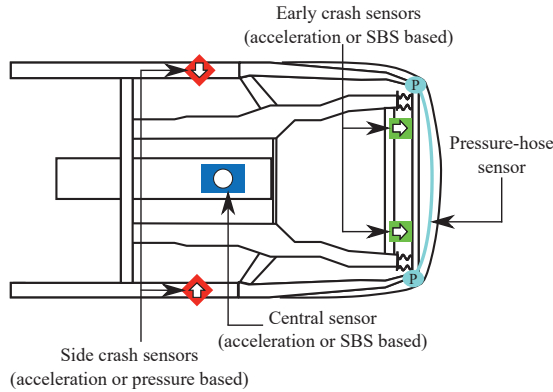
Figure 2.1: An example of the sensor architecture used for detecting vehicle crashes.

Additionally, to detect the impact from the side, two or more sensors are installed in the door structure on either side, which can be acceleration-based [31], pressure-based [31], [35], or a combination of both. For side-crash detection, pressure-based sensors are preferred over their predecessors (acceleration-based side crash sensors) because of their faster response time. These sensors measure the air pressure change in the door cavity caused by the change in volume due to the deformation of door structures.

Based on the signal from these sensors, the crash is classified into basic crash types (front, side, rear, etc.), its severity is assessed, and the decision on the required safety action is taken. Table 2.1 shows the comparison of the various crash sensors presently used in cars. The detection time of present crash sensors is about 7-50 ms depending on the crash-type and the sensor architectures employed. Next,

Table 2.1: Comparison of various sensors used for detecting vehicle crashes.[a]

Sensor type (crash type)	Response time	Advantages	Challenges
Acceleration sensor (front, side, and rear)	15 - 50 ms	• Robust. • Low cost.	• Slow compared to other sensors.
SBS-based sensor (front and rear)	10 - 30 ms	• Fast in some crash scenarios. • Hard and soft crash distinction.	• Variation in SBS of different vehicles.
Pressure sensor (side)	7 - 15 ms	• Fast response time.	• Distinction of different crashes with similar pressure signals.
Pressure-hose sensor (pedestrian)	10 - 15 ms	• Low cost.	• Deterioration from holes or blockage of hose.

[a] Some of the response time values are derived from curves in [32]–[34], [36].

a literature review comprising of the concepts, principles, and challenges faced by the different forward-looking sensors is described in the upcoming section.

2.2 Forward-looking sensors and their challenges

Perception or scanning of the surrounding environment is the first and one of the most essential tasks for future vehicle safety systems. Presently used forward-looking sensors in vehicles are suitable and tailor-made for driver assistance systems. More accurate and reliable information is required for vehicle safety functions indicating the need for more advanced forward-looking sensors. Many studies focus on extending the use of these sensors for different tasks of vehicle safety such as object detection and tracking [37], [38], collision detection and trajectory planning [39]–[41], and crash parameter prediction [42]. In the present automotive technologies and research work, scanning of the surrounding environment is dominated by radar, lidar, and camera sensors. The individual strengths, weaknesses, and limitations of these sensors concerning their ability to scan, detect, and derive important information of the neighboring environment are discussed in this section below.

2.2.1 Radar

A simple radar sensor can be thought of as a device that transmits electromagnetic waves and receives the electromagnetic waves reflected from the surface of the object to determine the velocity, range, and angle of the objects in the surrounding. Based on the requirements of a particular application there are different types of radar sensors. Present-day vehicles employ FMCW-type (Frequency Modulated Continuous Wave) radar sensors with chirp sequence modulation methodology. These sensors send out a sequence of identical chirp signals (a pulse whose frequency changes during transmission) through the transmitting antenna at short intervals. The sample rate of the repetition of a single chirp in the sequence should be high enough (approximately 80 kHz) to neglect the influence of the Doppler frequency for a single chirp. A two-step signal processing technique is employed to separate the range and doppler frequencies. In the first step, a Fast Fourier Transform (FFT) is performed on the data samples of each chirp giving a range vector. In the second step, FFT is performed on range data of the different chirps of a particular sequence to give information about Doppler frequency and thus the velocity. To solve the ambiguity arising from the multiple target reflections, a methodology with a combination of chirps signals with different slopes is explained in [43]. Automotive radar sensors consist of about 4 to 16 antennas to derive the angular information of the object from which the signals are reflected. With the state-of-the-art methodology used in the automotive radar explained above, more detailed information and basic principles about the radar technology can be found in Radar Handbook [44].

Radar sensors are presently used to a wide extent for Adaptive Cruise Control (ACC) function in vehicles [45], [46]. This technology can directly predict the relative velocity through the Doppler effect, which is their significant advantage. Their ability to function even in the most adverse weather conditions gives them another added advantage over the other sensors. Moreover, radar sensors are robust against mechanical failures for the reason that they don't have any moving parts. The present commercial radar technology used in the automotive industry faces the following challenges.

- The lateral position estimation accuracy of radar is generally low. This accuracy is dependent on the angular accuracies of the radar and the distance of the object from the radar. An angular accuracy of $\pm 0.5°$ would result in a lateral uncertainty of 17.45 cm at a 10-meter radial distance [47].

- In some scenarios, multipath reflections might lead to the detection of ghost or false-positive objects [48].

- It is difficult with present commercial radar sensors to estimate additional information of the objects such as size, shape or contour, and classification (passenger cars, trucks, motorbikes, etc.). Radar perceives the size of the objects in terms of Radar Cross-Section (RCS), which is a measure of ease to

11

detect a particular object using radar. Two vehicles of the same size can have different RCS which leads to uncertainty in the prediction of the physical size of the object.

- With an increase in the usage of radar sensors in vehicles, there is a concern over the interference by the number of sensors functioning in proximity to each other [49], [50].

Some of the presently used automotive radar sensors with their characteristics are listed in Table A.1 of Appendix A. These sensors are divided into long-range, mid-range, and short-range based on the maximum distance (range) up to which they can measure.

2.2.2   Lidar

Lidar uses a principle based on the time-of-flight of the reflected laser beams to measure the distance of the points on the surface of the objects from where the beams are reflected. Usually, in automotive applications, there are several objects in the surrounding (detection area) which is resolved by using multiple beams and a scanning mechanism that distributes these beams equally in the required field of view of scanning over a short measurement cycle. The most famous approach of scanning mechanism (used by Velodyne Inc. [51]) is to use a spinning mechanism that rotates the sensor at a high speed to cover the complete 360 degrees field of view. In a race to reduce the cost and size, some promising scanning approaches have emerged. In one approach [52], the sensor uses a micro-electromechanical (MEM) based mirror spinning system which directs the laser beam in different directions. Another approach is to use an optical phased array (a series of antennas with phase shifters). In this technology, the phase of one antenna is adjusted relative to the others for steering the laser beam [53]. With this technology, the laser beam can be steered in a specific manner in a two-dimensional space to concentrate on specific regions in the field of view of the sensor. Lidar sensor with this technology is recently developed by a California-based company Quanergy Systems.

Lidar sensors are presently used in premium cars for obstacle detection, collision mitigation, parking assist, etc. The main advantage of lidar is the 3-dimensional representation of the object in the form of a point-cloud, from which the shape, contour, and size of the object can be estimated. The angular resolution of lidar sensors is around 0.1 degree [46], which yields better lateral accuracy compared to that of radar technology. Some experts perceive lidar technology as one of the key requisites for future autonomous vehicles. It also has an advantage in classifying objects into different groups or classes. Like radar, lidar cannot directly measure the relative velocity but this parameter can be calculated by differentiating the position measured from different two consecutive time stamps. The major concerns of the present lidar sensors for the automotive industry are listed below.

- The main limitation of lidar sensors is degradation in their detection performance during adverse environmental conditions such as snow, rain, fog, dust, and dirt [54], [55]. Dense fog particles, large rain droplets, and snowflakes reflect the laser beam and block these beams from reaching the surrounding object's surface. The opponent-object can hide behind the detection-layer of these environmental factors which blinds the view of the lidar sensor. This can result in a dangerous driving situation. Additionally, direct sunlight on the sensor can cause disturbances in detection.

- The range of lidar sensors is limited by the power of the emitted laser beam, which is mainly restricted by the regulations for eye-safety [46]. There are usually two main light sources, one with 1550-nm wavelength sources that can function at longer ranges (by using higher power) without comprising eye-safety but is costly. The range for the other 905-nm wavelength sources is limited by the eye-safety regulations.

- The perception of lidar technology greatly depends on the reflectivity of the object's surface, which conveys the amount of light reflected in relation to the light incident. The dark-colored surface reflects less light as compared to the light-colored surface. Most of the commercial lidars can see up to 200 meters. But, can they detect a dark color object in the far-field?

- Present-day lidar technology is too expensive for its application in mass-produced commercial passenger vehicles and hence their use is limited to some premium vehicles and research.

Table A.2 compares the performance of some available lidar sensors in terms of range with its accuracy, field of view with its resolution, and cycle time. Solid-state sensors are a recent development over the traditional mechanical rotating sensors, which improves the robustness of lidar sensors to mechanical vibrations and shocks but have a limited field of view.

2.2.3 Camera

Camera systems are the only forward-looking sensors that can perceive the surrounding environment similar to the human eye. A simple camera consists of three units, namely, lens, image sensor, and processing unit. The light from a scene falls through the lens on the image sensor which converts the light photons on every pixel into an electronic signal which is transformed by the processing unit into pixelated image data. Presently in the automotive field, different camera technologies developed for other applications are being explored. A complete 360-degree field of view is possible by stitching together images from 4 or more cameras installed at different angles. A 360-degree surround-view monitor is presently provided in vehicles as an aid to the driver during parking but in the future, this technology

can be employed for object detection and its parameter extraction. A stereo camera is another technology that gives information on the depth (distance or range) based on the parallax image generated by using two cameras.

Camera systems have the potential to detect surrounding objects and estimate their position with the help of advanced image processing, machine learning, and artificial intelligence techniques. This technology has a distinctive sensing capability to recognize and differentiate the colors of an object, similar to human vision. Reading road signs, speed-limit, and detecting lane markings for lane-assist are some of the important tasks currently carried out by camera systems in today's vehicles. Even though camera systems have a big advantage due to their low hardware cost, there are some limitations and challenges to these systems. These are mentioned below.

- Camera systems require adequate lighting to capture clear images for their processing. These sensors face difficulty from low lighting conditions during the night. Furthermore, excessive light from the sun or the headlight of the opposite vehicle can obscure the camera images.

- Similar to the lidar sensor, adverse weather conditions can also degrade the viewing capabilities of the camera system. Even the small snowflakes directly in front of the camera can hide comparatively larger objects situated in the far-field. Heavy rain and dense fog can significantly reduce the range of the camera (analogous to problems faced by the driver in these conditions).

- The techniques such as image processing, machine learning, and artificial intelligence applied to extract useful information from the camera images require large computational resources.

- The longitudinal position (a position of an object in front of the vehicle) is estimated using the laws of linear perspective. The accuracy of this estimation is very less compared to radar and lidar sensors.

- The relative velocity has to be estimated by a two-step process, the first step is to estimate the relative position from the image perspective, followed by the differentiation of the positions from the two successive frames. This two-step increases the error in estimation through the accumulation of errors introduced by each step.

An overview of the camera systems currently used in vehicles is presented in Table A.3. There are different camera technologies under research such as night vision, infrared, stereo, and surround-view for their different strengths.

Table 2.2 summarizes the capabilities of the present forward-looking sensors. Presently, the best accuracy in range ($\pm$ 2 cm) is provided by the lidar sensors. The spinning mechanism type lidar sensor has the feasibility of providing a complete 360-degree horizontal field of view, which can be applied for object detection and tracking but the rotation increases the cycle time. The maximum range

Table 2.2: Comparison of various forward-looking sensors presently used in automotive applications.[b]

Comparison Parameter		Radar	Lidar	Camera
Range / distance [m]	Accuracy	0.1 to 1.8	0.02 to 0.1	0.1 to 5
	Minimum	0.2 to 1	0.4 to 1	2.5 to 120
	Maximum	5 to 320	13.5 to 250	10 to 150
Cycle time [ms]		30 to 72	10 to 66.6	22.2 to 50
Field of view [degree]	Horizontal	12 to 150	27 to 360	40 to 100
	Vertical	5 to 84	6.4 to 40	28 to 48
Relative velocity		Direct measure	Indirect measure	Indirect measure
Color recognition and differentiation		Not possible	Not possible	Possible
Target dimensional representation		2D/3D/4D	2D/3D	2D/3D
Weather influence (Fog, rain, day/night, etc.)		least	high	high
Cost		Medium	Costliest	Least

[b] The values for the comparison parameters are chosen from the tables for each sensor in Appendix A which are summarized from different datasheets and documents [51], [56]–[71]. Note that the term accuracy in the above table is the amount of uncertainty in the range measured.

capability (how far a sensor can see) is higher for radar sensors, while the short-range radar sensors offer the best possible minimum range of 0.2 meters (how close to an ego-vehicle a sensor can see). Moreover, adverse weather conditions have the least effect on radar sensors as compared to the other two sensors. With the recent improvement in the elevation values, the upcoming radar sensor can provide 4-dimensional (3-spatial coordinate values along with the radial velocity) data [56]. Camera sensors are the cheapest and the only sensor which can be used to distinguish between different colors. Using the stereo technique, it is possible to get the range information (spatial distance of the object from the ego-vehicle), but the accuracy reduces as the object is far away from the ego-vehicle [67], [68]. It should be noted that there is a trade-off between values of the different parameters listed in Table 2.2. For example, the lidar sensor with a 360-degree horizontal field of view has a limitation of 50 ms on cycle time based on the maximum rotation rate of 20 Hz. For this reason, a particular sensor cannot deliver the best possible values for all the parameters listed above.

A lot of research is going on to overcome the above-mentioned weaknesses or to

improve the functioning of these sensors. This first group of the research work is focused on investigating the sensor parameter, for e.g. parameters of radio waves chirp emitted in radar [72], [73] and varying the laser-beam principles used in lidar sensor [74]. Some researchers are striving to find new features, approaches, and data processing methods to extract useful information, for e.g. detection of vehicle-tire and pedestrian signatures using the micro-doppler effect [75], [76]. Others are trying to understand the behavior of degradation in sensor data due to different environmental conditions to filter out these effects and improve the detections [77], [78]. In addition to concentrating on improving individual sensors, it is important to discover ways to make the overall system robust. Many believe that a higher level of autonomy in the automotive field can be achieved using the best available information from each sensor and ignoring the degraded one, the so-called 'Sensor Fusion'. The above-discussed approaches would help in the detection and better recognition of an obstacle in the surrounding (i.e. whether an obstacle exists or not?) at some distance away from the ego-vehicle. But the ego-vehicle and in some cases the opponent (if it is another vehicle, cyclist, etc.) can move and change its position, orientation and velocities. Hence, estimating the state of the objects in the future based on their states detected by the forward-looking sensors and possible trajectories or paths is required for predicting an upcoming crash and estimating its parameters.

2.3 Trajectory planning
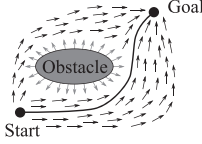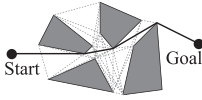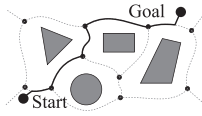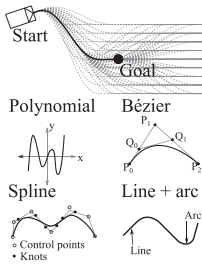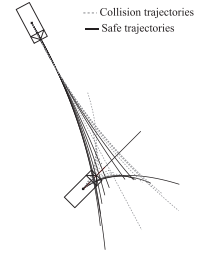
The trajectory planning problem has its roots in the field of robotics, where the choice of the path of the autonomous driving robot is made. An overview of the different basic methods used in the robotics field can be found in the textbooks [79]–[81]. In these approaches, the path between the starting-point and the end-point (goal) is calculated using different methods. One of the earliest methods developed, inspired by the electric charges concept, is a potential field method [82], where an objective function is defined that represents the space in potentials. A large potential is given to the space occupied by the obstacles compared to the vacant space and thus a path of low potential is preferred. Virtual force fields [83] and field vector histograms [84] are further enhancements of this method. Another group of methods is roadmap based, where the problem of planning is reduced by overlaying a roadmap in the space. The Visibility Graph is one of the approaches used by researchers to find the shortest path avoiding the vertices of the polygonal shapes which represent the different obstacles [85]. The Voronoi Diagram is another approach, where a plane (2-D space) containing the number of objects is divided into several convex polygons containing only one object. With this approach, a roadmap is built where the polygons specifying the maximum possible distance between two obstacles (consider the vertices of the polygons as points of maximum distance between obstacles) help to find the shortest collision-free path [86], [87]. Alternatively, other approaches use different basic geometries

such as polynomials [88], Bézier curves [89], spline curves [90], a combination of lines and circles [91], etc. for calculating different trajectories. The desired collision-free path is chosen based on the cost functions which identify the best possible trajectory.

In all these methods, the collision avoidance decisions are based on either the present positions of the obstacles (measured through different forward-looking sensors) or by predictions based on tracking the present and previous positions of the obstacles. Moreover, the trajectories generated do not include the physical limitation and vehicle dynamics behavior of the passenger vehicles [92], [93]. Hence, these methods are limited to path planning applications with lower safety requirements. For a pre-crash system possessing the choice of different vehicle safety actions in a short duration of time, consideration of vehicle dynamics is of utmost importance. Complex multi-body vehicle models are limited by the restricted vehicle dynamic calculations of the ego-vehicle in real-time [94]. One of the reasons for this is the lack of parameters required by the complex model of the opponent-vehicle due to limited information from the forward-looking sensors. The complexity of the vehicle dynamics models can be reduced by using a single-track or bicycle model [95]. Even though the single-track model is simple to implement in real-time applications, it is not suited for pre-crash applications due to limitations in representing the vehicle's lateral dynamics. Thus, a modified vehicle dynamics model for predicting the vehicle motions is required. Such a model is described in [12], which calculates the longitudinal and lateral movement of the vehicle based on its lateral and longitudinal accelerations, velocity, and vehicle-specific parameters such as mass, wheelbase, etc. In this model, the longitudinal and lateral accelerations are physically limited by Kamm's Circle principle. The model was used in this study to investigate the minimum time required of avoiding the collision for vehicle-to-vehicle side crash scenarios. This model is presently in future developmental stages at "CARISSMA Institute of Safety in Future Mobility, Technische Hochschule Ingolstadt" for investigating its use in predicting crash parameters in the cases of inevitable crash scenarios.

Consider a driving scenario as shown in Figure 2.2a, where an ego-vehicle (shown in purple color) and the opponent-vehicle (shown in grey color) are approaching each other. The light blue area represents the front scanning area of a particular forward-looking sensor. The dotted curves show the predicted trajectories (trajectories are anticipated using vehicle dynamics models that employ the combination of vehicle action braking, acceleration, and steering) of both the ego and opponent vehicles respectively. The dotted ellipse represents the boundary of the possible region where the vehicle can be situated in the future after some time δt. At this state of time, it is still ambiguous whether a collision would take place in the future. This ambiguity is resolved at a later state represented by Figure 2.2b, where all the trajectories of both vehicles confirm that the crash is inevitable. However, even at this state of time, the different possible trajectories will give different positions P of the initial contact point and the relative approach angle α_{ra}. In addition to the velocities, the crash severity of an ego-vehicle against

Table 2.3: Summary of the literature related to trajectory planning. Box with triangle represents a vehicle, shapes filled with grey color represent obstacles, solid black lines represent the chosen path, and grey dotted lines represent the possible trajectories (except in the last row).

Method	Description	Pictorial representation	Literature
Potential field	Path with low potential chosen		[82]–[84]
Visibility Graph	Shortest path joining the obstacle vertices		[85]
Voronoi Diagram	Shortest path thorough the points with maximum distance between obstacles		[86], [87]
Geometry based trajectories	Selection of the path based on the cost-functions for different trajectories		[88]–[91]
Trajectories based on vehicle dynamics	Vehicle dynamics based equations predict different possible trajectories		[12]
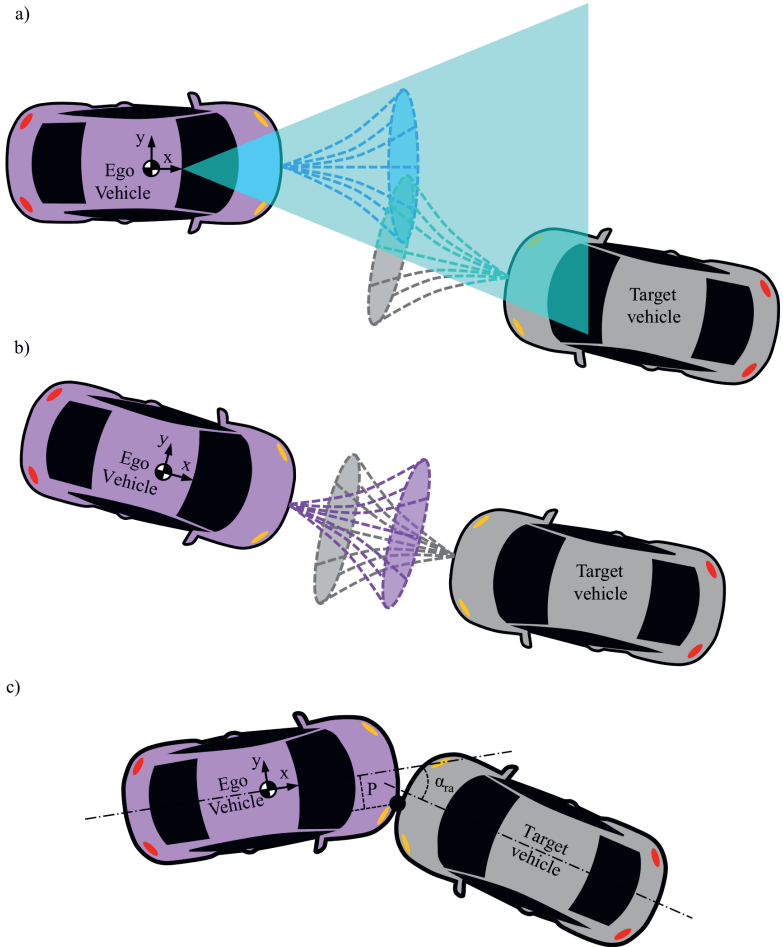
Figure 2.2: A driving scenario with two approaching vehicles: a) opponent-vehicle in far-field - collision avoidance possible, b) opponent-vehicle in near-field - collision inevitable, and c) vehicles contact with each other, (purple color represents ego-vehicle, grey color represents opponent-vehicle, and light blue color shows the front scanning area of the ego-vehicle).

a particular opponent also depends on P and α_{ra} [10], [11]. Consequently, the decision of the safety strategy to be deployed depends on P and α_{ra}. Figure 2.2

describes a state where both vehicles establish contact with each other. At this time, the exact values for P and α_{ra} can be measured to validate the predicted values and take a decision on the required safety action.

The integrated safety system is designed to estimate the crash parameters in the near-field (about 2 to 10 meters), just before the crash. The estimation in the near field helps to narrow down the possible variation in the crash parameters and thus the required safety systems to be deployed for the upcoming crash. But still, there can be ambiguity between two or more required safety actions (deploy driver airbag, deploy both driver and passenger airbags, deploy driver and left-side curtain airbags, etc.).

2.4   Opponent geometry estimation

Opponent geometry representation is another vital information that is required for making crash inevitability decisions during trajectory planning and crash parameter estimation. The basic requirement for geometry estimation is the availability of point cloud data of the object whose geometry is to be estimated. Camera systems cannot provide precise depth information, which makes them ineffective to estimate the detailed geometry of the opponent objects such as the front-contour of the vehicle. Radar and lidar sensors can provide the data required for estimating the detailed geometry of the opponent-object. Since the vehicle as an opponent object composes of one of the most complex geometry, a significant amount of studies in this field focus on estimating the opponent-vehicle geometry. An approach to fit an oriented bounding box and estimate the width, length, and position of the opponent-vehicle using a radar sensor is presented in [96]. In [97] the potential of the radar sensor to estimate vehicle contour through a heat-map is investigated. Even though radar sensors are competent to estimate the geometry of the vehicle, the point cloud data produced by the lidar sensor gives a more precise sense of the shape transition. Hence most of the studies on the investigation of vehicle geometry estimation use lidar point cloud data. A general overview of different approaches used for geometry estimation is demonstrated in Figure 2.3 and explained in the following paragraphs.

The point cloud data generated by the sensors require a specific methodology for estimating vehicle geometry. This methodology forms the basis of the vehicle-geometry estimation. The approach of fitting a rectangular box enclosing the cluster of point clouds from a particular object, the so-called 'Bounding box', can be considered as a stepping stone towards estimating the geometry of the opponent-vehicle. The simple bounding box approach does not consider the orientation of the opponent-vehicle and leads to erroneous geometrical parameters. Hence, an oriented bounding box approach that takes into account the orientation of the opponent-vehicle is usually considered for estimating the opponent-vehicle parameters such as length, width, etc. In [98] and [99], an L-fit (L-shape formed by two perpendicular lines representing the front and a side of the vehicle) based
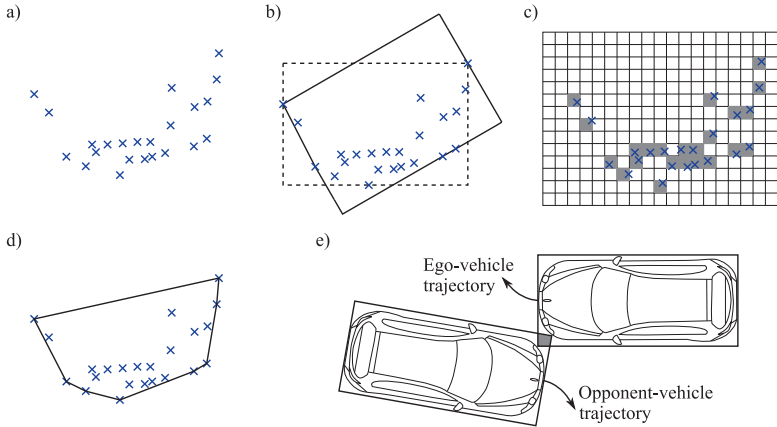
Figure 2.3: Different vehicle geometry estimation approach: a)an example of the point cloud from vehicle front, b) Bounding box (dotted line) and oriented bounding box (solid line) approaches c) Occupancy-grid based approach, d) Convex hull based approach, and e) False-positive contact-detection through oriented bounding box approach.

approach for fitting an oriented bounding box is explained, while [96] discusses a combination of K-Nearest-Neighbors (KNN) and Density-Based Spatial Clustering of Applications with Noise (DBSCAN) algorithm to cluster the radar data. The clustered data is used to construct an oriented bounding box with minimal area and including all the points of the cluster. In challenging scenarios (visibility of only one side of the vehicle to radar), the oriented bounding box formed using the above methods cannot estimate both width and length accurately. In [100], a template-based approach is suggested for estimating the vehicle geometrical parameters in these challenging scenarios.

Although this oriented bounding box approach is presently used in Advanced Driver Assistance Systems (ADAS) for a rough estimation of geometrical parameters of the vehicle, it is not suitable for pre-crash systems that require finer geometrical details. Consider a driving scenario illustrated in Figure 2.3 where an oriented bounding box approach would indicate collision based on the intersection of the boxes shown by the intersecting grey area. But in the real world, both vehicles would cross each other without any collision due to the curved shape of the vehicles. The requirement of these finer geometrical details motivated researchers to investigate different approaches to estimate them. A two-dimensional occupancy-grid based approach is explained in [101]. In this work, the point cloud representing the shape of the vehicle is mapped on a two-dimensional grid to form an occupancy-based black belt with tolerances representing the shape of

the vehicle. Another technique for estimation of vehicle geometry using convex hull approximations enclosing the lidar point cloud is proposed in [102] and [103]. This method considers the points from the outermost region of the corresponding cluster of point clouds and confines itself by joining adjacent points with straight lines. Considering the individual points in analysis for estimating geometry introduces errors due to fluctuation of the reflection points generated by the sensor noise. A combined behavior of the reflection points should be considered to neutralize the effect of noise. Moreover, the front contour of the vehicle is generally a higher degree curve and a straight line approximation between the points requires a high number of reflection points for better representation. A convex hull methodology gives a large number of line elements, which define the vehicle geometry. Each of these line elements has to be considered for the pre-crash algorithms such as inevitability prediction and crash parameter estimation, which increases the complexity. Hence, a novel methodology that can represent the finer details of the vehicle geometry with less number of geometrical elements is desired by the pre-crash algorithms.

2.5 Crash severity estimation

The prediction of an upcoming inevitable crash and its parameters are not enough, it is also of utmost importance to know its severity and the corresponding passive safety action to safeguard and reduce the occupant injuries before the crash. Present studies in the field of crash severity estimation can be broadly classified into two categories, physical model-based approaches and data-based approaches. Studies on the first approach [104]–[107] use some form of Lumped Parmater Models (LPM – models built using mass, spring, and damper elements) to simulate the physical in-crash response of the vehicle from a particular type of crash. The book on vehicle crash mechanics [104] explains the basics of using the LPM approach for vehicle crash modeling and also describes different models. In [105], regressive models are investigated to estimate the parameters of the LPM-model for vehicle-to-pole crash tests. The output of the LPM model is usually a simplified deceleration signal of the vehicle from the crash based on which the crash severity parameters are calculated. The LPM approach is fast and simple enough to be embedded in the control unit of the vehicle for real-time prediction. But these models usually ignore the rotational movements of the vehicle during the crash.

Many countries record the data from the police reports after the crash in databases such as General Estimates System (GES), Fatality Analysis Reporting System (FARS), and Crash Analysis and Reporting System (CARS) from the United States and German In-Depth Accident Study (GIDAS) from Germany. Most of the studies [108]–[111] implementing the data-based approaches use the information from these databases to train different machine learning methods such as random forest algorithms or neural networks. The focus of these studies is either to identify the factors of severe crashes or to predict the crash or injury severity

in some classes such as (minor, moderate, severe, and fatal). In [112], a logistic regression method is used to predict the probability of fatal occupant injuries, while [113] uses this method to identify the cause of fatal injuries in Iran. The performance of the prediction of the crash severity using data-based approaches is dependent on the accuracy of the data and comprehensiveness of the database to cover all the possible crashes.

2.6   Summary

Early and robust information about an upcoming crash is desired by the vehicle safety systems for a decision on the required safety action. Passive safety sensors discussed in Section 2.1 have limitations in providing information about the crash after some milliseconds. This information is then analyzed and a signal for suitable safety action is triggered. Due to this, a safety action such as airbag deployment can only be activated after this analysis. If the information about the crash and its relation to the required safety action is available before the crash (pre-crash phase), then the safety action can be taken much earlier. This gain in time can be used to increase safety by deploying larger airbags to cover a broader area or controlling the gas inflow inside the airbag (smart airbag).

The forward-looking sensors discussed in Section 2.2 together with the trajectory planning (Section 2.3) have the capability of providing information about the crash (crash parameters such as velocities, the position of initial contact, angular orientation, etc.) in the pre-crash phase. Activation of the irreversible safety systems based on the information measured by the forward-looking sensors is theoretically feasible. However, there is an uncertainty on the exact values of the crash parameters. The first source of this uncertainty arises from the uncertainties and the reliability of the forward-looking sensors. The present forward-looking sensors face many challenges from complex real-world vehicle surroundings. Some of the major challenges and uncertainties for these sensors are tolerances and angular errors, weather influences, ghost objects, multi-reflections, etc. For example, the challenges arising from the harsh weather conditions are illustrated in Figure 2.4. In these conditions, the frames from the camera are hazy or not clear, the lidar sensor is completely blinded by the dense fog and gives less number of cloud points in light fog and rainy conditions, and the disturbances from the rain cause the detection in the near field region difficult for the radar sensor [114]. A brief literature survey on this topic is given in Section 2.2. The other source of this uncertainty comes from the trajectory planning and crash parameter estimation models explained in detail in Section 2.3. Moreover, there are concerns about incidents such as the famous accident caused by Uber's automated driving system in Arizona State of the United States. In addition to this, the forward-looking sensors fail to provide material-related information about objects such as mass and stiffness. A soft-object like a cardboard box or a foam with the same reflection properties will be perceived by the forward-looking sensor also as a critical-object.
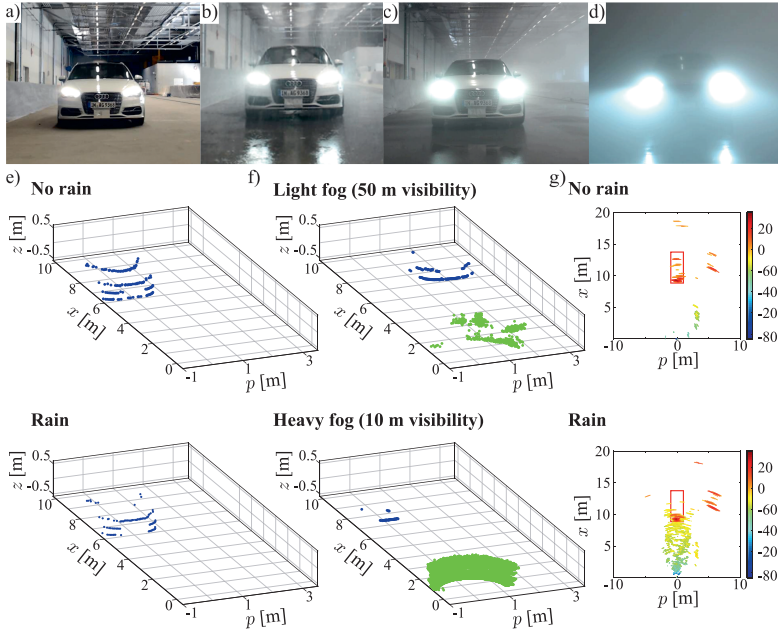
Figure 2.4: Challenges faced by forward-looking sensors in harsh weather conditions: a) Camera frame in normal weather, b) Camera frame in rainy conditions, c) Camera frame in light fog conditions (50 meters visibility), d) Camera frame in dense fog conditions (10 meters visibility), e) effect of rain on the lidar point cloud, f) effect of fog on the lidar point cloud (blue color represents the cloud points from the vehicle, while the green color represents the cloud points from the fog particles), and g) effect of rain on radar signal. This figure is prepared from the results of the tests performed by colleagues working in CARISSMA, Technische Hochschule Ingolstadt [114].

In these incidents of misidentification, a false positive may result in the activation of irreversible safety systems, such as airbags, which can cause an injury to an occupant, while a false negative would result in no action when an action might be required. This highlights the need for robust validation before activating critical vehicle safety systems. This lays down the need and importance of crash-scenario validation. Also, as per the ISO 26262 guidelines, the activation of safety actuators requires the Automotive Safety Integration Level D (ASIL-D) [115]. This level can be achieved by validating the crash parameters predicted by forward-looking sensors with parameters measured using a sensor working on a different

principle. Furthermore, the validation will also provide the required robustness against the false-activation of safety systems. The use of passive safety sensors for validation would neglect the benefit of the pre-crash information and thus a sensor that can provide early information is needed. To fulfill this need, a contact-based validation system that can validate a crash based on mechanical contact (near t_0) is described in Chapter 3.

In addition to the crash inevitability and crash parameter prediction algorithms, a representation of the opponent geometry is also necessary for the validation process. The present methodologies for estimating the geometry of the opponent-vehicle (refer to Section 2.4) lack either the geometric details or have a complicated representation for the task of validation. Hence a new methodology to estimate the geometry of the opponent-vehicle through a combination of simplified geometrical-elements (arc and line elements) has been established. A brief description of this methodology is given in Chapter 4. This methodology also includes the estimation of the angular orientation of the opponent-object with respect to the ego-vehicle.

Prediction of the severity of an upcoming crash is desired by the pre-crash systems to mitigate and reduce the occupant-injuries in case of inevitable crashes. Both the groups of studies associated with the topic of crash severity estimation, discussed in Section 2.5 have some inadequacies. In a particular crash, the severity with which an occupant can be injured is a combination of the physical behavior (deformation, deceleration of the vehicle, etc.) of the crash structure, restraint effect of the safety systems such as airbags and seatbelts, and the occupant kinematics. The group of studies based on the physical-model approach is limited to the vehicle level parameters and misses out on the representation of the behavior of the occupant kinematics and restraint systems required for the decision on activation of airbags. Whereas the available crash database used in the database approaches are from the police reports and the parameters such as the initial position of impact, relative approach angle, the velocity of vehicles, etc. are established based on the police investigation and crash reconstruction. These databases lack the resolution and accuracy of the crash parameters to train the prediction models. Considering this limitation of the present crash database, a two-step Finite-Element simulation-based methodology for generating data along with the structure of the database, its features, and analysis of the data collected for head-on collisions is discussed in Chapter 5. In addition to these, the concepts of the crash-severity prediction models, learning methodologies, and the results from these models are also discussed.

Chapter 3

Validation of Pre-Crash Information

Abstract

This chapter focuses on the validation of pre-crash information and the corresponding sensor developed for this validation. At first, the desired functions for the validation are laid down, followed by basic physical principles, which are of interest for the validation of this information. The concept of the validation sensor consisting of electrical resistance elements, its working principle, different variations, and methodology for validation are the main contributions of this chapter. The robustness and functioning of the sensor are demonstrated by investigating the sensor in different dynamic experiments, the experimental investigation through crash test was a major milestone. In conclusion, the potential of the proposed sensor for improving vehicle safety is presented by comparing it with presently used crash sensors.

Activation of the irreversible safety systems based on the information measured by the forward-looking sensors is theoretically feasible. However, the uncertainty on the values of crash parameters and their sources (discussed in Section 2.6) lays down the need and importance for the validation of these parameters. Validation at the first contact would verify the crash parameter estimation and further reduce the variation and uncertainties in the crash parameters to the accuracy of the sensor used for validation. In addition to the function of detecting a crash, there are other supplementary functions desired by the validation process to assist in the decision of the activation of the irreversible safety systems. Due to the significance of these functions to this chapter, they are listed in the first section.

3.1   Desired functions of the validation process

The main function of the validation process is to confirm that the predicted crash scenario is within acceptable limits and take a decision on the required safety strategy based on this validation. The following parameters must be checked for

the validation of a crash scenario[1].

- Has a crash event occurred?

- Is the predicted position of impact within the acceptable limits?

- Does the predicted relative approach angle fall within the acceptable limits?

- Is the predicted relative velocity within the acceptable limits?

The challenge for the validation is to measure and/or estimate all the above parameters using just one additional sensor for validation. The requirement of limiting the number of validation sensors to one stems from the cost competitiveness in the automotive industry. The most important purpose of the validation is to avoid false activation of irreversible safety actuators, which is fulfilled by ensuring the occurrence of a crash event. In an event of a crash, contact between the vehicle and the opponent is inevitable. Hence, a physical principle that can sense contact during a vehicle crash is an optimal choice for a validation sensor. Additionally, the position of the initial contact point is essential, because the severity of the vehicle crash highly depends on this position [10]. The other two parameters (relative approach angle and relative velocity) can be predicted with great accuracy by applying the data-fusion technique to signals acquired from different forward-looking sensors. Hence, the information on these parameters is considered desirable for the validation sensor.

After having a brief review of the desired functions for the validation process, an overview of the important physical principles which can be used in sensors is a good foundation before the introduction of the proposed validation sensor.

3.2   Underlying physical principles

A sensor in the context of the vehicle system is a component that converts the effects like motion, deformation, contact, etc. into physical quantities that can be measured, usually into electrical signals such as voltage or electric current. There are different physical effects with which the sensing function can be achieved. Some of the physical effects and their principles form the fundamentals of sensing technology. Detailed information about these effects and their relation to the respective sensors can be is given in [116]–[118]. Understanding the important physical principles which are of interest to vehicle-crash validation is an introductory requisite and a brief revision of these principles is described in the below section.

---

[1]A particular crash scenario is defined by the pre-crash information such as initial contact point, relative approach angle, velocities of the vehicle, etc. Therefore, the term 'validation of a crash scenario' can be considered as collective validation of the different pre-crash information required to define the crash scenario
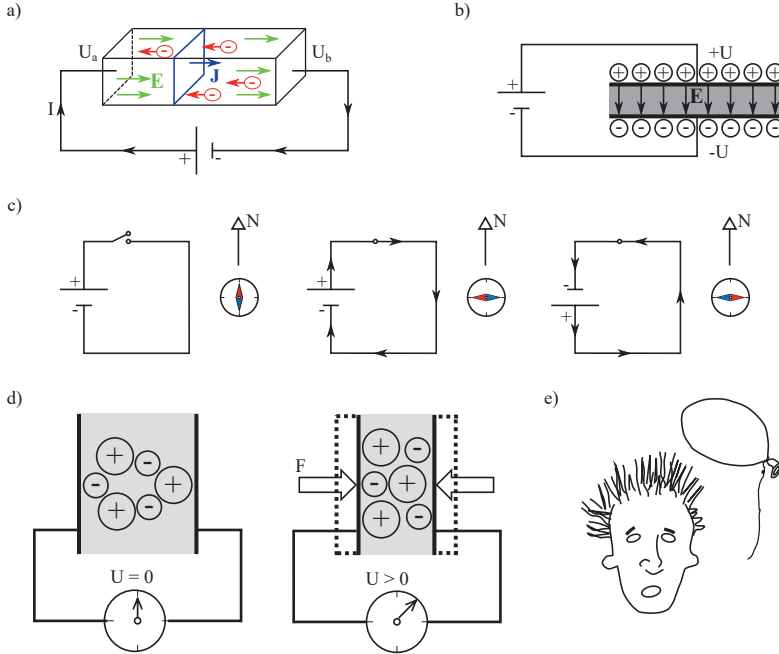
Figure 3.1: Important physical effects for sensing: a) electric current flowing through a material by voltage application, b) charge development on a parallel-plate capacitor, c) demonstration of the electromagnetic effect, d) piezoelectric effect, and e) triboelectric effect.

3.2.1 Electric resistance

Consider a conductor with a uniform cross-section as shown in Figure 3.1a, across which a battery is connected and the two ends of the body are at two different voltage potentials (U_a and U_b). This will set up an electric field E within the material along with corresponding electric force, which causes the free electrons (negative charges) to move from the negative terminal of the battery to the positive terminal. This motion of electrons is termed an electric current (charge flowing through a region per unit time), with the flow or direction of electric current opposite to that of electrons. The material of the bar tends to resist this motion or flow of charges (e.g. in the case of metals the flow of electrons is interrupted by its collisions with ions), which is termed as electric resistance.

The electric resistance of a body or component depends on its material and geometry. The material property which relates to the electric resistance is specific

resistivity ρ and relates electric field $\boldsymbol{E}$ to the electric current density $\boldsymbol{J}$ by Ohm's law in vector form.

$$\boldsymbol{E} = \rho \boldsymbol{J}, \tag{3.1}$$

where ρ is a second-order tensor. $\boldsymbol{E}$ and $\boldsymbol{J}$ are vectors. Resistivity ρ at a particular point in a material can be defined as the ratio of the magnitude of $\boldsymbol{E}$ to the magnitude of $\boldsymbol{J}$ and is given by

$$\rho = \frac{|\boldsymbol{E}|}{|\boldsymbol{J}|}. \tag{3.2}$$

The electrical resistance R of a particular body with uniform cross-sectional area A and length L is described by the resistivity equation as follows

$$R = \rho \cdot \frac{L}{A}. \tag{3.3}$$

The above equation is the fundamental basis for most electrical resistance based sensors. This principle is widely used in displacement sensors, where L corresponds to the linear or angular position. In [119] different sensor designs requiring physical contact are discussed, while [120] describes the contact-free resistance-based sensor concept. Resistance based force and pressure sensors use strain gauges, devices that change their resistance based on the change in $\frac{L}{A}$. Studies [121], [122] discuss more complex sensor concepts, which use a network of resistance elements to define the damage and deformation behavior of advanced non-homogeneous materials such as composites. These complex sensing concepts are suitable for health monitoring applications but have difficulty in detecting the contact position with the required accuracy and robustness for vehicle crash applications.

3.2.2 Capacitance

Capacitance is an effect, which charges two conducting materials by an equal magnitude of opposite charges if they are separated by a dielectric medium and connected to the opposite terminals of the battery (see Figure 3.1b). A device with such a combination of materials is called a capacitor. The capacitor is usually specified in capacitance C, a ratio of the magnitude of the charge q on either of the conductor and the potential difference U between them. It is given by

$$C = \frac{q}{U}. \tag{3.4}$$

Based on the design of the capacitor, the capacitance can be calculated using the general equation

$$C = \varepsilon_0 \varepsilon_r G, \tag{3.5}$$

where G is a geometric factor, which depends on the shape of the two conducting materials and the distance separating them, ε_0 is the electric constant or permittivity of free space and ε_r is the relative permittivity or dielectric constant. Table B.1 in Appendix B gives an overview of some of the basic configurations of a capacitance-based sensor and their equations for the geometric factor. For most of the applications, the change in geometric factor G causes the change in the capacitance of the sensor. Capacitance based sensors are one of the widely used sensors to measure different physical quantities such as force, pressure, distance, acceleration, touch, etc. In [123], a design of a tactile sensor based on the capacitance effect to detect the contact pressure is investigated, while a concept for position detection based on variation in the area is described in [124]. A large number of capacitive sensing grids would be required to cover the region of the vehicle for a particular crash type, thereby increasing the challenge for cost feasibility.

3.2.3 Magnetism and Induction

A magnet is an object that has a special property to attract certain materials such as iron, steel, nickel, etc. Similar to the electric field, a magnet has a magnetic field around it, which is strong near the magnet and weak far away from the magnet. Consider a demonstration shown in Figure 3.1c, if a magnetic compass is brought near a current-carrying conductor, the needle of the compass changes its pointing direction. Now, if the direction of the electric current is changed by interchanging the ends of the conductor connected to the battery, the needle of the compass points in the opposite direction. This demonstration shows that a magnetic field (similar to that around a magnet) is also produced when a current passes through a conductor and its direction is dependent on the direction of the current flowing through the conductor. On the contrary, when an electric charge q moves across a magnetic field $\boldsymbol{B}$ with a velocity $\boldsymbol{v}_q$, it experiences a force $\boldsymbol{F}_{mag}$ and is given by

$$\boldsymbol{F}_{mag} = q \cdot \boldsymbol{v}_q \times \boldsymbol{B}. \tag{3.6}$$

The direction of this magnetic force is perpendicular to the plane formed by $\boldsymbol{v}_q$ and $\boldsymbol{B}$. In most applications, the magnetic field acts as a source to induce an electric current when a force is applied or a body moves.

Induction is the phenomenon by which an electric current is induced in a loop of wire when the magnetic field surrounding it varies with time. According to Faraday's law of induction, the rate of change of magnetic flux ϕ_B is equal to the induced electromotive force $(e.m.f)$ and given by the following equation

$$e.m.f = -\frac{d\phi_B}{dt}. \tag{3.7}$$

The minus sign indicates that the direction of the $e.m.f$ is opposite to the direction of the change in magnetic flux. Usually, such an $e.m.f$ is induced in a coil of wire with n_{loop} number of loops in a coil and the total $e.m.f$ is the addition of $e.m.f$ induced in every loop of wire or in other words given by

$$e.m.f = -n_{loop}\frac{d\phi_B}{dt}. \tag{3.8}$$

The magnetic flux is given by

$$\phi_B = \int\int_A \boldsymbol{B} \cdot d\boldsymbol{A} = \boldsymbol{B} \cdot \boldsymbol{A} = B \cdot A \cdot \cos\theta. \tag{3.9}$$

Substituting equation 3.9 in equation 3.8

$$e.m.f = -n_{loop}\frac{dB \cdot A \cdot \cos\theta}{dt}. \tag{3.10}$$

As described above an electric current flowing through a coil will create a magnetic field around it. If the electric current flowing through the coil varies with time, the magnetic field generated will also vary with time and thus induce an $e.m.f$ in the coil. This phenomenon is called self-induction. The induced $e.m.f$ is proportional to the rate with which the current changes and is given by

$$e.m.f = -L\frac{dI}{dt}, \tag{3.11}$$

where the proportionality constant L is called inductance. Equations 3.10 and 3.11 form the basis for a sensor working on the above principle. These sensors usually measure the change in induced $e.m.f$ caused by moving the source of the magnetic field, changing the orientation of the magnetic field, varying the current flowing through the coil, changing the area by application of external force, or changing the number of turns. [125] and [126] describes a magnetism and induction based position measurement sensor concept respectively. These principles can detect only metallic targets and additionally, the measurement signals are dependent on the type of metal being detected.

3.2.4 Piezoelectric effect

When an external force is applied to some crystalline materials such as quartz, ceramics, polymers, etc., an electric charge is generated across this material. This behavior of these materials is termed as the piezoelectric effect. The external force F applied to the piezoelectric material deforms the crystalline structure of the material, which rearranges the positive and negative charges inside the material and develops an electric charge on the material's surface (see Figure 3.1d). The charge is developed because of the electric polarization within the material and is given by

$$\begin{bmatrix} P_{xx} \\ P_{yy} \\ P_{zz} \end{bmatrix} = \begin{bmatrix} d_{11} & d_{12} & d_{13} & d_{14} & d_{15} & d_{16} \\ d_{21} & d_{22} & d_{23} & d_{24} & d_{25} & d_{26} \\ d_{31} & d_{32} & d_{33} & d_{34} & d_{35} & d_{36} \end{bmatrix} \begin{bmatrix} \sigma_{xx} \\ \sigma_{yy} \\ \sigma_{zz} \\ \tau_{yz} \\ \tau_{zx} \\ \tau_{xy} \end{bmatrix} \tag{3.12}$$

31

where P represents the polarization vector, d matrix represents the piezoelectric coefficient matrix of the piezoelectric material, σ represents the axial stresses and τ represents the shear stresses (note that the subscripts indicate the directions). The electric charge generated q_x in the material is proportional to the applied force F_x and is given by

$$q_x = d_{11} \cdot F_x. \tag{3.13}$$

The material with two electrodes also acts as a capacitor with capacitance C, with a voltage U developed between the electrodes is

$$U = \frac{q_x}{C} = \frac{d_{11}}{C} \cdot F_x. \tag{3.14}$$

This phenomenon is widely used in accelerometers in which a piezoelectric material is sandwiched between a mass-spring system and a casing. The motion of the mass compresses or expands the piezoelectric producing the voltage corresponding to the motion. A general concept of tactile sensors based on the piezoelectric principle is explained in [127], while [128] describes a similar concept applied to vehicle crash detection. This concept can detect a vehicle crash and roughly estimate the impact position as left or right by analyzing the signals from two sensors but it cannot give the exact impact position.

3.2.5 Triboelectric effect

Rubbing a balloon on hair for some time results in the hair sticking up when the balloon is drawn away (see Figure 3.1e). This is caused by the triboelectric effect, a phenomenon of electric charge redistribution between two materials when they come in contact with each other. When a balloon is rubbed on the hair, the electrons from the hair are transferred to the balloon making it negatively charged. The loss of electrons causes the hair to be positively charged and thus the hair is attracted to the negatively charged balloon.

In [129], [130], a combination of the triboelectric effect and electrostatic induction is used to develop Triboelectric generators (TEG) or triboelectric nanogenerators (TENG). These devices have the potential for harvesting mechanical energy from daily human activities, which can be used for self-powered devices. A sensor for monitoring the motion of humans in their sleep is investigated in [131], while a similar sensor to measure human hand motions for smart gloves is studied in [132]. The research work [133] describes a pressure sensor concept using TEG made from a layer of polydimethylsiloxane and another layer of a combination of carbon nanotube and polydimethylsiloxane material. The above studies show that this effect can be applied to sense motions, force, pressure, etc. for applications with smaller sensing regions. The region of interest for vehicle-crash detection applications is comparatively large (the vehicle front region is approximately about 1.5 to 2 meters) and would require a matrix of such sensors resulting in the cost increase.

Table 3.1: Decision matrix for selection of physical principle.

Factor Principle	Ability to realize desired functions	Ease of measurement	Ability to sense before contact	Total points
Electric resistance	4	2	0	6
Capacitance	1	1	1	3
Magnetism and induction	1	1	1	3
Piezoelectric	1	3	0	4
Triboelectric	1	3	0	4

A decision-matrix method is used to choose a physical principle for the validation sensor. Table 3.1 shows the decision-matrix, with three factors considered for the judgment. The first factor is the ability to realize the functions mentioned in Section 3.1, with a point for every function that can be realized by the sensing principle. The electric resistance principle scores a maximum of four points for its feasibility to provide information on all the functions. The other principles can only detect a crash by a change in the measured signal either by contact or by proximity and hence score only a point. These principles would require multiple measuring grids for detecting the position of impact, increasing the cost, and making this detection not feasible for the cost-competitive automotive industry. The second factor considered was the ease of measurement with a scale of three points. The piezoelectric and triboelectric principles score three points due to their ability to directly measure the voltage as the measured signal. The electric resistance principle requires additional electric circuit elements such as shunt resistance to measure the current and hence scores two points. The other two principles need a specially tuned measurement circuit, which increases the complexity for measurement and thereby each scoring a point. The ability to provide information before the first-contact was considered as the last factor. The contact-based sensing principles (electric resistance, piezoelectric, and triboelectric) cannot give information before the contact and score no points, while the other proximity-based sensing principles score a point for this factor. The electric resistance principle scores the maximum points compared to other sensing principles and is considered for the validation sensor.

3.3 Proposed Validation Sensor

Such a sensor can be directly integrated into the outer-skin[2] of the vehicle or can be installed as an additional component of the vehicle as shown in Figure 3.2. A concept to embed such a sensor as an integral part of the vehicle's outer-skin, when it is made from composite material is demonstrated in [2], [3], while [1], [4], [5] describe an approach where this sensor can be produced separately and installed in the vehicle. The choice to select a particular concept is a production optimization problem for vehicle manufacturers to reduce the overall production cost. Both concepts work on a similar principle and a generalized description of the proposed validation sensor is given in the following sections.
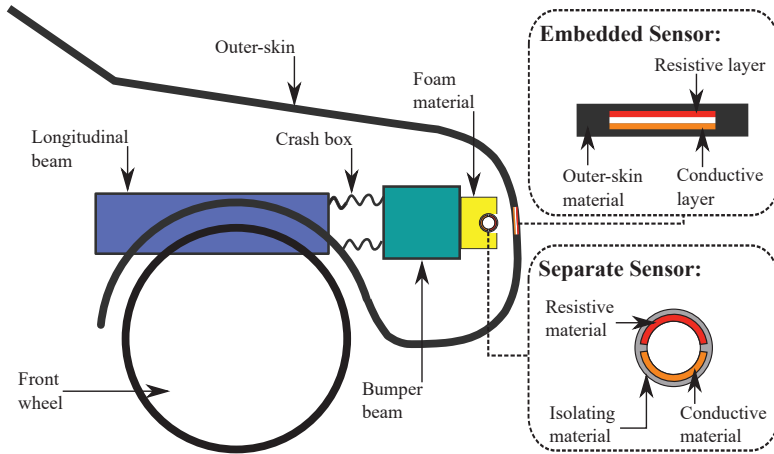
Figure 3.2: Concepts for incorporating validation sensor in a vehicle.

3.3.1 Principal design

The proposed sensor consists of one or more resistance elements electrically isolated from each other as shown in Figure 3.3. At the ends of these resistance elements, electrical contacts are created to connect the sensing part with a measurement circuit. In addition to the choice of integration of the validation sensor, vehicle manufacturers can also modify the size and shape of the sensor suited to their vehicle design and manufacturing facilities. Figure 3.3 demonstrates the sensor conceptualized with a circular geometry as a basic shape. The resistance elements are arranged in segments of this basic shape and based on the number

---

[2]The word 'outer-skin' is used for the exterior surfaces of the vehicle usually made from fiber-reinforced plastics and/or sheet metals

of segments the sensor can be classified into two different types as described below.
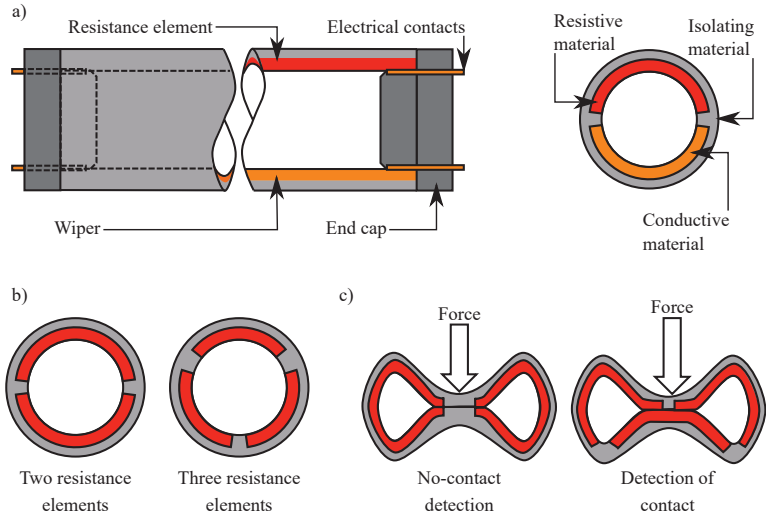
Figure 3.3: Types of validation sensor: a) construction and cross-section of single-resistance element sensor, b) cross-section of multiple-resistance elements sensor, and c) vulnerability of two-resistance elements sensor.

Single-resistance element sensor: As the name suggests, this type of sensor consists of only one resistance element and it works similarly to a voltage divider or potentiometer. This type of sensor requires another element made from a conductive material (shown by the light orange color in Figure 3.3a) to tap the voltage potential at the contact point from the crash. The function of this element is equivalent to the wiper used in a potentiometer and hence this element is named as a wiper. This type of sensor concept is more suitable when the sensor is to be integrated into the vehicle parts and has a base material, which can function as a wiper. When this sensor is manufactured separately, this concept has challenges in the production process to bring together three different materials as one single part. Hence, automotive manufacturers will prefer the concept with the multiple resistance elements when the validation sensor is manufactured separately.

Multiple-resistance elements sensor: The construction of this type of sensor is similar to the single-resistance element sensor concept, except the conductive material of the wiper is replaced by a resistive material to form another resistance element. This type of sensor can also contain more than two resistance elements. The use of the same resistive material for all the resistance elements makes the

manufacturing process simpler as compared to the single-resistance element sensor concept.

The simplest form of a multiple-resistance elements sensor is a two-resistance elements sensor. The two-resistance elements sensor and single-resistance element sensor are vulnerable to no-contact detection if the contact force is in the separation region of the elements and perpendicular to it (see Figure 3.3c). Hence, the separation region should be kept as small as possible. Additionally, during the installation of the sensor, the sensor should be so aligned that the direction of the force is perpendicular to the resistance element to overcome this vulnerability.

Another approach to increase the robustness of the sensor against the above-discussed vulnerability is to increase the number of resistance elements. The increase in the number of resistance elements increases the sensing capability of the sensor to the forces from all directions. This robustness comes with a price of increased complexity in manufacturing and measurement principle and thus increased cost.

3.3.2 Working principle

Figure 3.4 shows the electrical schematic diagram for sensors with single resistance and two resistance elements. The ends of the elements are connected to pins of the measurement apparatus (e.g. a micro-controller). As defined by the measurement principle, required voltage potentials are applied at these pins by programming the measurement apparatus. Several shunt resistances are included in the measurement circuit and the voltage across these resistances is measured with the required sampling rate (>10 kHz for vehicle crash applications). In the normal driving state, there is no electrical contact between the elements of the sensor and hence, there is no change in the measured voltages. In an event of a vehicle crash, the resistance elements establish contact with other elements, this causes a change in electrical resistance across the ends of the resistance elements and the measured voltages. This change in resistance is measured to detect the crash event and to calculate the parameters which are of interest for validation of the crash. These parameters are described below.

- P_L is the position of the left-most contact point from the center of the vehicle or sensor.

- P_R is the position of the right-most contact point from the center of the vehicle or sensor.

- P_C represents the central position of the contact.

- O is the overlap or the width of the contact at a given point in time.

The central position P_C is the midpoint of the left-most and right-most contact position, while the overlap O is the addition of the absolute value of the two positions. The measurement procedures used for the validation sensor are explained
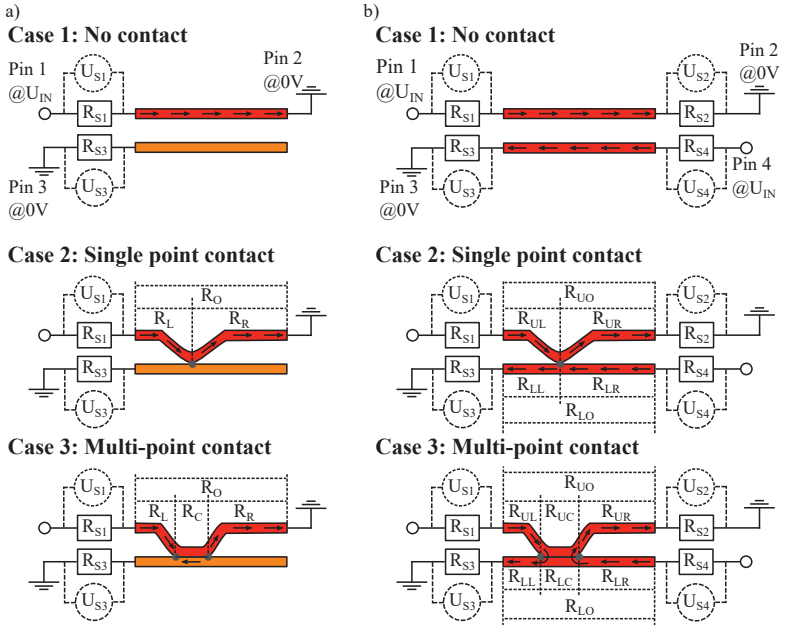
Figure 3.4: Electrical schematic diagrams for validation sensor: a) single-resistance element sensor, and b) two-resistance elements sensor. (Note: Red color represents resistance element, while orange color represents wiper. The voltage potential at pins are shown in case 1 and they are the same for case 2 and case 3, but not displayed in respective figures to avoid repetition).

below which is an extension of the research work described in [2].

Single-resistance element sensor: The electrical schematic of the measurement circuit for the single-resistance element sensor is shown in Figure 3.4a. Input potential U_{IN} is applied to pin 1 of the sensor, while pin 2 is grounded (kept at 0 volts) to make the current flow through the resistance element. This current is measured by connecting a shunt resistance R_{S1} between pin 1 and the end of the resistance element. R_{S1} should be kept considerably low (a few ohms) so that the voltage drop across it is small enough as compared to the resistance element. Another shunt resistance R_{S3} is connected between the one end of the wiper and pin 3. This resistance should be as large as possible (some mega-ohms) and is introduced in the measurement circuit to reduce the noise at the floating wiper. The required position information is derived from the voltages measured across the shunt resistances.

During the usual driving condition, there is no electrical contact between the resistance element and the wiper (see case 1 of Figure 3.4a). Hence, the voltage across R_{S3} is zero. When a crash occurs, the contact between the resistance element and the wiper is established and the voltage across R_{S3} increases depending on the position of the contact point. Initially, a single-point contact is established, and gradually as time progresses, the contact area increases changing to multi-point contact.

Based on the contact type the overall resistance R_O of the sensor can be divided into two or three parts, R_L part of the resistance element on the left side of the contact point, R_R part of the resistance element on the right side of the contact point and R_C part of the resistance element between the two extreme contact points. Since the wiper consists of conductive material and its resistance is comparatively negligible, R_C can be ignored, and using the equation of specific electrical resistance, R_O can be written as

$$R_O = R_L + R_C + R_R = R_L + R_R = \frac{\rho}{A} \cdot (L - O), \qquad (3.15)$$

where L is the length of the sensor, ρ is the specific resistivity of the resistance element and A is the cross-sectional area of the resistance element. According to Ohm's law, R_O is given by

$$R_O = (U_{IN} - U_{S1}) \cdot \frac{1}{U_{S1}/R_{S1}} = \left(\frac{U_{IN}}{U_{S1}} - 1\right) \cdot R_{S1}. \qquad (3.16)$$

From equations 3.15 and 3.16, the overlap is given by

$$O = L - R_O \cdot \frac{A}{\rho} = L - \left(\frac{U_{IN}}{U_{S1}} - 1\right) \cdot R_{S1} \cdot \frac{A}{\rho}. \qquad (3.17)$$

The left contact point position P_L is calculated by

$$
\begin{aligned}
P_L &= \frac{L}{2} - R_L \cdot \frac{A}{\rho} \\
&= \frac{L}{2} - \frac{U_{IN} - U_{S1} - U_{S3}}{U_{S1}/R_{S1}} \cdot \frac{A}{\rho} \\
&= \frac{L}{2} - \frac{U_{IN} - U_{S1} - U_{S3}}{U_{S1}} \cdot R_{S1} \cdot \frac{A}{\rho} \\
&= \frac{L}{2} - \left(\frac{U_{IN} - U_{S3}}{U_{S1}} - 1\right) \cdot R_{S1} \cdot \frac{A}{\rho},
\end{aligned}
\qquad (3.18)
$$

while the right contact point position is given by

$$P_R = O - P_L. \qquad (3.19)$$

Substituting equations 3.17 and 3.18 in equation 3.19

$$
\begin{aligned}
P_R &= L - \left(\frac{U_{IN}}{U_{S1}} - 1\right) \cdot R_{S1} \cdot \frac{A}{\rho} - \frac{L}{2} + \left(\frac{U_{IN} - U_{S3}}{U_{S1}} - 1\right) \cdot R_{S1} \cdot \frac{A}{\rho} \\
&= \frac{L}{2} + \left(\frac{U_{IN} - U_{S3} - U_{IN}}{U_{S1}} - 1 + 1\right) \cdot R_{S1} \cdot \frac{A}{\rho} \\
&= \frac{L}{2} - \frac{U_{S3}}{U_{S1}} \cdot R_{S1} \cdot \frac{A}{\rho}.
\end{aligned}
\tag{3.20}
$$

According to the vehicle axis system defined by International Standard ISO 8855 [134], the positive is considered on the left side. The same axis system is considered in this work. Hence, the central position of the contact is given by

$$
P_C = \frac{P_L - P_R}{2}.
\tag{3.21}
$$

In the above equation, a negative central position would indicate that the contact position is to the right of the vehicle center and vice versa. In the case of single-point contact, there is no overlap, i.e. O is zero and P_R has the same value as P_L but with the opposite sign.

Multiple-resistance element sensor: Figure 3.4b shows the electric representation for the two-resistance elements sensor. Input potential U_{IN} is applied to pins at the opposite end of the two resistance elements (pin1 and pin 4), while the other two pins (pin2 and pin3) are grounded. This criss-cross configuration makes the current flow through both elements. The current flowing at the four ends is measured by inserting shunt resistances R_{S1}, R_{S2}, R_{S3}, and R_{S4} between the ends of the resistance elements and their respective pins. All the shunt resistances for this type of sensor should be kept considerably low (a few ohms) so that the voltage drop across them is small compared to the resistance elements.

The current measured at one end of a particular resistance element is equal to the current measured at the other end of the resistance element in a normal driving condition. When a crash occurs, both the resistance elements come in contact with each other and there are changes in the current flowing through the resistance elements. The electric current would flow from pin 1 to pin 3 and from pin 4 to pin 2 as shown in case 2 and case 3 of Figure 3.4b.

Similar to the single-resistance element sensor, the overall resistances R_{UO} and R_{LO} of the upper and lower resistance elements of this sensor type can be divided into left (R_{UL} and R_{LL}), right (R_{UR} and R_{LR}), and central (R_{UC} and R_{LC}) parts respectively.

Applying Kirchoff's voltage law to the left side voltage loop of the contact

$$
U_{IN} - U_{S1} - R_{UL} \cdot \frac{U_{S1}}{R_{S1}} - R_{LL} \cdot \frac{U_{S3}}{R_{S3}} - U_{S3} = 0.
\tag{3.22}
$$

Rearranging equation 3.18

$$U_{IN} - U_{S1} - U_{S3} = R_{UL} \cdot \frac{U_{S1}}{R_{S1}} + R_{LL} \cdot \frac{U_{S3}}{R_{S3}}. \tag{3.23}$$

Defining a new term α as a ratio of the resistance per unit length of the upper and lower resistance element

$$\alpha = \frac{\rho_U}{A_U} \cdot \frac{A_L}{\rho_L}, \tag{3.24}$$

where ρ_U and ρ_L is the specific resistivity of the upper and lower resistance element respectively. While A_U and A_L are the cross-sectional areas of the two elements. This term depends on the material of the two resistance elements and is considered as constant for a particular sensor. Using the resistivity equation the ratio of R_{UL} to R_{LL} can be written as

$$\frac{R_{UL}}{R_{LL}} = \frac{\rho_U}{A_U} \cdot L_{UL} \cdot \frac{A_L}{\rho_L} \cdot \frac{1}{L_{LL}}. \tag{3.25}$$

The length of the part from the two resistance elements corresponding to the resistance R_{UL} and R_{LL} can be assumed to be equal to each other and hence the equation 3.25 becomes,

$$\frac{R_{UL}}{R_{LL}} = \frac{\rho_U}{A_U} \cdot \frac{A_L}{\rho_L} = \alpha. \tag{3.26}$$

Substituting equation 3.26 in equation 3.23

$$U_{IN} - U_{S1} - U_{S3} = \alpha \cdot R_{LL} \cdot \frac{U_{S1}}{R_{S1}} + R_{LL} \cdot \frac{U_{S3}}{R_{S3}}$$
$$= R_{LL} \left(\alpha \cdot \frac{U_{S1}}{R_{S1}} + \frac{U_{S3}}{R_{S3}} \right). \tag{3.27}$$

Rearranging equation 3.27, R_{LL} is given by

$$R_{LL} = \frac{U_{IN} - U_{S1} - U_{S3}}{\left(\alpha \cdot \dfrac{U_{S1}}{R_{S1}} + \dfrac{U_{S3}}{R_{S3}} \right)}. \tag{3.28}$$

Based on the resistivity equation, P_L is given by

$$P_L = \frac{L}{2} - R_{LL} \cdot \frac{A_L}{\rho_L}. \tag{3.29}$$

Substituting equation 3.28 in 3.29

$$P_L = \frac{L}{2} - \frac{U_{IN} - U_{S1} - U_{S3}}{\left(\alpha \cdot \dfrac{U_{S1}}{R_{S1}} + \dfrac{U_{S3}}{R_{S3}} \right)} \cdot \frac{A_L}{\rho_L}. \tag{3.30}$$

Table 3.2: Different contact configurations for a three-resistance elements sensor (E1, E2, and E3 represent resistance element-1, element-2, and element-3 respectively, while the black line represents the contact).

Left contact ╲ Right contact	E1 & E2	E2 & E3	E1 & E3	E1, E2, & E3
E1 & E2				
E2 & E3				
E1 & E3				
E1, E2, & E3				

Similarly, the equation for P_R can be derived considering the voltage loop on the right side of the contact and is given by

$$P_R = \frac{L}{2} - \frac{U_{IN} - U_{S2} - U_{S4}}{\left(\alpha \cdot \dfrac{U_{S2}}{R_{S2}} + \dfrac{U_{S4}}{R_{S4}} \right)} \cdot \frac{A_L}{\rho_L}. \tag{3.31}$$

In the above equations U_{IN}, R_{S1}, R_{S2}, R_{S3}, and R_{S4} are fixed by the design of the measurement apparatus and thus known. The voltages U_{S1}, U_{S2}, U_{S3}, and U_{S4}, are measured, while the remaining parameters can be calculated from the measurement before the crash during normal driving conditions. P_C can be calculated with equation 3.21 given in the above section, while the addition of P_L and P_R would give us the overlap O.

As discussed in Section 3.3.1, the robustness of the sensor can be increased by using additional resistance elements. Consider a three-resistance elements sensor as shown in Figure 3.3b. At any given instant of time, there are four types of contacts possible at a particular contact point. Three of them are given by the combination of elements for a two-element contact and the fourth type is where all the three elements are in contact with each other. For a vehicle crash application, the position of the two extreme contact points is of importance, which represents the contact width during the crash. Considering, the two extreme contact points (left-most and right-most contact point), sixteen different contact configurations are possible as shown in Table 3.2. The table emphasizes the complexity of measurement due to an additional resistance element.

This complexity can be reduced by using a switching technique as shown in Figure 3.5. At any instant of time, only two resistance elements are active while the third element is inactive (isolated). This reduces the possible contact configurations from sixteen to nine (configurations remaining in Table 3.2 after deleting the last column and last row). With the use of the switching technique, the above-explained measurement principle for the two-resistance elements sensor can be used. The position of the contact points from all the configurations can be measured over a short cycle time. One measuring cycle is divided into three sub-cycles. In each sub-cycle, as mentioned only a pair of resistance elements are active. The pin-voltages at the ends of the element are chosen to retain the criss-cross measuring configuration explained for the two-resistance elements sensor in this section. The voltage configuration for different sub-cycles is shown in Figure 3.5b.

3.3.3 Dynamics of contact point position and its importance

As discussed in the previous section, the proposed sensor can sense the crash condition by contact detection and measure the position of impact based on the change in the electrical resistance from the contact. After the contact, the width of the contact gradually increases with the crash duration causing a change in the position of the contact points (P_L and P_R). This change in position depends on the parameters such as velocity, orientation, and shape of the ego-vehicle and
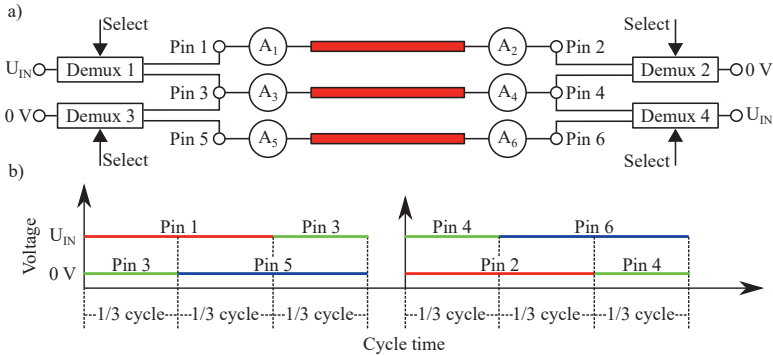

Figure 3.5: Measurement methodology for three-resistance elements type sensor: a) Electrical schematic with switching by using de-multiplexer and b) Voltage configurations for different sub-cycle. (Note: Pin-voltages at the end of the elements are represented by red color for element-1, green color for element-2, and blue color for element-3).

opponent-object, which can be used for validation. The contact points movement is a combined effect of the three parameters mentioned and can be calculated for the initial few milliseconds of crash duration using the parameters predicted by the forward-looking sensors. Hence, a combined validation of these predicted parameters is possible by comparing the measured and the calculated movements of the contact points. A detailed explanation of the methodology for this validation is given in Chapter 4.

3.4 Experimental investigation

The validation sensor was examined through a series of experiments to investigate its performance. The sensor was first examined in a simple finger-contact test to check the behavior of the change in resistance with the contact position. Next, the sensor was studied in a pendulum test to investigate its behavior under low-speed impact conditions. After confirming the performance of the sensor from the above-discussed tests, it was investigated in a crash test with other crash sensors for comparison. Since the crash test comprises of an investigation from several other sensors along with the validation sensor, this test is discussed in this section to give a comprehensive summary. The details and results from the finger contact and pendulum tests are given in [2], [3], [5].

3.4.1 Test details

The aim of the crash test was to verify the functioning of the proposed sensor in the test condition similar to a real vehicle crash and to compare it with other presently used sensors. A compact passenger car (Volkswagen Golf-IV) was chosen as a test vehicle. In the crash test, this vehicle was impacted at 64 km/h against a rigid barrier as shown in Figure 3.6a. The test vehicle was aligned to have an impact of a 40% overlap on the driver's side. The data from the sensors during the crash test was recorded using two data acquisition systems. The first system (M-bus Pro, Messring GmbH) was sampled at 100 kHz, which was used to measure the signals from the acceleration sensors. The other data acquisition system (LTT-24, Labortechnik Tasler GmbH) was used to measure the signals from other sensors at a sampling rate of 1000 kHz. These systems along with the power supply were mounted away from the crash-zone in the vehicle trunk. Three high-speed cameras were installed in the test area to monitor the crash from the top, left, and right perspectives. All the cameras recorded the crash at a frame rate of 1000 frames per second. Both the data acquisition systems and the camera system were triggered by a standard tape switch trigger used in the crash test. This trigger ensures the time synchronization of different systems with all systems having the same zero time (t_0), which corresponds to the first contact of the test vehicle with the rigid barrier.
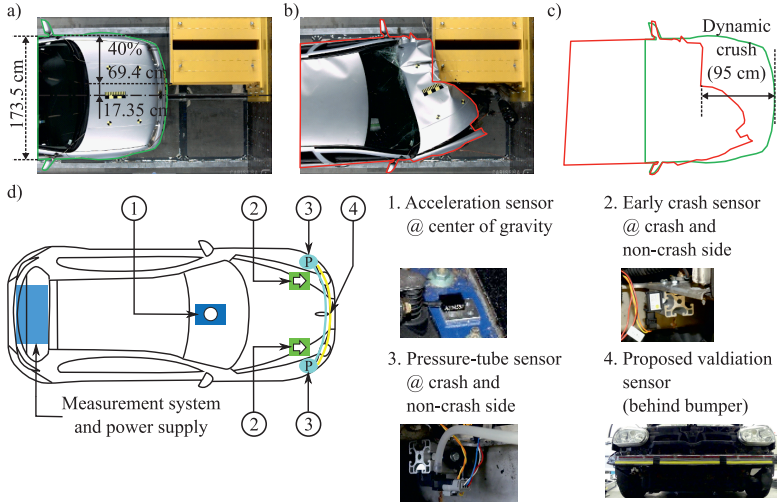
Figure 3.6: Crash test details and sensor configuration: a) Frame at first contact, b) frame at maximum deformation, c) vehicle boundary schematic showing maximum deformation, and d) sensor configuration. (Note: Both the pressure-tube (transparent color) and the validation sensor (yellow color) are installed in the foam material behind the bumper beam).

3.4.2 Sensor configuration

The sensor configuration chosen for the crash test is shown in Figure 3.6d. It consists of three additional sensors along with the validation sensor for comparison. The acceleration pulse at the center of gravity is the most basic and common measurement in vehicle safety. The parameters derived from this pulse are used in present vehicles as a measure for the deployment of passive safety systems. Therefore, it was decided to mount a standard crash test acceleration sensor (Type – M0053A, Kistler Instrumente GmbH) to record this acceleration pulse from the crash test. The acceleration sensors used for the crash test have higher resolution compared to the cost-optimized passive safety sensors used in the vehicle. As discussed in Section 2.1, some vehicles employ a pair of ECS sensors (one on the driver's side and one on the passenger's side) in addition to the sensor at the center of gravity. Since these two types of sensors represent the signals from the sensors used in the present vehicles, they form the baseline for comparison. The third sensor chosen was a pressure-tube sensor, which is in use for low-impact-energy applications such as a vehicle crash against pedestrians. This sensor is in research for its extending its use for high impact-energy such as vehicle-to-vehicle

crashes and hence it is selected for comparison against the proposed sensor. The pressure-tube sensor was installed in the foam material between the bumper beam and the bumper (see Figure 3.6d). The validation sensor used in the crash test was a two-resistance elements type with a length of 140 cm. It was also installed in the foam material next to the pressure-tube sensor so that both the sensors have a similar deformation during the crash test.
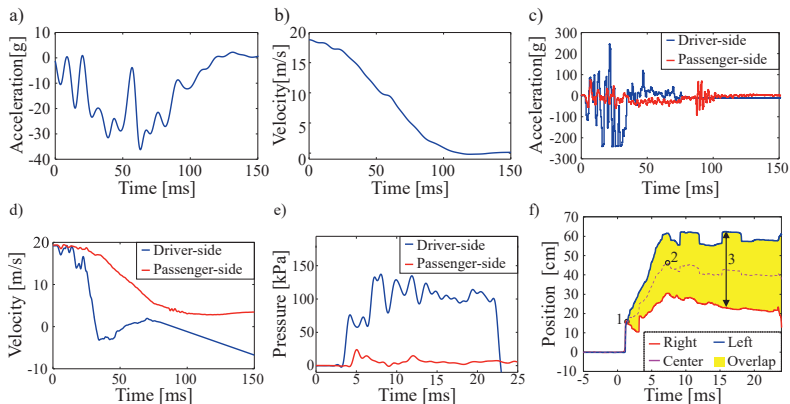
Figure 3.7: Crash test results: a) acceleration signal from the sensor at the center of gravity, b) derived velocity signal from the sensor at the center of gravity, c) acceleration signal from ECS, d) derived velocity signal from ECS, e) pressure-tube sensor, and f) proposed validation sensor.

3.4.3 Results and discussion

The damage caused to the vehicle by impacting against the rigid barrier can be visualized in Figures 3.6b and c. A major part of the energy was absorbed by the deformation of the front crash structures, with some damage extended to the A-pillar on the driver-side. The maximum deformation during the crash in the longitudinal direction was about 95 cm. The results from the different sensors under investigation are discussed in the below paragraphs.

Acceleration sensor at the center of gravity: Figure 3.7a shows the filtered acceleration signal recorded by the sensor at the center of gravity. Applying a low-pass filter is a common pre-processing procedure in crash data analysis. A technical bulletin from Euro-NCAP [135] gives the guidelines on using the low-pass filter for different sensors. A low-pass Butterworth filter with zero-phasing was applied in forward and reverse directions with a cut-off frequency of 100 kHz to the acceleration signals as a pre-processing step. The acceleration signals show

a crash duration of 118 ms, which is given by the time at the zero acceleration after the initial fluctuations. It can be observed that for a considerable amount of time (about 60 ms) the vehicle experiences high decelerations (above 20 g) and has a maximum deceleration of 36.2 g. These values indicate a severe crash with the necessity for the deployment of restraint systems. Most of the complex passive safety algorithms consider velocity signals for activating restraint systems such as airbags [136]. The velocity signals have comparatively fewer fluctuations, especially in the initial deformation phase of the crash during which the decision on deployment of restraint systems is taken. The fewer fluctuations help in a better and faster judgment of the crash severity. Hence, the filtered acceleration signals were integrated to derive the velocity signals and were used for comparison with other sensors.

Early crash sensors: ECS sensors used in the test were the same as the sensors used in vehicles for passive safety applications. These sensors had a lower resolution compared to the instrumentation grade sensor used at the center of gravity and hence have higher fluctuations (see Figure 3.7c). It is not possible to derive any useful information directly from the acceleration signals even after low-pass filtering. Nevertheless, the velocity signals derived from these noisy acceleration signals shown in Figure 3.7d, provide a much better perspective. The signals from the driver-side sensor have a steeper negative slope compared to the passenger-side, which indicates a driver-side impact. The driver-side sensor was broken during the crash test by the deformation from the crash (indicated by the constant value in the acceleration signal). For this reason, only a part of the signal from this sensor up to 80 ms can be considered, while the passenger-side sensor survived the crash and its complete signal can be considered.

Pressure-tube sensor: The impact from the crash induces a pressure wave in the tube, which travels on either side of the impact at close to the speed of sound in the air and is measured by the pressure sensors at both ends. Since the impact is on the driver's side, higher pressure amplitudes are detected on this side compared to the passenger's side (see Figure 3.7e). Also, the pressure wave has a comparatively shorter distance to travel at the driver-side. This causes the passenger-side pressure signal to lag behind the driver-side signal. It is possible to calculate the position of impact using this time lag and is derived below. The position of impact $P_{L,pr}$ from the driver-side (left) sensor is given by

$$P_{L,pr} = t_{L,pr} \cdot c, \tag{3.32}$$

where $t_{L,pr}$ is the time at which the pressure shown by the driver-side sensor exceeds the threshold, and c is the speed of sound in air. Similarly, impact position $P_{R,pr}$ from the passenger-side (right sensor) sensor is given by

$$P_{R,pr} = t_{R,pr} \cdot c, \tag{3.33}$$

where $t_{R,pr}$ is the threshold crossing time for the passenger-side sensor. The impact position with respect to the center of the tube can be calculated using the length of the pressure tube L, which is given by the addition of equations 3.32 and 3.33

$$P_{c,pr} = \frac{L}{2} - P_{L,pr} = \frac{P_{L,pr} + P_{R,pr}}{2} - P_{L,pr} = \frac{t_{R,pr} - t_{R,pr}}{2} \cdot c. \qquad (3.34)$$

The value of the position calculated using the above equation for the pressure-tube sensor is used for comparison against the validation sensor in Section 3.4.4. Additionally, at 22.9 ms a negative pressure signal can be observed for the sensor at the driver-side, which indicates that this sensor is damaged.

Proposed validation sensor: The validation sensor measures the voltages across the shunt resistances at the end of the resistance element. The position values were calculated over the complete crash duration from these voltages using the equations 3.30, 3.31, and 3.21 as shown in Figure 3.7e. At about 1 ms, a steep increase in the position values is observed. This indicates that contact between the two resistance elements has been established. After this time, the position of the left contact point increases steeply as compared to the right contact point and the yellow region between these two signals represents the dynamics of the contact width or overlap during the crash. After 1.4 ms (point 1 in Figure 3.7e), the difference in the left and right contact point position increases which indicates a transfer from single-point contact to multi-point contact. At about 7.8 ms (point 2 in Figure 3.7e), the maximum position for the left contact point is reached, which is also observed in the position values of the left contact point which fluctuates about a maximum value. The voltage across the shunt resistance was zero after 24.2 ms indicating a break in the current flow. This break is caused by sensor damage from the severe deformation process during the crash and will not affect the validation process because this process is performed by the information acquired before the break in the current flow.

3.4.4 Comparison of the investigated sensors

The results of the different sensors investigated in the crash test were compared based on three criteria. A vehicle crash is recognized by the crash sensors based on the change in its signal from the normal driving condition. The response time at which a particular sensor shows a considerable change in its signal was chosen as the first criterion. The threshold for this change was decided based on the maximum recorded value (10% of the maximum value) for each sensor. The importance of information on the position of impact is described in Section 3.1 and hence it was selected as the second criterion. The third criterion considered for comparison was whether the sensor could provide information on the development of the contact points.

As discussed in the above section, the derived velocity signals were considered for both acceleration-based sensors. The threshold for the acceleration sensor at

Table 3.3: Comparison of results from different sensors under investigation

Sensor type	Crash event detection		Position of impact		Ability to measure overlap
	Threshold	Time [ms]	Position value [cm]	Time [ms]	
Central acceleration sensor	2.0 m/s	24.2	-	-	-
Early crash sensor	1.6 m/s	14.6	left	14.6	-
Pressure-tube sensor	2.5 kPa	3.4	18.8	4.5	-
Proposed validation sensor	6.2 cm	1.1	16.1	1.4	Overlap value with time

the center of gravity was set to a deviation of about 2.0 m/s (10% of 20.6 m/s). At 24.2 ms after t_0, this deviation was reached and the sensor can identify the crash event. This sensor cannot alone provide information on the other criterion. For ECS sensors, the threshold limit was selected based on the maximum value of the velocity signal from the passenger-side sensor. The initial fluctuations of the ECS sensors from the impact were ignored. The driver-side sensor was first to record this change in signal (at 14.6 ms), which highlights the time-benefit (about 11.5 ms) gained by using ECS sensors in addition to the central sensor in the present vehicles. At 14.6 ms, the change in the signal of the passenger-side sensor is below the threshold and hence a driver-side (left position) impact can be identified. Therefore, these sensors can classify the position of impact as left, right, or center in addition to the crash event detection. The pressure-tube sensor recorded a maximum pressure of 144 kPa on the driver's side and 23.5 kPa on the passenger's side. The lower value of the two maximum values was considered for threshold calculation (10% of 23.5 = 2.35 kPa). The driver-side sensor crosses this threshold before (at 3.4 ms) than the passenger-side sensor (at 4.5 ms). In contrast to the impact-position classification of ECS sensors, this sensor can provide a value for the position of impact (18.8 cm for the crash test) using equation 3.34 mentioned in the above section. It can be observed that the validation sensor crosses the threshold value (10% of 62.44 = 6.2) at 1.1 ms, shows the impact position of 16.1 cm at 1.4 ms, and further provides information on overlap by measuring the position of the two extreme contact points compared to the other sensors. Table 3.3 summarizes the comparison of the results from the different investigated sensors.

3.5 Potential for improvement

3.5.1 Investigation of required time for airbag activation

Let us consider a simplified mass-spring model to investigate the occupant-vehicle dynamics and their relations to the detection timing required by the sensors. Figure 3.8 shows such a simplified mass-spring model which describes the motion of the occupant under the influence of a respective acceleration response of the vehicle from a crash. The variables in the model are described as follows

- s, c, and ω are the slack, specific stiffness, and natural frequency of the restraint system,

- m_o and m_v are the masses of the occupant and the vehicle respectively,

- x_o, v_o, and a_o is the displacement, velocity, and natural acceleration of the occupant relative to the ground,

- $x_{o/v}$, $v_{o/v}$, and $a_{o/v}$ are the displacement, velocity, and natural acceleration of the occupant relative to the vehicle, and

- x_v, v_v, and a_v is the displacement, velocity, and natural acceleration of the vehicle relative to the ground.

In crash analysis, usually, an idealized crash pulse such as Equivalent Square Wave (ESW) is used to represent the acceleration response of the vehicle from the crash. This is given by the following equation

$$a_v = ESW = \frac{F_{avg}}{m_v \cdot g}. \tag{3.35}$$

The average force 'F_{avg}' is given by the ratio of the kinetic energy before the crash to the maximum displacement '$x_{v(max)}$' of the vehicle from the crash, which modifies the above equation to

$$a_v = ESW = \frac{1}{2}\left(\frac{m_v \cdot v_0^2}{x_{v(max)}}\right)\frac{1}{m_v \cdot g} = \frac{1}{2 \cdot g}\left(\frac{v_0^2}{x_{v(max)}}\right). \tag{3.36}$$

Considering the values of $v_0 = 64\text{km/h} = 17.78\text{m/s}$ and $x_{v(max)} = 0.95\text{m}$ from the crash test explained in Section 3.4.3, the value for ESW come approximately to -17 g. The negative sign is added to indicate the deceleration of the vehicle.

Until the displacement of the occupant reaches the value equal to the slack 's' of the restraint system, the occupant velocity 'v_o' is constant and equal to the initial impact velocity 'v_0' i.e. the velocity of the vehicle v_v at t_0, and this period is called free-flight. During the free-flight phase from $t = t_0 = 0$ till $t = t_s$,

$$s = v_0 \cdot (t_s - 0) = v_0 \cdot t_s. \tag{3.37}$$

49
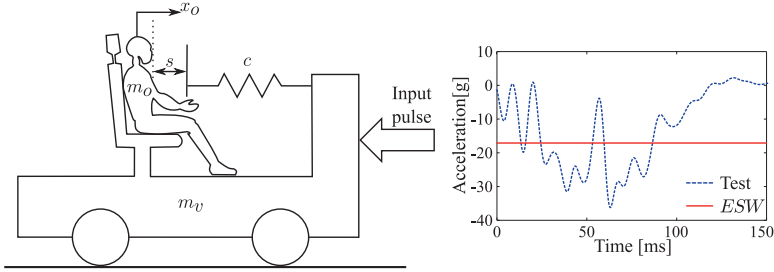
Figure 3.8: Simplified mass-spring model for determining the maximum time for sensing a crash. The dotted blue curve is the crash-pulse or acceleration signal at the center of gravity from the vehicle given in 3.4.3, while the red curve is the *ESW* corresponding to the crash test performed.

After this period, the restraint coupling phase starts where the seatbelt exerts a force on the occupant's chest to decelerate the occupant. The occupant acceleration relative to the vehicle for a mass-spring model can be assumed as a sine-wave response and can be represented by the following equation.

$$a_{o/v} = a_0 + a_v = A \cdot \sin\left(\omega t' + \phi\right), \tag{3.38}$$

where t' is the time which starts from the restraint coupling phase, i.e. $t' = t - t_s$. By integrating the above equation, the occupant velocity relative to the vehicle is given by

$$v_{o/v} = \int (a_0 + a_v) = -\frac{A}{\omega} \cdot \cos\left(\omega t' + \phi\right). \tag{3.39}$$

The constant of integration is neglected since the initial condition is matched using the phase shift. This helps to match the initial value of the velocity according to the initial conditions (see next paragraph). Integrating the above equation, the occupant displacement relative to the vehicle is given by

$$x_{o/v} = \int (v_0 + v_v) = -\frac{A}{\omega^2} \cdot \sin\left(\omega t' + \phi\right) + C. \tag{3.40}$$

The constant of integration in the above equation is considered to match the initial occupant displacement.

Considering initial conditions, at $t' = 0$, the occupant acceleration $a_o = 0$ then the equation 3.38 gives,

$$a_{o/v} = 0 + a_v = ESW \cdot g = A \cdot \sin\left(\phi\right). \tag{3.41}$$

Also, at $t' = 0$, the relative occupant velocity $v_{o/v} = ESW \cdot g \cdot t_s = ESW \cdot g \cdot \dfrac{s}{v_0}$,

which modifies the equation 3.39 to

$$v_{o/v} = ESW \cdot g \cdot \frac{s}{v_0} = -\frac{A}{\omega} \cdot \cos(\phi). \tag{3.42}$$

Summing the squares of the equations 3.41 and 3.42, we get

$$A = \pm\sqrt{(ESW \cdot g)^2 + \left(ESW \cdot g \cdot \omega \frac{s}{v_0}\right)^2}. \tag{3.43}$$

The sign of the amplitude 'A' is chosen to match the direction of occupant responses. Dividing equation 3.41 by equation 3.42,

$$\tan \phi = -\frac{v_0}{s \cdot \omega}. \tag{3.44}$$

Moreover, at $t' = 0$, the relative occupant displacement $v_{o/v} = s$ and substituting it in equation 3.40 gives

$$C = s + \frac{A}{\omega^2} \cdot \sin(\phi). \tag{3.45}$$

A simple approach to estimate the maximum time available for the sensor to decide on airbag activation can be computed based on the general thumb rule of '5 inch – 30 milliseconds' [104]. This rule says that the airbag should be activated the latest 30 milliseconds before the time corresponding to the 5 inches of travel (displacement) of the occupant. The time of 30 milliseconds is selected based on the approximate time required by a driver airbag to fully inflate, while the distance of 5 inches is the general distance between the fully inflated airbag surface and the driver. Based on the above-derived equation for occupant motion, we can calculate the maximum time available for the sensors for the crash test performed in Section 3.4.3 using the following equation

$$t = t_s + t' = t_s + \frac{\sin^{-1}\left(\left(C - x_{o/v}\right) \cdot \frac{\omega^2}{A}\right) - \phi}{\omega} \tag{3.46}$$

with $x_{(o/v)} = 0.127$ m corresponding to the 5 inches. Taking the various crash cases covered in [104] into consideration, the natural frequency of the restraint system can vary from 4 to 8 Hz, while the slack varies from about 0.5 to 8 inches including unbelted occupant cases. Thus, considering a restraint system with a natural frequency of 6 Hz and slack of 0.025 m (belted occupant) and inserting these values in equation 3.46 gives 38.2 milliseconds for an occupant to reach the airbag surface or travel 5 inches distance. Hence, the maximum available time for the sensor is about 8.2 milliseconds in the case of crashes with a severity similar to the crash test performed. This requirement can be fulfilled only by the pressure-tube sensor or the proposed validation sensor (see Table 3.3). The physical limit of the acceleration-based sensors is the reason for their late response.

The front of the vehicle (about 20 cm) is usually made from soft materials such as plastic, foam, and easily deforming aluminium material (see Section 5.2.1 for detailed explanation on vehicle structure) which provide very little resistance to vehicle motion. Hence, there is negligible change in the acceleration and velocity signals (see Figure 3.7) till the time corresponding to this displacement is reached, i.e. for the above case $t_{(x=0.2)} = \dfrac{\text{distance}}{\text{velocity}} \cdot 1000 = \dfrac{0.2}{17.78} \cdot 1000 = 11.25$ ms.

Moreover, today's airbags are limited in the protection capability (volume capacity) from the time taken by the sensors for detecting the crash. Larger airbags providing a more cushioning effect with extended protection area would reduce the distance between the occupant and the fully inflated airbag surface due to an increase in size and also require more time to fully inflate the airbag. Hence, an improvement in detection timing creates an opportunity to use larger volume airbags to further enhance occupant safety. The above investigation highlights the need and importance of sensors such as the proposed validation sensor which can detect the crash earlier. To summarize this chapter, the improvement provided by the proposed validation sensor over the other sensors is outlined in the subsection below.

3.5.2 Summary

The acceleration-based sensors give a direct measure of the crash-severity based on different parameters such as jerk, velocity, displacement, energy, etc. derived from the acceleration signal [104]. For a better crash classification, several acceleration-based sensors distributed at different special locations such as ECS can be used. Even with the distributed system, the acceleration-based sensors have limitations in response time to detect a crash and further analyze its severity. This restricts the present vehicle safety systems from using advanced restraints systems such as smarter and bigger airbags which require more time.

Contact-based sensors can be mounted on the structural members which are very close to the outer-skin of the vehicle. Hence, these sensors have a location advantage which is reflected in their signals as time-benefit for crash detection (seen in signals of pressure-tube sensor and proposed validation sensor). Out of these two sensors, the pressure-tube sensor is slower. This delay comes from the time required for the pressure wave to travel to the ends of the tube. Moreover, in the cases where the position of impact is away from the center, it has to wait for the sensor on the non-impact side to cross the threshold, after which the position value can be calculated. The proposed validation sensor measures the change in electrical resistance depending on the contact, which can be directly measured after the contact without any delay. Every millisecond gained in crash detection can be used in improving vehicle safety by the use of advanced restraint systems. The results from the crash test conducted show the time-benefit which can be gained using the validation sensor and thus the improvement in vehicle safety.

It also tracks the movement of the two extreme contact points during the crash and hence the overlap progress with time can also be measured. This information can be further used for a combined validation of pre-crash information such as velocity, approach angle, and shape. A detailed discussion of the procedure for this combined validation is given in Chapter 4. For the pressure-tube sensor, based on the time lag only the initial position of impact can be calculated with no information on how the contact develops later.

One of the major concerns for the pressure-tube sensor is the deterioration of the material causing holes in the tube during its life. These holes cause a variation in the pressure signal and also the time lag which deteriorates the sensing function of this sensor. Since a small amount of current flows through the validation sensor continuously, there is a possibility for a self-health monitoring feature in the proposed validation sensor. The deterioration of the material would reflect in the current signal during its life and a message to visit the nearest workshop could be displayed on the dashboard if the tube material deteriorates enough to affect the functioning of the sensor.

The above-discussed points and the experimental investigation highlight the potential for improvement in vehicle safety by using the proposed validation sensor. Moreover, the unique feature of self-health monitoring would increase the robustness of crash detection. The idea of the validation sensor which is the outcome of this work is in the phase of investigation for series production with a goal of cost-optimization.

Chapter 4

Opponent-object Geometry: Simplification and Estimation

Abstract

A novel methodology for estimating the geometry of the opponent vehicle based on the cloud point data and geometry-based prediction of dynamic change in the position of contact points during a crash are the highlights of this chapter. The chapter is introduced with a description of the basic geometries of the opponent objects, followed by a detailed explanation of the proposed methodology for geometry estimation along with the different concepts and equations used in this methodology. The performance of this methodology is demonstrated in the experimental investigations and results section of this chapter. The next section of this chapter is dedicated to the above-mentioned geometry-based predictions. A detailed theory and derivation of the equations for the position of the contact points during the crash for collision against different types of opponents form the basis of this prediction. These equations are then used to investigate the different crash scenarios. In the end, the prediction values are compared with the positions of contact points measured using the contact-based sensor for the crash test described in Chapter 3.

A contact-based sensor for validation of pre-crash information introduced in Chapter 3 can be used for a combined validation of parameters such as velocity, approach angle, and geometries of both ego-vehicle and opponent-object. These parameters for ego-vehicle are easily available from the on-board sensors and devices installed in it. The main challenge is to acquire the parameters of the opponent-object. Vehicle-to-everything (V2X) communication and prediction algorithms based on forward-looking sensors are two possible approaches in research for acquiring this information. Besides security and technological challenges faced by the V2X communication approach, it requires that every object (especially vehicles) on roads can communicate. Moreover, for vehicle safety applications the information is time-critical (e.g., in about 50 to 200 ms, a considerable change in velocity and position of the vehicle is possible which may affect the required safety decisions). Therefore in vehicle safety applications, the latter approach is preferred.

Out of the above-mentioned parameters, estimating the geometry and the angular orientation of the opponent-object using the data from the forward-looking sensors is a challenging task. The relative velocity is either directly measured through the Doppler effect of radar sensors [46] or can be derived from the distance measured between the two data frames of the lidar or camera sensor.

Since the geometry estimation of the vehicles involves all the complexities as compared to other traffic participants, most of the studies for opponent-geometry estimation concentrate on them. In addition to vehicles, there are other opponent-objects against which an ego-vehicle can collide. The following section gives a general overview of the geometry of different objects surrounding an ego-vehicle.
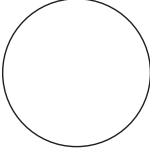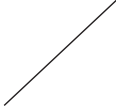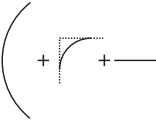
4.1 Geometry of objects in vehicle's surrounding

In road transport, an ego-vehicle is surrounded by different stationary objects (trees, walls, poles from traffic signals and signs, guard rails, etc.) as well as moving objects (other vehicles, animals, pedestrians, e-scooters, motorbikes, bicycles, etc.). These objects have various shapes and sizes which are their fundamental characteristics. For example, the diameter of the pole for a traffic signal is regulated and is within a specific dimension range. Hence, predicting the shape and size of these objects can help in estimating their class or type. Moreover, the shape of the object is also significant for making safety-critical decisions on the inevitability of an upcoming crash. A three-dimensional shape increases the complexity by increasing the parameters required for defining the shape and is not necessary for the above task. Moreover, to perform this task in real-time, a simplification is essential. The shapes of the objects can be simplified and approximated by basic two-dimensional geometry such as lines and/or arcs of the circle. Most of the objects surrounding the vehicle can be represented in three categories shown in Table 4.1 and explained below.

- Circular geometry can be used to represent objects like a tree, pole, etc. For these objects orientation of the ego-vehicle is not important because of the symmetry of the circular shape, but the offset distance with the longitudinal axis of the vehicle is important in defining the crash scenario.

- Objects such as a wall or a guard rail can be represented by a simple line. The angle of this line depends on the orientation of the ego-vehicle with the object.

- Two-dimensional geometry of some objects is complex and cannot be represented by a single geometrical shape (line or circular arc) and need a combination of these geometrical shapes. For these objects both the offset and the orientation with the ego-vehicle are important.

Vehicles are one of the major participants in road transport having a complex shape, especially the front of the vehicle which requires a more accurate representation than a single geometrical shape (line or circular arc). The following section

Table 4.1: Simplified two-dimensional geometrical representation of some objects in vehicle surroundings.

Category	Object	Geometrical representation
Circle-based objects		
Line-based objects		
Hybrid objects		

proposes a methodology in which the vehicle geometry is represented by a combination of simplified geometrical elements. The choice of the geometrical elements is limited to arcs of circles and lines due to the simplicity of their equations and thereby reducing the complexity of the pre-crash algorithms. For example, the estimation of initial contact points based on the intersection of geometry is simpler for circle-based geometries than other complex curve-based geometries such as an ellipse, higher degree polynomials, etc. Also, for the task of geometry-based predictions of contact point positions during the initial few milliseconds of the crash, the solutions are confined to roots of quadratic equations (see Section 4.3) without the requirement of complex iterative methods, which helps to simplify the contact-based validation of a particular crash scenario. A similar combination method can be used to represent the geometry of all the objects with complex shapes.

4.2 Proposed methodology for vehicle geometry estimation

The basic idea of the proposed methodology emerged from the need for a simplified mathematical representation of the vehicle geometry for contact-based validation. The vehicle geometry is a complex shape, especially the front of the vehicle requires a more accurate representation than a single geometrical shape (line or circular

arc). The major problem in representing the vehicle front is the change in the curvature near the headlights. Therefore, this region of the vehicle is represented by fillet-arcs with larger curvature on both sides. Thus the front of the vehicle is represented by three arcs, a central arc representing the major portion of the geometry combined with two fillet arcs for the curvature in the headlight region (see the output block in Figure 4.1). The side of the vehicle can be represented by a line tangent to the arc representing the headlight region.

4.2.1 Methodology

The point cloud data recorded from the perception or forward-looking sensors serves as an input for estimating the vehicle geometry. Although the lidar sensor 'VLP16' made by Velodyne lidar Inc. was used to generate the necessary point cloud data for the investigation, the methodology itself can be applied to the point cloud data from any other sensors. A general process flow of the proposed methodology for vehicle geometry estimation is illustrated in Figure 4.1. Each block of the process flow is described in the following paragraphs with the help of a single point cloud data frame.

Pre-processing: The point cloud data generated from the sensor requires some pre-processing steps to filter the non-essential data points, before the task of estimating the opponent-vehicle geometry. The first pre-processing step is to eliminate the irrelevant data points by trimming the field of view (FOV) perceived by the sensor to the region of interest. As discussed previously, this work focuses on head-on collision and hence the reflection points from the opponents on the path in front of the ego-vehicle are of interest. The parameters considered for trimming the FOV in the investigations in this work are listed below.

- A maximum limit of 25 meters in front of the vehicle representing the length of the region of interest was considered. This distance was decided based on the reduction of the reflection points as the distance of the object increases from the sensor. At about 25 m away from the sensor about 7 to 10 points from the front contour of the opponent were reflected and measured depending on the sensor configuration parameters.

- Width of the region of interest is specified by the side limits from the center of the vehicle. The EU Council Directive 96/53/EC [137] specifies a maximum permissible width of 2.55 meters (rounded to 2.5 meters) for vehicles on European roadways. Considering two vehicles on one side and rounding the permissible width, a value of ± 5 meters from the vehicle center was considered for the side limits.

- The height of the region of interest was fixed to ± 2 meters from the height of the sensor so that it includes the height of the front curvature of all different commercial vehicles.
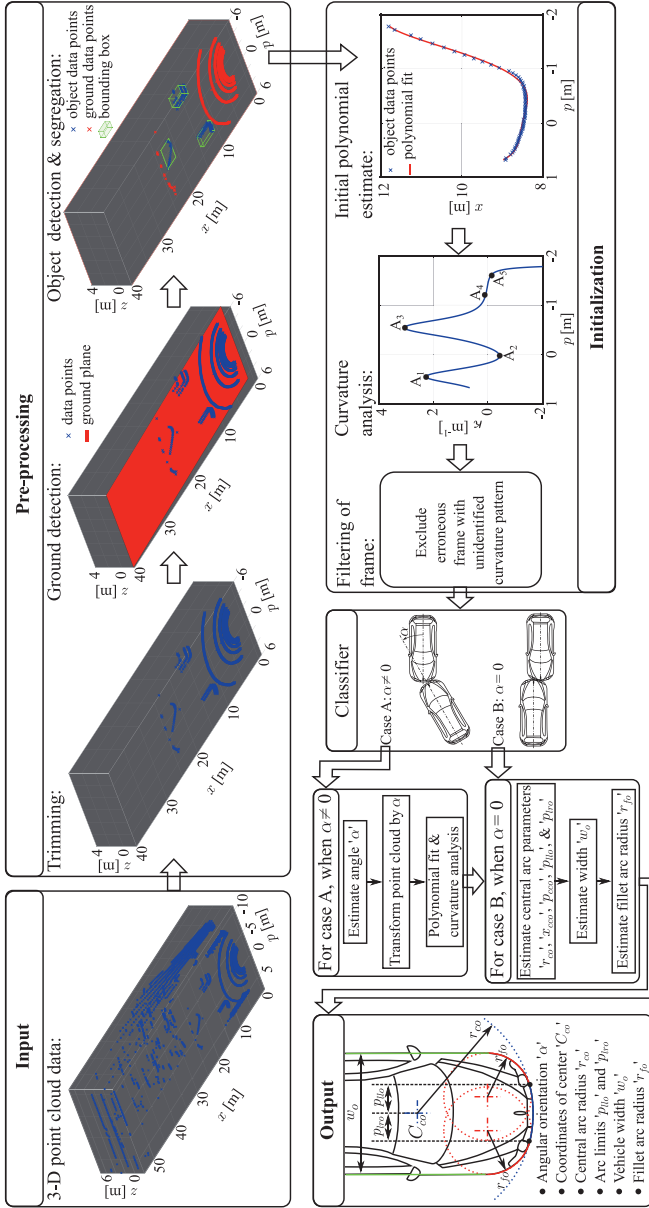
Figure 4.1: Process flow chart of the proposed methodology for vehicle geometry estimation. (For the detailed definition of the output parameters and the sign convention of the angle α refer to Section 4.3. Please note that for the task of geometry estimation the origin of the coordinate system is at the sensor position, which is different from the one used in Section 4.3.)

In the trimming process, the data points falling only in the region of interest are considered, while the data points outside the region of interest are neglected. The first 3-D plot of the pre-processing block in Figure 4.1 shows the data frame after the trimming process.

The data frame after trimming is submitted to a ground plane analysis. In this step, a plane model represented by the point-normal equation form (equation 4.1) is fitted onto the three-dimensional point cloud data (see the red color plane in the second 3-D plot of the pre-processing block).

$$A \cdot x + B \cdot p + C \cdot z + D = 0, \tag{4.1}$$

where the coefficients A, B, and C are direction ratios of the normal to the ground plane and D is a real number. x, p, and z are the coordinate axes. The fitted ground plane gives clear segregation between the data points reflected from the ground and the ones reflected from the opponent-objects. The function 'pcfitplane' [138] (a built-in function of Matlab software) based on the M-estimator SAmple Consensus (MSAC) algorithm was used to find the ground plane equation. Once the ground plane is identified, the data points reflected from the ground (shown by red color cross markings, see last 3-D plot of the pre-processing block in Figure 4.1) are ignored and only the data points reflected from different opponent-objects (shown by blue color cross markings) are considered for further analysis.

These data points reflected from different opponent-objects are clustered into different groups and each group represents a different opponent. A built-in function of Matlab software 'pcsegdist' [139], which segments a point cloud data frame into different clusters based on Euclidean distance was used. The points having a euclidean distance less than the threshold value of 1.5 meters are grouped into one object. The third 3-D plot of the pre-processing block in Figure 4.1 shows three segregated objects in the data frame with their respective bounding boxes. Some driving scenarios, where the opponent-objects are very close to each other result in the euclidean distances between the reflecting points from two objects being less than the threshold limit. In these scenarios, the above clustering approach might face difficulty in identifying the two objects and other advanced clustering approaches might be required. Since the focus of the investigations was only to test the proposed three-arc methodology for vehicle geometry estimation, the clustering approach based on the euclidean distance that gave satisfactory results was used.

Initialization: After the pre-processing step, the segregated clusters of the data points representing a particular object are sent to the initialization block, where an initial guess on the vehicle geometry is made using polynomial fitting and curvature analysis.

The first process of the initialization block is to estimate a polynomial equation representing the front bumper region of the vehicle. At first, the point cloud data of a particular vehicle is further filtered based on the ground height. The height of the individual data points h_i from the ground plane can be calculated using the

below equation.

$$h_i = \frac{|A \cdot x_i + B \cdot p_i + C \cdot z_i + D|}{\sqrt{A^2 + B^2 + C^2}}, \tag{4.2}$$

where the subscript i corresponds to the index of the data point under consideration and varies from 1 to n(no of the data points under consideration in the point cloud). x_i, p_i, and z_i represent the coordinates of the ith point. The points within the range of the bumper height are considered for further analysis. For the investigations, this range was set to 40 to 50 centimeters based on the dimensions of the Audi E-tron. This filtering process reduces the data points from a three-dimensional representation to a two-dimensional one. An initial estimate of the geometry given by equation 4.3 is established by carrying out a polynomial regression using the least square estimation approach between the limits p_{min} and p_{max}. These limits are chosen based on the maximum and minimum values of the data points corresponding to the p-axis.

$$x = a_0 \cdot p^5 + a_1 \cdot p^4 + a_2 \cdot p^3 + a_3 \cdot p^2 + a_4 \cdot p + a_5, \tag{4.3}$$

where a_0, a_1, a_2, a_3, a_4, and a_5 are the coefficients of the polynomial equation. In the next step, the estimated polynomial equation is submitted to a curvature analysis. The curvature values (κ) of the polynomial curve within the limits (p_{min} and p_{max}) are calculated using equation 4.4.

$$\kappa = \frac{\dfrac{\mathrm{d}^2 x}{\mathrm{d}p^2}}{\left(1 + \left(\dfrac{\mathrm{d}x}{\mathrm{d}p}\right)^2\right)^{\frac{3}{2}}}. \tag{4.4}$$

These values are plotted against the corresponding p-coordinates to give a curvature plot from which the necessary anchor points are derived. An anchor point is defined by the two conditions listed below.

- A point on the plot where the direction of the curvature changes i.e. the curvature value changes from decreasing to increasing (point A_2, see curvature analysis plot in Figure 4.1) or vice versa. These points imply an abrupt change in the curvature and hence transition from the fillet-arc region to the central-arc region or vice versa.

- A vehicle side can be identified by a zero curvature value either before the anchor point A_1 or after anchor point A_3. Two points (point A_4 and point A_5 are chosen as the anchor points to identify the line representing the side of the vehicle, see curvature analysis plot in Figure 4.1). The anchor point A_4 corresponds to the curvature value of +0.001 m^{-1}, while the anchor point A_5 corresponds to the curvature value of -0.001 m^{-1}.

With the help of the anchor points, the polynomial curve can be divided into regions of the central arc, fillet arc, and side of the vehicle. Hence, the estimation is made on the bending behavior of the polynomial curve instead of the curve itself.

An unfamiliar curvature pattern in the curvature plot indicates an erroneous frame and these frames are filtered out and not considered for the computation. The unfamiliar pattern can be easily recognized by the number of anchor points based on the curvature change and the number of anchor points representing the side. A data frame having more than five anchor points does not match with the three-arc template, hence such a frame should be skipped and the next frame should be considered.

Classifier: Based on the anchor points derived from the curvature plot, the data frame is categorized by the classifier into either a case where the orientation angle $\alpha \neq 0$ or the one with $\alpha = 0$. Figure 4.2 highlights the difference in the curvature behavior of both cases. The classification is made based on the visibility of the side of the vehicle. When the opponent-vehicle is inline i.e. $\alpha = 0$, the sides of the vehicle are not visible, and hence the corresponding anchor points are not available. For the case where the opponent-vehicle is inclined i.e. $\alpha \neq 0$, one of the sides is visible and the respective anchor points can be identified. The cases with $\alpha \neq 0$ require additional computation steps before geometry estimation and are explained in the following paragraphs.

Case A ($\alpha \neq 0$): For the cases where the opponent-vehicle is inclined, the first task is to calculate the angle α. This angle is calculated based on the coordinates of the anchor points A_4 and A_5 of the curvature plot (see Figure 4.2b). The x-coordinates of these anchor points are calculated by inserting their p-coordinates in equation 4.3. The coordinates of the anchor points A_4 and A_5 are used to calculate the orientation angle using the following equation.

$$\alpha = \tan^{-1}\left(\frac{p_{A5} - p_{A4}}{x_{A5} - x_{A4}}\right), \tag{4.5}$$

where x_{A4}, x_{A5}, p_{A4}, and p_{A5} are the x and p- coordinates of the anchor points A_4 and A_5 respectively. Once the angle is computed, the perpendicular distance of all the data points from the line passing through the points on the polynomial fit corresponding to the anchor points A_4 and A_5 are calculated. The data points having a perpendicular distance less than the threshold value (5 centimeters) are considered as associated with the side of the vehicle. The data points from the side of the vehicle are ignored and a new matrix consisting of the coordinates of the remaining data points which are reflected from the front region of the vehicle is formed. The coordinates of the data points associated with the front region of the vehicle are then rotated by angle α using equation 4.6.

$$[p' \; x'] = [p \; x] \begin{bmatrix} \cos\alpha & \sin\alpha \\ -\sin\alpha & \cos\alpha \end{bmatrix}. \tag{4.6}$$
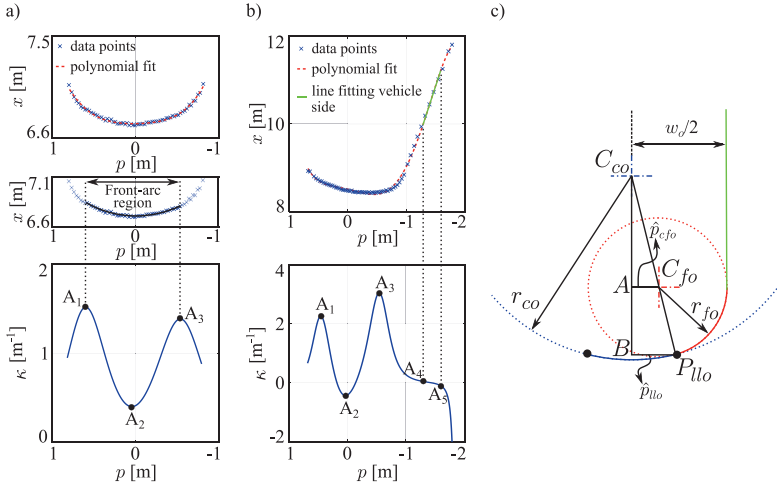
Figure 4.2: Figures for a detailed explanation of the proposed methodology for vehicle geometry estimation: a) polynomial fit on data points (top plot), figure showing front-arc region (middle plot), and curvature plot (bottom plot) - for case B ($\alpha = 0$), b) polynomial fit on data points (top plot) and curvature plot (bottom plot) - for case A ($\alpha \neq 0$), and c) Geometrical schematic for calculation of fillet-arc radius.

This rotation process transforms the set of data points from the front of the vehicle from an inclined case to a case where $\alpha = 0$. This transformed set of data points is submitted to polynomial regression and then curvature analysis processes as explained in the above paragraphs. The further steps for the geometry estimation are similar to the case with $\alpha = 0$ and hence explained in the next paragraph. As the magnitude of α increases (an increase from zero in either direction i.e. positive and negative), the lesser region from the front of the vehicle is visible to the sensor and could result in the disappearance of either of the anchor points A_1 or A_3 depending on the direction of the angle. A virtual anchor point at the end of the curvature plot near the missing anchor point is assumed to continue with the central-arc estimation.

Case B ($\alpha = 0$): Based on the anchor points A_1 and A_3, the point cloud data is divided into three parts as shown in Figure 4.2a. The central part of the data points corresponds to the central-arc region. A circle is fitted on the set of data points belonging to the central arc using the least square regression approach to find the radius r_{co} and the coordinates x_{cco} and p_{cco} of its center C_{co} (see the middle graph in Figure 4.2a). It should be noted that if this step is performed on the rotated data points corresponding to case A, the coordinates of the data

points are in the transformed coordinate axes $(x'\text{-}p\prime)$ and should be transformed back to the $(x\text{-}p)$ coordinate system.

Once the p-coordinate of the central-arc center is known, the width of the opponent-vehicle w_o can be calculated using equation 4.7.

$$w_o = \max\left[2 \cdot (p_{fmax} - p_{cco}), 2 \cdot (p_{cco} - p_{fmin})\right], \tag{4.7}$$

where p_{fmax} and p_{fmin} are the maximum and minimum values of the p-coordinate from the set of the data points belonging to the front of the opponent-vehicle under consideration.

After calculating the width, the p-coordinates of the anchor points A_1 and A_3 are used to calculate the left limit $\hat{p}_{llo}$ of the central arc based on the following equation.

$$\hat{p}_{llo} = \max\left[|p_{A1} - p_{cco}|, |p_{cco} - p_{A3}|\right]. \tag{4.8}$$

Considering the front contour of the vehicle as symmetrical, the other limit $\hat{p}_{lro}$ has the same magnitude as that of the left limit but has a negative sign. Please note ' ^ ' symbol is used to indicate that these limits are calculated from the center of the central arc to match with the representation of the limits for the opponent-vehicle used in Section 4.3.3. The last parameter radius r_{fo} which is the radius of the fillet-arc can be calculated based on the defined geometry as shown in Figure 4.2c. By applying a similar triangle rule to $\triangle C_{co}C_{fo}A$ and $\triangle C_{co}P_{llo}B$, we get the following equation for the $\hat{p}$-coordinate of the fillet-arc center.

$$\hat{p}_{cfo} = \frac{r_{co} - r_{fo}}{r_{co}} \cdot \hat{p}_{llo}. \tag{4.9}$$

The width of the vehicle can be represented by the following equation.

$$w_o = 2\left(r_{fo} + \hat{p}_{cfo}\right). \tag{4.10}$$

Inserting equation 4.9 in 4.10 the above equation becomes

$$\begin{aligned} w_o &= 2\left(r_{fo} + \frac{r_{co} - r_{fo}}{r_{co}} \cdot \hat{p}_{llo}\right) \\ &= 2\left(r_{fo}\left(1 - \frac{\hat{p}_{llo}}{r_{co}}\right) + \hat{p}_{llo}\right) \\ &= r_{fo} \cdot \frac{2}{r_{co}}\left(r_{co} - \hat{p}_{llo}\right) + 2 \cdot \hat{p}_{llo}. \end{aligned} \tag{4.11}$$

Rearranging the above equation, the equation for r_{fo} is given by

$$r_{fo} = \frac{w_o - 2 \cdot \hat{p}_{llo}}{r_{co} - \hat{p}_{llo}} \cdot \frac{r_{co}}{2}. \tag{4.12}$$

Using the above methodology, all the parameters for defining the three-arc representation of the opponent-vehicle can be calculated from a single frame of the

point cloud data. The geometrical parameters predicted from the multiple frames of the point cloud data contain variations originating from the noise in the lidar data points. From the output parameters, r_{fo} is a derived parameter and α is a variable parameter (since the vehicle moves and can change its orientation from one data frame to another). Moreover, α is estimated from the polynomial fit on the data points, which itself reduces the noise variations. Hence the variation in width and central-arc parameters, which should not change from one frame to another are considered for prediction improvement. The following paragraph gives a brief discussion on the sources of variation and an approach to improve the predictions.

The first source of variation is introduced by the change in the horizontal resolution of the lidar data points caused by the change in the distance between the reflected surface and the sensor as the ego-vehicle approaches the opponent-object. This effect can be explained by the two states shown in Figure 4.3a. When the distance between the object and the sensor is x_1, the outermost data points are at the corner with a total of four data points reflected from the object's surface. As the sensor moves closer to the object, the outermost data points move towards the central axis of the sensor. When the distance between the object and the sensor reaches x_2, two additional data points are reflected from the object's surface. Since the prediction of w_o depends on the outermost data points, this effect has a direct impact on its prediction. For the data frames between the distance x_1 and x_2, the predicted width would gradually decrease till the new data points are introduced at distance x_2 and this saw-tooth behavior continues as shown in Figure 4.3b.
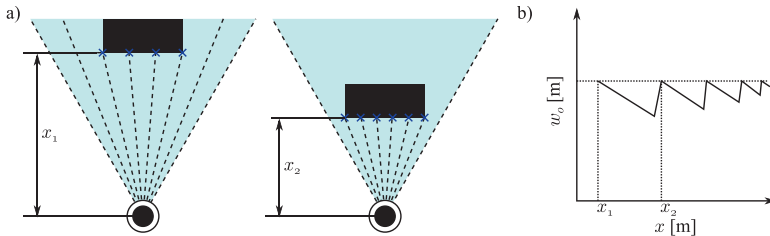
Figure 4.3: Variation in lidar data points introduced by a change in the distance: a) schematic representing lidar data point reflected from an object at distances x_1 and x_2 and b) saw-tooth effect on the width prediction.

Noise in the reflected data points forms another source of variation. A direct eradication of the noise is not possible since it depends on multiple external and internal parameters. Nevertheless, statistical approaches can be used to reduce the impact of noise and improve the prediction. The effect of this variation is visualized in the central-arc parameters. One approach to improve the prediction is to use a simple one-dimensional Kalman filter. This filter continuously receives the predicted values and estimates the final values. An example of such a filter to

estimate the central-arc radius is given by the following equation.

$$r_{co,e(t)} = r_{co,e(t-1)} + KG \cdot (r_{co,p(t)} - r_{co,e(t-1)}), \tag{4.13}$$

where $r_{co,e(t)}$ and $r_{co,e(t-1)}$ are the current and previous estimated value of the central-arc radius respectively, $r_{co,p(t)}$ is the current predicted value of the central-arc radius and KG is the Kalman filter gain, which is given by the following equation.

$$KG = \frac{E_{e(t-1)}}{E_{e(t-1)} + E_{sensor}}, \tag{4.14}$$

where E_{sensor} is the possible variance in the central-arc radius from the variations of the lidar points measured by the sensor and $E_e(t-1)$ is the estimation error, which is updated for each data frame after estimation using the below equation.

$$E_{e(t)} = (1 - KG) \cdot E_{e(t-1)}. \tag{4.15}$$

The value of E_{sensor} is assumed as 0.1 meters, while the initial values of central-arc radius and estimation error are defined as 1.5 and 0.3 meters respectively.

4.2.2 Experimental investigation and results

The investigation of the methodology for vehicle geometrical estimation was carried out in three testing phases. The aim of the first phase was to compare the geometrical predictions given by the above methodology with the ground truth (physical dimensions of the opponent-object). The second testing phase was intended to examine the working of the methodology under the multiple vehicles scenario, while the third phase was selected to check the methodology under the real driving scenario by mounting the lidar sensor on the vehicle and testing the methodology in real-time. For all the tests, VLP-16 lidar sensor from Velodyne Inc. was used as it can provide the required point cloud data at a reasonable cost. The following paragraph explains the test setup used for different tests.

Test setup: The first and the second testing phase was conducted in the indoor crash-test facility of CARISSMA research and test center affiliated to Technische Hochschule Ingolstadt, Germany. The test setup for the first and second types of tests can be explained with the schematic and pictures in Figures 4.4a, c, and d. The lidar sensor was installed on the crash test trolley representing the ego-vehicle about 30 centimeters from the ground. The trolley was pulled to follow a straight trajectory to approach the stationary objects whose geometries are to be predicted using the crash test facility.

Using a vehicle as an opponent-object directly for the first testing phase would result in variation of the ground truth due to the complexity of the shape of the vehicle, making it not feasible for measuring the performance of the proposed methodology. Therefore, a wooden target with simplified geometry (uniform along with the height) was fabricated which can be used as a standard for comparison.
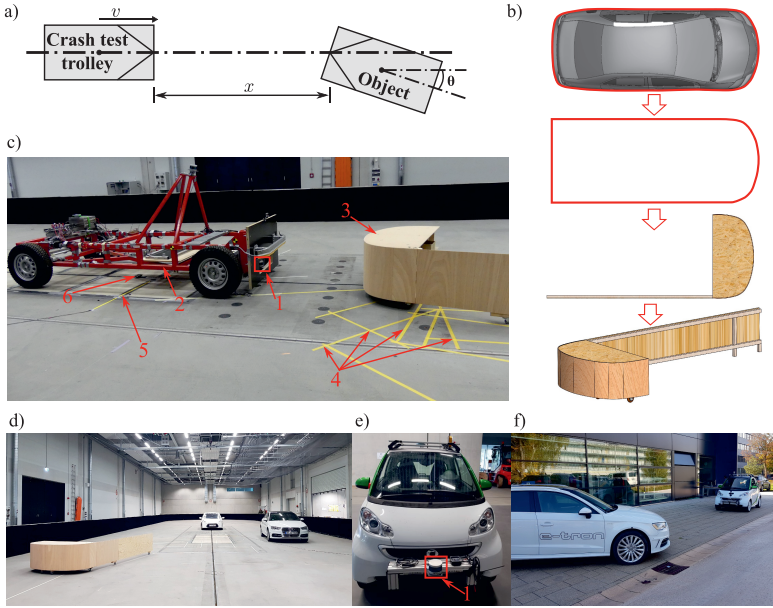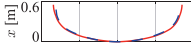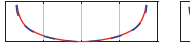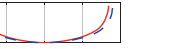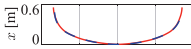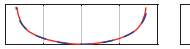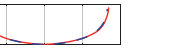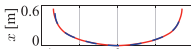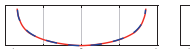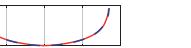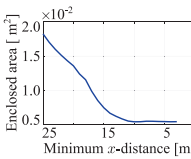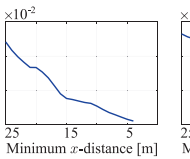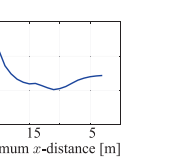
Figure 4.4: Compositions of schematic and pictures describing different test setups: a) a simplified schematic of the experimental setup for the first testing phase, b) simplified wooden target fabrication process, c) an image of the first testing phase, d) an image of the multi-object testing phase, e) an image of lidar sensor mounting for real-time testing, and f) picture showing the real-time testing. In the figure, 1) lidar sensor, 2) crash test trolley, 3) simplified wooden target, 4) angle markings for object orientation, 5) trigger strip for braking, and 6) connection to wire rope of propulsion system.

The outer edge from the top view of the publicly available engineering drawings was used as a template for manufacturing the wooden target and the fabrication procedure can be visualized in Figure 4.4b. A series of tests were conducted with different orientation angles (0, 15, and 45 degrees) of the wooden target to investigate how it affects the geometry prediction. The trolley was pulled at 10 km/h and the VLP-16 was set to collect data at 20 Hz. In the second testing phase, two additional objects were placed in the testing area to analyze the working of the methodology under the multiple objects scenario (see Figure 4.4d). For the third testing phase as shown in Figure 4.4e, the lidar sensor was mounted on a vehicle (Smart from Daimler AG) and was driven straight toward a stationary vehicle (Audi E-Tron).

Table 4.2: Results from the tests against the simplified wooden target. Note: In the first three rows, the 2-D geometry from the predicted parameters at three different frames (Frame at 25, 15, and 5 meters from the lidar sensor) is reconstructed with angular and translation transformations to match with ground-truth data for pictorial representation.

Parameter	0 degree	-15 degree	-45 degree
Frame at x-dist. 25 m			
Frame at x-dist. 15 m			
Frame at x-dist. 5 m			
Prediction accuracy: Enclosed area			

Results: To demonstrate the effectiveness of the proposed methodology for geometry estimation, the results from the first testing phase, i.e. the tests against the simplified wooden target at different orientation angles are considered for discussion in this section. The results from these tests can be directly compared with the ground-truth (simplified wooden target) is the reason for discussing this testing phase. The parameter values predicted from the tests are tabulated in Appendix C. A pictorial representation of the results for three different frames is displayed in the first three rows in Table 4.2. These rows show the predicted front contour (2-D geometry) using the proposed methodology in dashed blue lines against the actual contour (ground-truth derived from the cad model) in solid red lines at three different frames. It can be observed that as the lidar sensor moves near the target, the predicted geometry approximates the ground-truth. This is due to the consideration of multiple frames for prediction as explained above in the methodology section. Even though the first three rows portray visually the closeness of the prediction to the ground-truth but they do not quantify this closeness. The enclosed area between the two curves is a good measure of the closeness of the two curves which is plotted against the minimum distance of the target from the lidar sensor to illustrate the effectiveness of the prediction.

67

These plots are presented in the fourth row of Table 4.2. The improvement in the prediction using multiple frames can be visualized by the reduction in the enclosed area with the distance. The results from the investigations carried out to test this methodology are published in [7], [9], [14], [15], [19]. A detailed comparison of the proposed methodology with other methods based on different metrics is represented in [8], [18].

With the proposed methodology, the geometry of the vehicle can be represented by parameters that fully define the three-arc template. This template can be used in trajectory planning applications instead of the present bounding-box or convex-hull approach for better inevitability decisions. Another application where this methodology can be utilized is contact-based validation. An approach to use the three-arc vehicle geometry template for predicting the dynamic change in the contact width is explained in Section 4.3.3.

4.3 Geometry-based prediction of the dynamic behavior of contact points

In this section, a method for predicting the movement of the contact points during the crash (analogous to the position of the contact points measured using the contact sensor in Section 3.4) is explained. The equations for the intersection points of the ego-vehicle and opponent-object geometry form the basis of this prediction method. During the initial few milliseconds of the crash, only the soft vehicle parts (such as the plastic bumper, foam, etc.), which offer very little resistance to vehicle motion undergo deformation. Hence, the velocity of the ego-vehicle and the opponent-object can be assumed to be constant for the calculation of the contact point positions. Also, the motion of the ego-vehicle and opponent-object (if any) can be assumed to be linear without any rotation.

For deriving the equations, the ego-vehicle is considered as the reference and can be assumed as stationary by transferring the movement of the ego-vehicle to the opponent-object. This means that the opponent-object moves by a magnitude equal to the movement of the ego-vehicle but in the opposite direction in addition to its motion (if any). The coordinate system used is based on the vehicle coordinate system specified in ISO-8555 with the longitudinal axis of the ego-vehicle represented by x, while the lateral axis represented by p denoting the position calculated using this methodology (predicted position). In this section, the methodology is explained considering frontal collisions as an example but it is not limited to and can be easily expanded to side crash scenarios. Furthermore, an ego-vehicle can collide with different opponent-objects as categorized in Section 4.1 forming the three basic cases which are explained in the following subsections.

4.3.1 Case 1: Collision of an ego-vehicle with a circle-based object

The crash scenario where an ego-vehicle collides against a stationary circle-based object such as a tree or pole is shown in Figure 4.5a. In this case, the opponent is represented by a circle, usually with a diameter smaller than the width of the ego-vehicle as is the case with most of the objects in this category. Moreover, the collision can be considered as in-line with the longitudinal axis of the ego-vehicle (horizontal axis of both the objects parallel to each other in Figure 4.5a). Here,

- r_{ce} is the radius of the central arc and r_{fe} is the radius of the arcs representing the headlight region of the ego-vehicle.

- d_e is the variable representing the displacement of the ego-vehicle, which can be derived from the velocity of the vehicle.

- p_{off} is the offset between the axes of the ego-vehicle and opponent-object.

- P_0 is the point of contact at t_0 or the initial contact point with p_0 and x_0 as coordinates.

- P_{lle} is the left or driver-side limiting point of the central arc for ego-vehicle with p_{lle} and x_{lle} as coordinates.

- P_{lre} is the right or passenger-side limiting point of the central arc for ego-vehicle with p_{lre} and x_{lre} as coordinates.

- w_e is the width of the ego-vehicle.

- r_o is the radius of the opponent-object.

As discussed in Section 4.1, the front of the ego-vehicle is divided into three regions. Considering frontal collisions for the ego-vehicle, P_0 can lie in any of these three regions. When P_0 lies in the central-arc region (see Figure 4.5c), p_{off} can be represented by

$$p_{off} = p_0 + p_0 \frac{r_o}{r_{ce}}, \qquad (4.16)$$

which gives the equation for p_0 as

$$p_0 = p_{off} \frac{r_{ce}}{r_{ce} + r_o}. \qquad (4.17)$$

Let us consider an example where P_0 lies in the central-arc region of the ego-vehicle as shown in Figure 4.5c (i.e. $p_{lle} \geq p_0 \geq p_{lre}$). The center of the central arc of the ego-vehicle C_{ce} is chosen as the origin and the equation for this arc is given by

$$x^2 + p^2 = r_{ce}^2. \qquad (4.18)$$
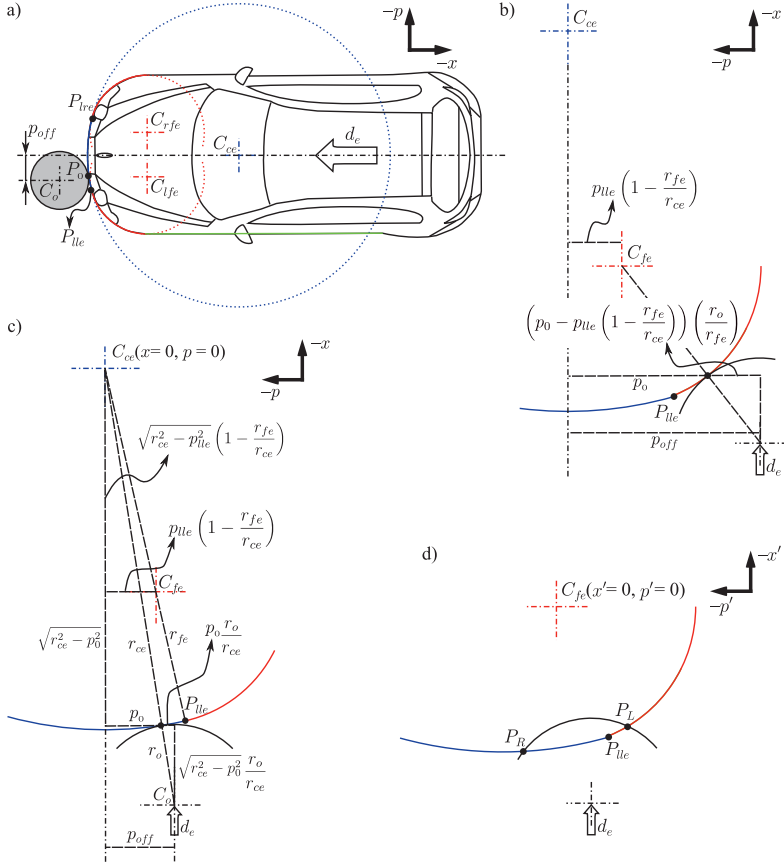
Figure 4.5: Geometrical representation of an ego-vehicle colliding against a tree or pole: a) geometrical schematic, b) illustration of P_0 in the fillet-arc region on the driver's side, c) illustration of P_0 in the central-arc region, and d) illustration of contact transfer in the fillet-arc region.

The equation of the circle for the opponent geometry can be written as

$$\left(x - \left(\sqrt{r_{ce}^2 - p_0^2}\left(1 + \frac{r_o}{r_{ce}}\right) - d_e\right)\right)^2 + \left(p - \left(p_0\left(1 + \frac{r_o}{r_{ce}}\right)\right)\right)^2 = r_o^2. \qquad (4.19)$$

Inserting

$$\sqrt{r_{ce}^2 - p_0^2}\left(1 + \frac{r_o}{r_{ce}}\right) - d_e = e \qquad (4.20)$$

$$\text{and } p_0 \left(1 + \frac{r_o}{r_{ce}}\right) = f \qquad (4.21)$$

in equation 4.19 we get

$$x^2 - 2ex + e^2 + p^2 - 2fp + f^2 = r_o^2. \qquad (4.22)$$

Rearranging equation 4.18

$$x^2 = r_{ce}^2 - p^2, \qquad (4.23)$$

which gives

$$x = \pm\sqrt{r_{ce}^2 - p^2}. \qquad (4.24)$$

Substituting equation 4.23 and equation 4.24 in equation 4.22 we get

$$\pm\sqrt{r_{ce}^2 - p^2} = \frac{e^2 + f^2 + r_{ce}^2 - r_o^2}{2e} - \left(\frac{f}{e}\right)p. \qquad (4.25)$$

Inserting

$$\frac{e^2 + f^2 + r_{ce}^2 - r_o^2}{2e} = g \qquad (4.26)$$

in equation 4.25

$$\pm\sqrt{r_{ce}^2 - p^2} = g - \left(\frac{f}{e}\right)p. \qquad (4.27)$$

Squaring both sides the above equation becomes

$$r_{ce}^2 - p^2 = g^2 - \frac{2gf}{e}p + \left(\frac{f}{e}\right)^2 p^2. \qquad (4.28)$$

Rearranging the above equation in the general quadratic form $ax^2 + bx + c = 0$,

$$\left(\left(\frac{f}{e}\right)^2 + 1\right)p^2 - \frac{2gf}{e}p + \left(g^2 - r_{ce}^2\right) = 0. \qquad (4.29)$$

Where,

$$a = \left(\frac{f}{e}\right)^2 + 1, \qquad (4.30)$$

$$b = -\frac{2gf}{e}, \qquad (4.31)$$

$$\text{and } c = g^2 - r_{ce}^2. \qquad (4.32)$$

The contact develops from a single point of contact at t_0 into two-point contact as time increases and the positions of the left and right contact points are given by the roots of the quadratic equation 4.28. The greater value of the two roots represents the position of the left contact point p_L, while the other root represents

the position of the right contact point p_R. If the roots exceed the limits (p_{lle} and p_{lre}) of the central arc, the contact progresses in the fillet-arc region of the ego-vehicle as shown in Figure 4.5d. To derive the equations for the position of the contact point in the fillet-arc region, a new cartesian coordinate system x'-p' is defined with the center of the fillet arc as the origin. The equation for the fillet arc is given by

$$(x')^2 + (p')^2 = r_{fe}^2. \tag{4.33}$$

Any point can be shifted from this new coordinate system to the x-p coordinate using

$$x = x' + \left(\sqrt{r_{ce}^2 - p_{lle}^2} \left(1 - \frac{r_{fe}}{r_{ce}} \right) \right) \tag{4.34}$$

$$\text{and } p = p' + \left(p_{lle} \left(1 - \frac{r_{fe}}{r_{ce}} \right) \right). \tag{4.35}$$

The above equations represent shifting to the coordinate system with the center of the driver-side fillet arc as the origin. When the contact develops in the passenger-side fillet-arc region, the coordinate system with the origin as the center of the passenger-side fillet arc should be considered. The equations for shifting from this coordinate system to the x-p coordinate system can be formulated by replacing p_{lle} with p_{lre} in equations 4.34 and 4.35.

Substituting equations 4.34 and 4.35 in equation 4.19 and rearranging,

$$\left(x' - \left(\sqrt{r_{ce}^2 - p_0^2} \left(1 + \frac{r_o}{r_{ce}} \right) - \sqrt{r_{ce}^2 - p_{lle}^2} \left(1 - \frac{r_{fe}}{r_{ce}} \right) - d_e \right) \right)^2 +$$
$$\left(p' - \left(p_0 \left(1 + \frac{r_o}{r_{ce}} \right) - p_{lle} \left(1 - \frac{r_{fe}}{r_{ce}} \right) \right) \right)^2 = r_o^2, \tag{4.36}$$

gives the equation of the circle for the opponent geometry in the new coordinate system. Inserting

$$\sqrt{r_{ce}^2 - p_0^2} \left(1 + \frac{r_o}{r_{ce}} \right) - \sqrt{r_{ce}^2 - p_{lle}^2} \left(1 - \frac{r_{fe}}{r_{ce}} \right) - d_e = h \tag{4.37}$$

$$\text{and } p_0 \left(1 + \frac{r_o}{r_{ce}} \right) - p_{lle} \left(1 - \frac{r_{fe}}{r_{ce}} \right) = i \tag{4.38}$$

in equation 4.36 we get

$$(x')^2 - 2hx' + h^2 + (p')^2 - 2ip' + i^2 = r_o^2. \tag{4.39}$$

Rearranging equation 4.33

$$(x')^2 = r_{fe}^2 - (p')^2, \tag{4.40}$$

which gives

$$x' = \pm \sqrt{r_{fe}^2 - (p')^2}. \tag{4.41}$$

Substituting equation 4.40 and equation 4.41 in equation 4.39 we get

$$\pm\sqrt{r_{fe}^2 - (p')^2} = \frac{h^2 + i^2 + r_{fe}^2 - r_o^2}{2h} - \left(\frac{i}{h}\right)p'. \tag{4.42}$$

Inserting

$$\frac{h^2 + i^2 + r_{fe}^2 - r_o^2}{2h} = j \tag{4.43}$$

in equation 4.42

$$\pm\sqrt{r_{fe}^2 - (p')^2} = j - \left(\frac{i}{h}\right)p'. \tag{4.44}$$

Squaring both sides, the above equation becomes

$$r_{fe}^2 - (p')^2 = j^2 - \frac{2ji}{h}p' + \left(\frac{i}{h}\right)^2 (p')^2. \tag{4.45}$$

Rearranging the above equation in the general quadratic form $ax^2 + bx + c = 0$,

$$\left(\left(\frac{i}{h}\right)^2 + 1\right)(p')^2 - \frac{2ji}{h}p' + \left(j^2 - r_{fe}^2\right) = 0. \tag{4.46}$$

The roots of equation 4.46 will give the position of the intersection points in the x'-p' coordinate system. These positions are shifted to the x-p coordinate system using equation 4.35. The intersection points which fall in the fillet-arc region (i.e. $p_{lle} < p < w_e/2$ or $-w_e/2 < p < p_{lre}$) are chosen as the contact point. The above equations are derived for the driver-side impact and the same method can be used for passenger-side impact.

If P_0 lies in the fillet-arc region on the driver's side (see Figure 4.5c), p_{off} is given by

$$\begin{aligned}
p_{off} &= p_0 + \left(p_0 - p_{lle}\left(1 - \frac{r_{fe}}{r_{ce}}\right)\right)\left(\frac{r_o}{r_{fe}}\right) \\
&= p_0\left(1 + \frac{r_o}{r_{fe}}\right) - p_{lle}\left(1 - \frac{r_{fe}}{r_{ce}}\right)\left(\frac{r_o}{r_{fe}}\right) \\
&= p_0\frac{r_{fe} + r_o}{r_{fe}} - p_{lle}\left(1 - \frac{r_{fe}}{r_{ce}}\right)\left(\frac{r_o}{r_{fe}}\right).
\end{aligned} \tag{4.47}$$

From equation 4.47, the position of the initial point of contact is given by

$$p_0 = p_{off}\frac{r_{fe}}{r_{fe} + r_o} + p_{lle}\left(1 - \frac{r_{fe}}{r_{ce}}\right)\left(\frac{r_o}{r_{fe} + r_o}\right). \tag{4.48}$$

In the above equation, if p_{lle} is replaced by p_{lre}, the resulting equation gives the value of p_0 for the case when the initial point of contact lies in the fillet-arc region on the passenger's side. For the crash scenarios, where P_0 lies in the fillet-arc region (i.e. $p_0 > p_{lle}$ or $p_0 < p_{lre}$), the equation for the position of the contact points p

can be derived using a similar method. In these scenarios, the fillet-arc region with x'-p' coordinate system is considered first followed by the central-arc region with x-p coordinate system region when the position value exceeds the limits of the fillet-arc region and falls into the central-arc region. An illustration of a similar procedure is given as an example in the following subsection for reference.

4.3.2 Case 2: Collision of an ego-vehicle with a line-based object

Figure 4.6a shows a geometrical schematic of an ego-vehicle colliding against line-based objects such as a wall. This case is more complex than the above, with the possibility for the wall to be at an angle to the approaching ego-vehicle. Additionally, there is also the possibility of only a part of the vehicle's width can collide with the wall (analogous to the 40% rigid barrier test). In addition to the parameters of the ego-vehicle defined in the above sub-section, the representation of the line geometry of the wall requires the definition of the following parameters.

- β represents the angle between the lateral axis (axis representing p) of the ego-vehicle and the surface of the wall. This angle is measured from the line parallel to the p-axis (initial arm) up to the line representing the wall (terminal arm) in the anticlockwise direction as shown in Figure 4.6a. The line geometry of the wall limits this angle from 0°to 180°. If β is an obtuse angle, the sign of this angle is changed to negative so that the trigonometric functions of this angle which corresponds to a negative value on p-axis match with the sign convention used in x-p coordinate system.

- P_{llo} is the left or driver-side limiting point for the opponent-object with p_{llo} as position coordinate.

- P_{lro} is the right or passenger-side limiting point for the opponent-object with p_{lro} as position coordinate.

Similar to the above case the first step is to identify the region of the ego-vehicle geometry in which the initial point of contact lies by solving for the value of p_0. The equation for p_0 depends on the value of β and has two possibilities. When β is an acute angle, the equation for p_0 is given by

$$
p_0 = \begin{cases} r_{ce} \cdot \sin\beta, & \begin{cases} \text{if } r_{ce} \cdot \sin\beta \leq p_{llo} \leq p_{lle}; \\ \text{if } p_{llo} > p_{lle} > r_{ce} \cdot \sin\beta; \end{cases} \\ p_{llo}, & \begin{cases} \text{if } p_{llo} \leq p_{lle} \ \& \ p_{llo} \leq r_{ce} \cdot \sin\beta; \\ \text{if } p_{llo} > p_{lle} < r_{ce} \cdot \sin\beta \\ \& \ r_{fe} \cdot \sin\beta > p_{llo}; \end{cases} \\ p_{lle}\left(1 - \dfrac{r_{fe}}{r_{ce}}\right) + r_{fe} \cdot \sin\beta, & \begin{aligned} &\text{if } p_{llo} > p_{lle} < r_{ce} \cdot \sin\beta \\ &\& \ r_{fe} \cdot \sin\beta \leq p_{llo}. \end{aligned} \end{cases} \tag{4.49}
$$

When β is an obtuse angle, this value is given by

$$p_0 = \begin{cases} r_{ce} \cdot \sin{(-\beta)}, & \begin{cases} \text{if } r_{ce} \cdot \sin{(-\beta)} \geq p_{lro} \geq p_{lre}; \\ \text{if } p_{lro} < p_{lre} < r_{ce} \cdot \sin{(-\beta)}; \end{cases} \\ p_{lro}, & \begin{cases} \text{if } p_{lro} \geq p_{lre} \\ \& \ p_{lro} \geq r_{ce} \cdot \sin{(-\beta)}; \\ \text{if } p_{lro} < p_{lre} > r_{ce} \cdot \sin{(-\beta)} \\ \& \ r_{fe} \cdot \sin{(-\beta)} < p_{lro}; \end{cases} \\ p_{lre}\left(1 - \dfrac{r_{fe}}{r_{ce}}\right) + r_{fe} \cdot \sin{(-\beta)}, & \text{if } p_{lro} < p_{lre} > r_{ce} \cdot \sin{(-\beta)} \\ & \& \ r_{fe} \cdot \sin{(-\beta)} \geq p_{lro}. \end{cases} \tag{4.50}$$

For this case, let us consider that the initial point of contact lies in the fillet-arc region on the driver side of the ego-vehicle (see Figure 4.6c). As discussed in Section 4.3.1, for deriving the equation of the contact points in the fillet-arc region, the x'-p' coordinate system is considered. Since the ego-vehicle has the same geometry, the fillet-arc region can be represented by equation 4.33 given in the above subsection. The equation for the line representing the wall in the slope-intercept form is given by

$$\begin{aligned} x' &= -\tan{\beta} \cdot p' + r_{fe} \cdot \cos{\beta} + r_{fe} \cdot \sin{\beta} \cdot \tan{\beta} - d_e \\ &= -\tan{\beta} \cdot p' + r_{fe}\left(\cos{\beta} + \frac{\sin^2{\beta}}{\cos{\beta}}\right) - d_e \\ &= -\tan{\beta} \cdot p' + r_{fe}\left(\frac{\cos^2{\beta} + \sin^2{\beta}}{\cos{\beta}}\right) - d_e \\ &= -\tan{\beta} \cdot p' + \frac{r_{fe}}{\cos{\beta}} - d_e \\ &= ep' + f. \end{aligned} \tag{4.51}$$

Where,

$$e = -\tan{\beta} \text{ represents the slope} \tag{4.52}$$

$$\text{and } f = \frac{r_{fe}}{\cos{\beta}} - d_e \text{ is the intercept.} \tag{4.53}$$

Squaring equation 4.51 and substituting in equation 4.33 we get

$$e^2(p')^2 + 2efp' + f^2 + (p')^2 = r_{fe}^2. \tag{4.54}$$

Rearranging the above equation in the quadratic form, it becomes

$$(p')^2\left(e^2 + 1\right) + 2efp' + f^2 - r_{fe}^2 = 0. \tag{4.55}$$

Figure 4.6: Geometrical representation of an ego-vehicle colliding against a line-based object: a) geometrical schematic, b) illustration of P_0 in the central-arc region, c) illustration of P_0 in the fillet-arc region on the driver's side, and d) illustration of contact transfer in the central-arc region.

The roots of equation 4.55 are shifted to the x-p coordinate system using equation 4.35 and then compared with the positions of limiting points to find the position of the contact points. The position of the left contact point is given by the greater of the two roots if this root is less than p_{llo}, else the position is equal to the left limiting position p_{llo}. Similarly, the position of the right contact point is

given by the smaller of the two roots if this root is greater than p_{lro}, else it is equal to the right limiting position p_{lro}. When the roots of the quadratic equation in the x-p coordinate system fall in the central-arc limits (p_{lle} and p_{lre}), this region is considered for calculating the position of the corresponding contact points. Consider the state, where the right contact point progresses in the central-arc region as shown in Figure 4.6d. Substituting equations 4.34 and 4.35 in equation 4.51, we get the equation of the line representing the wall in x-p coordinate as

$$x = e\left(p - \left(p_{lle}\left(1 - \frac{r_{fe}}{r_{ce}}\right)\right)\right) + f + \left(\sqrt{r_{ce}^2 - p_{lle}^2}\left(1 - \frac{r_{fe}}{r_{ce}}\right)\right). \tag{4.56}$$

Inserting

$$g = f + \left(\sqrt{r_{ce}^2 - p_{lle}^2}\left(1 - \frac{r_{fe}}{r_{ce}}\right)\right) - e\left(p_{lle}\left(1 - \frac{r_{fe}}{r_{ce}}\right)\right) \tag{4.57}$$

in equation 4.56 we get

$$x = ep + g. \tag{4.58}$$

Squaring equation 4.58 and substituting in equation 4.18

$$e^2 p^2 + 2egp + g^2 + p^2 = r_{ce}^2. \tag{4.59}$$

Rearranging the above equation in the quadratic form, it becomes

$$p^2\left(e^2 + 1\right) + 2egp + g^2 - r_{ce}^2 = 0. \tag{4.60}$$

The roots of the above equation falling in the central-arc limit are then compared to the opponent limiting positions (p_{llo} and p_{lro}). The position of the required contact points is inferred using the same comparison logic as explained in the above paragraph for contact in the fillet-arc region. In the case of a passenger-side impact, precaution should be taken to incorporate the negative sign arising from the obtuse angle β. In addition to the crash scenarios, where P_0 lies in the central-arc region (i.e. $p_{lre} \leq p_0 \leq p_{lle}$), the equations are derived in the x-p coordinate system followed by the derivation of the equation in the x'-p' coordinate system when the contact points shift to the fillet-arc region.

4.3.3 Case 3: Collision of an ego-vehicle with another vehicle

When the opponent-object is another vehicle, its geometrical representation as explained in Section 4.1 consists of more than one geometrical element. Moreover, the opponent-object can also move apart from the ego-vehicle, and the oblique crash scenarios would require consideration of the lateral and longitudinal movement of the opponent-vehicle. Figure 4.7 shows the representation of a general vehicle-to-vehicle head-on collision. Similar to the above cases, the ego-vehicle is assumed to be stationary and its motion is transferred to the opponent-vehicle for
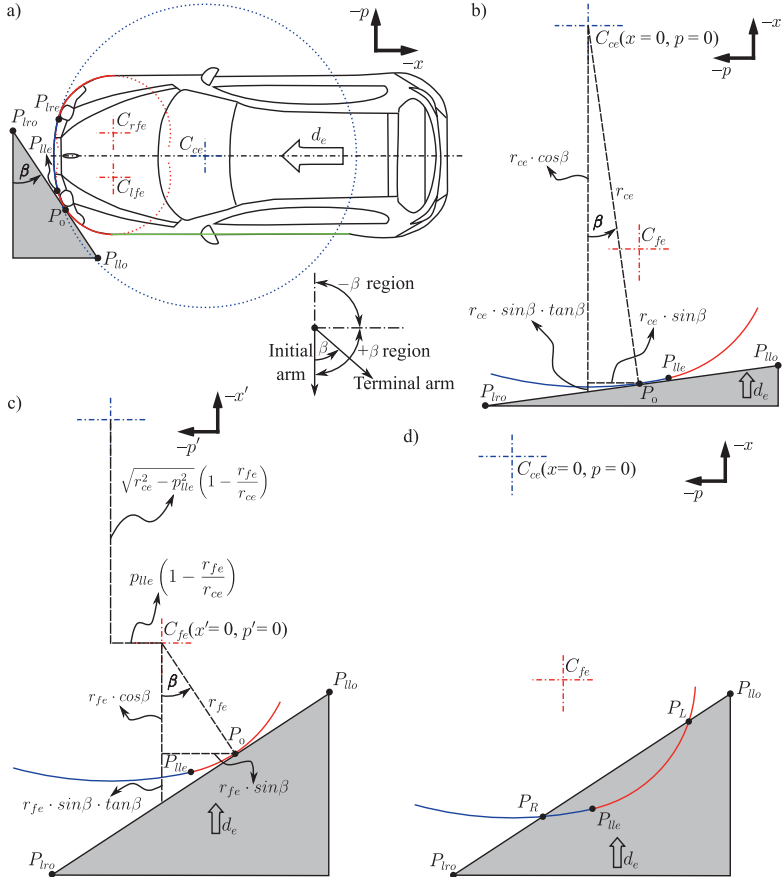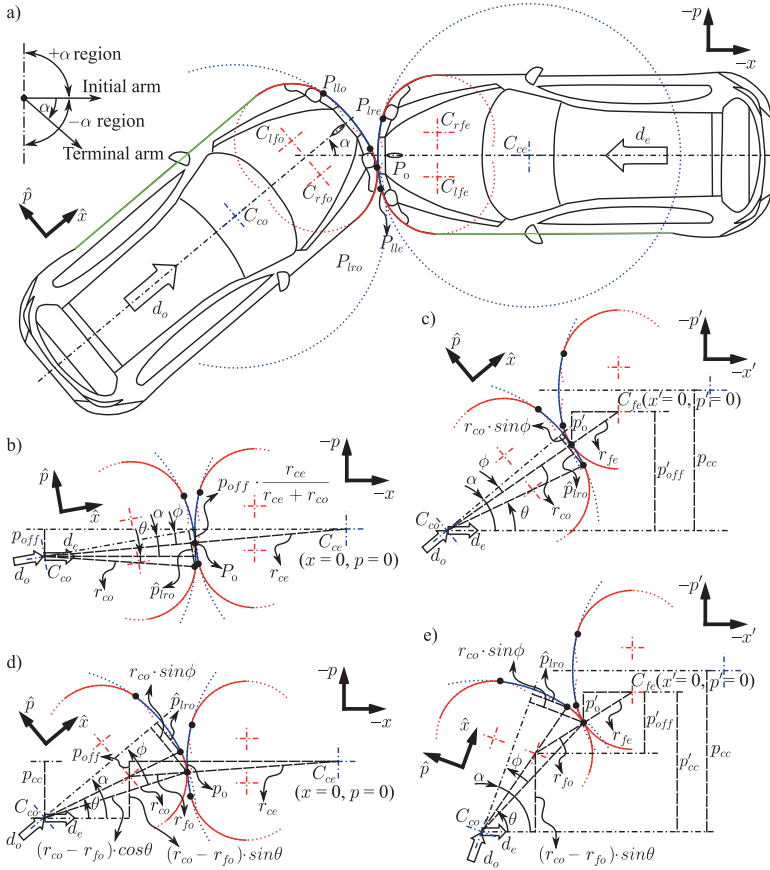
Figure 4.7: Geometrical representation of ego-vehicle colliding against another vehicle: a) geometrical schematic, b) illustration of P_0 in the central-arc region of both vehicles, c) illustration of P_0 in the fillet-arc region of ego-vehicle and central-arc region of the opponent, d) illustration of P_0 in the central-arc region of ego-vehicle and fillet-arc region of the opponent, and e) illustration of P_0 in the fillet-arc region of both vehicles.

the derivation. Hence, the opponent-vehicle is moving with the resultant velocity of both vehicles.

The predicted geometrical parameters of the opponent-vehicle require a def-

inition of a new axis system $\hat{x}$-$\hat{p}$ with the center of the central arc C_{co} of the opponent-vehicle as the origin. As C_{co} is moving, this new axis system is also moving. In this case, the solution for the position of contact points requires the following parameters for representing the opponent-vehicle in addition to the parameters of the ego-vehicle defined in Section 4.3.1.

- r_{co} is the radius of the central arc and r_{fo} is the radius of the arcs representing the headlight region of the opponent-vehicle.

- d_o is the variable representing the displacement of the opponent-vehicle, which can be derived from its velocity.

- p_{cc} is the distance between the center of the central arc of the ego-vehicle and opponent at t_0 measured parallel to p-axis.

- P_0 is the point of contact at t_0 or the initial contact point with p_0 and x_0 as coordinates.

- P_{llo} is the left or driver-side limiting point of the central arc for the opponent-vehicle with $\hat{p}_{llo}$ and $\hat{x}_{llo}$ as coordinates in the $\hat{x}$-$\hat{p}$ coordinate system. It should be noted that $\hat{p}_{llo}$ has a positive value since it is on the driver's side of the opponent-vehicle.

- P_{lro} is the right or passenger-side limiting point of the central arc for the opponent-vehicle with $\hat{p}_{lro}$ and $\hat{x}_{lro}$ as coordinates in the $\hat{x}$-$\hat{p}$ coordinate system. It should be noted that $\hat{p}_{lro}$ has a negative value since it is on the passenger's side of the opponent-vehicle.

- w_o is the width of the opponent-vehicle.

- α represents the angle between the longitudinal axis of both vehicles. This angle is measured from the longitudinal axis of the ego-vehicle (initial arm) to the longitudinal axis of the opponent-vehicle and varies from +90° to -90°. When the angle is measured in an anticlockwise direction it is considered as positive while the clockwise direction is considered as negative (see Figure 4.7a).

For the case of front-to-front collisions of two vehicles, the three regions of both vehicles create nine different possible configurations for the location of P_0. The approach described in Section 4.3.1 for calculating the value of p_0 can be used for this case if the equations for p_{off} in each configuration are known. When P_0 lies

in the central-arc region of the ego-vehicle, p_0 is given by

$$
p_0 = \begin{cases} p_{off} \cdot \dfrac{r_{ce}}{r_{ce} + r_{co}}, & \text{if } \hat{p}_{llo} \geq -r_{co} \cdot \sin \phi \geq \hat{p}_{lro} \\ & \text{i.e. } P_0 \text{ lies in the central-arc} \\ & \text{region of the opponent;} \\[2em] & \begin{cases} \text{if } -r_{co} \cdot \sin \phi > \hat{p}_{llo} \\ \text{i.e. } P_0 \text{ lies in the driver-side} \\ \text{fillet-arc region of the opponent;} \\[1em] \end{cases} \\ p_{off} \cdot \dfrac{r_{ce}}{r_{ce} + r_{fo}}, & \\ & \begin{cases} \text{if } -r_{co} \cdot \sin \phi < \hat{p}_{lro} \\ \text{i.e. } P_0 \text{ lies in the passenger-side} \\ \text{fillet-arc region of the opponent.} \end{cases} \end{cases} \tag{4.61}
$$

Where ϕ is given by

$$
\phi = \alpha - \sin^{-1}\left(\frac{p_{cc} - p_0}{r_{co}}\right) \tag{4.62}
$$

and the equation for p_{off} can be represented by

$$
p_{off} = \begin{cases} p_{cc}, & \text{if } P_0 \text{ lies in the central-arc} \\ & \text{region of the opponent;} \\[1em] & \begin{cases} \text{if } P_0 \text{ lies in the driver-side} \\ \text{fillet-arc region of the opponent;} \\[1em] \end{cases} \\ p_{cc} - (r_{co} - r_{fo}) \cdot \sin \theta, & \\ & \begin{cases} \text{if } P_0 \text{ lies in the passenger-side} \\ \text{fillet-arc region of the opponent.} \end{cases} \end{cases} \tag{4.63}
$$

Where θ is given by

$$
\theta = \begin{cases} \alpha + \sin^{-1}\left(\dfrac{\hat{p}_{llo}}{r_{co}}\right), & \text{if } P_0 \text{ lies in the driver-side} \\ & \text{fillet-arc region of the opponent;} \\[1em] \alpha + \sin^{-1}\left(\dfrac{\hat{p}_{lro}}{r_{co}}\right), & \text{if } P_0 \text{ lies in the passenger-side} \\ & \text{fillet-arc region of the opponent.} \end{cases} \tag{4.64}
$$

If the value of p_0, given by equation 4.61 exceeds the limits p_{lle} and p_{lre}, P_0 lies in a fillet-arc region of the ego-vehicle. In these cases, p_{cc} is shifted to the x'-p' coordinate system as explained in Section 4.3.1 to give p'_{cc}, based on which the

equation for p'_{off} can be expressed as

$$
p'_{off} = \begin{cases} p'_{cc}, & \text{if } P_0 \text{ lies in the central-arc} \\ & \text{region of the opponent;} \\ & \text{if } P_0 \text{ lies in the driver-side} \\ & \text{fillet-arc region of the opponent;} \\ p'_{cc} - (r_{co} - r_{fo}) \cdot \sin\theta, & \text{if } P_0 \text{ lies in the passenger-side} \\ & \text{fillet-arc region of the opponent.} \end{cases} \tag{4.65}
$$

Eventually, the equation for p'_0 can be written as

$$
p'_0 = \begin{cases} p'_{off} \cdot \dfrac{r_{fe}}{r_{fe} + r_{co}}, & \text{if } P_0 \text{ lies in the central-arc} \\ & \text{region of the opponent;} \\ & \text{if } P_0 \text{ lies in the driver-side} \\ & \text{fillet-arc region of the opponent;} \\ p'_{off} \cdot \dfrac{r_{fe}}{r_{fe} + r_{fo}}, & \text{if } P_0 \text{ lies in the passenger-side} \\ & \text{fillet-arc region of the opponent.} \end{cases} \tag{4.66}
$$

Even if P_0 lies in the fillet-arc region of the ego-vehicle, the same conditions (given in equation 4.61) apply to the decision of the arc-region in which P_0 lies on the opponent. The initial position p'_0 can be shifted to the x-p coordinate system using the method explained above.

Consider an example, where P_0 lies in the central-arc region of the ego and the fillet-arc region on the opponent-vehicle as shown in Figure 4.7d. The equation of the central-arc for ego-vehicle is given by equation 4.18, while the fillet-arc of the opponent-vehicle is given by

$$
\left(x - \left(\sqrt{(r_{ce} + r_{fo})^2 - p^2_{off}} - d_o \cdot \cos\alpha - d_e \right) \right)^2 \tag{4.67}
$$
$$
+ \left(p - (p_{off} - d_o \cdot \sin\alpha) \right)^2 = r^2_{fo}.
$$

Substituting
$$
\sqrt{(r_{ce} + r_{fo})^2 - p^2_{off}} - d_o \cdot \cos\alpha - d_e = e \tag{4.68}
$$

$$
\text{and } p_{off} - d_o \cdot \sin\alpha = f \tag{4.69}
$$

in equation 4.67, we get the equation
$$
x^2 - 2ex + e^2 + p^2 - 2fp + f^2 = r^2_{fo}. \tag{4.70}
$$

Substituting equations 4.23 and 4.24 in equation 4.70

$$\pm\sqrt{r_{ce}^2 - p^2} = \frac{e^2 + f^2 + r_{ce}^2 - r_{fo}^2}{2e} - \left(\frac{f}{e}\right)p. \tag{4.71}$$

Inserting

$$\frac{e^2 + f^2 + r_{ce}^2 - r_{fo}^2}{2e} = g \tag{4.72}$$

in equation 4.71, we get equation 4.27 derived in Section 4.3.1. This equation can be transformed into a general quadratic form by squaring on both sides and rearranging (as in Section 4.3.1). The roots of the quadratic equation give the positions of the left and right contact points. For this case in addition to the limits (p_{lle} and p_{lre}) of the ego-vehicle, the limits (p_{llo} and p_{lro}) of the opponent-vehicle should also be considered. But since these limits are acquired in the coordinate system ($\hat{x}$-$\hat{p}$) of the opponent-vehicle, they have to be transformed to x-p coordinate system using the following equations

$$p_{llo} = p_{cc} - r_{co} \cdot \sin\left(\alpha + \sin^{-1}\left(\frac{\hat{p}_{llo}}{r_{co}}\right)\right) - d_o \cdot \sin\alpha \tag{4.73}$$

$$\text{and } p_{lro} = p_{cc} - r_{co} \cdot \sin\left(\alpha + \sin^{-1}\left(\frac{\hat{p}_{lro}}{r_{co}}\right)\right) - d_o \cdot \sin\alpha. \tag{4.74}$$

If the roots exceed the limits (p_{llo} and p_{lro}) of the opponent-vehicle, the corresponding contact point/points shift its arc-region on the opponent-vehicle. For the case shown in Figure 4.7d, the right contact point would shift from fillet-arc region to central-arc region of the opponent when one of the roots is less than p_{lro}. After this shift, the equation of the central-arc region of the opponent should be considered. This equation is given by

$$\left(x - \left(\sqrt{(r_{ce} + r_{fo})^2 - p_{off}^2} + (r_{co} - r_{fo}) \cdot \cos\theta - d_o \cdot \cos\alpha - d_e\right)\right)^2 \tag{4.75}$$
$$+ (p - (p_{off} + (r_{co} - r_{fo}) \cdot \sin\theta - d_o \cdot \sin\alpha))^2 = r_{fo}^2.$$

The above-discussed method can be used to derive the quadratic equation to be solved for the roots of the equation. One of the roots would correspond to the position of the required contact point, in this case, the smallest root since the right contact point shifts in the central-arc region.

When the position of the left contact point is greater than p_{lle}, this contact point shifts from the central-arc region to the fillet-arc region of the ego-vehicle. The position of the left contact point when it shifts in the fillet-arc region can be predicted by considering the equations of the arcs in the x'-p' coordinate system (a method similar to the one explained in Section 4.3.1).

4.4 Investigations of the dynamic behavior of contact points in a vehicle crash

In this section, the dynamic behavior of the change in position of the contact points for the different cases (estimated based on the equations derived in the above section) is analyzed under varying crash parameters. The geometrical dimensions of the ego-vehicle considered for the investigation are derived from the Toyota Yaris Finite-Element-Model (used in Chapter 5 for data generation) and listed in Table 4.3. As mentioned in the caption of Figure 4.8, please note that the dashed line represents the position of the left contact point while the dashed-dotted line represents the position of the right contact point. The results from the investigation for all the above-discussed cases are described below.

Table 4.3: Object parameter values selected for investigation.

Parameter description	Parameter value
Central arc radius (r_{ce} and r_{co})	1438 mm
Width (w_e and w_o)	1695 mm
Driver-side limiting point of central arc (p_{lle} and $\hat{p}_{llo}$)	+ 496.5 mm
Passenger-side limiting point of central arc (p_{lre} and $\hat{p}_{lro}$)	- 496.5 mm
Fillet arc radius (r_{fe} and r_{fo})	536 mm

4.4.1 Case 1: Collision against a circle-based object

To investigate a crash scenario in which an ego-vehicle collides against circular objects, three different opponent radii as given below are considered.

- 125 mm – corresponding to a pole with a diameter of 25 cm used for the frontal pole impact test by IIHS [140]

- 375 mm – corresponding to a medium-size tree diameter found in Germany as per the report published by the Federal Ministry of Food and Agriculture [141]

- 625 mm – corresponding to a large-size tree diameter found in German [141]

During the crash, an initial contact point at t_0 separates into the left or the right contact point. These contact points may lie in either the central arc or fillet arcs of the ego-vehicle and may move from the central arc of the ego vehicle to the fillet arc and vice-versa. Figure 4.8a shows the influence of the change in diameter of the opponent object for central impact (i.e. $p_0 = 0$ mm) and the ego-vehicle traveling at speed of 50 km/h. Since p_0 is at the center of the bumper and the

shape of the opponent object is symmetrical, the left and right contact points move by the same magnitude but in opposite directions. For the opponent object with a radius of 125 mm, the maximum possible position of the contact point (corresponding to the radius of the object) is reached at 9.4 ms. After this time the contact points are considered constant. For the objects with other radii, this limit is not reached and hence the position value of the contact point continues to change. Based on the figure, it can be concluded that depending on the movement of the contact points, information on the diameter of the opponent object can be established.

When p_0 is away from the center of the bumper, the change in the position of the left and the right contact point is asymmetrical and the information about the diameter of the opponent object is more noticeable in the change in position of one of the contact points. This effect can be visualized in Figure 4.8b with p_0 in the headlight region on the driver's side (i.e. +720 mm from the center of the bumper). It can be observed that the information of the diameter can be more easily classified in the position values of the right contact point as compared to the left contact point.

The influence of the ego-vehicle velocity on the position values of the contact point is illustrated in Figure 4.8c. It can be observed that higher velocities cause the contact points to move faster. Hence, the same positions of the contact point are reached earlier as compared to the crash with lower ego-velocity and with all other parameters the same. The effect of the velocity is the same for the other two cases and hence, it is not considered in the below sections.

4.4.2 Case 2: Collision against a line-based object

For line-based objects, its orientation with the ego-vehicle specified by the angle β is an important parameter. For this case, p_0 depends on β (see Section 4.3.2). The effect of β on the position values of the contact points is examined in this section. Three angles (0, 30, and 60 degrees) are considered for the investigation. Figure 4.8d shows that p_0 increases as β increases, indicating that the initial point of contact moves away from the center of the bumper. Moreover, the change in the positions of the right and the left contact point is not the same i.e. asymmetric movement of the contact points. Owing to the increase in angle, the left contact point shows a lower change in position as compared to the right contact point. The negative value of β would also have a similar effect, with the only difference being that p_0 is negative and the right and left contact point interchange their behavior of the change in position.

4.4.3 Case 3: Collision against another vehicle

To investigate this scenario, two cars of similar geometry are supposed to collide front-to-front (head-on collisions) with each other. For vehicle-to-vehicle collisions,
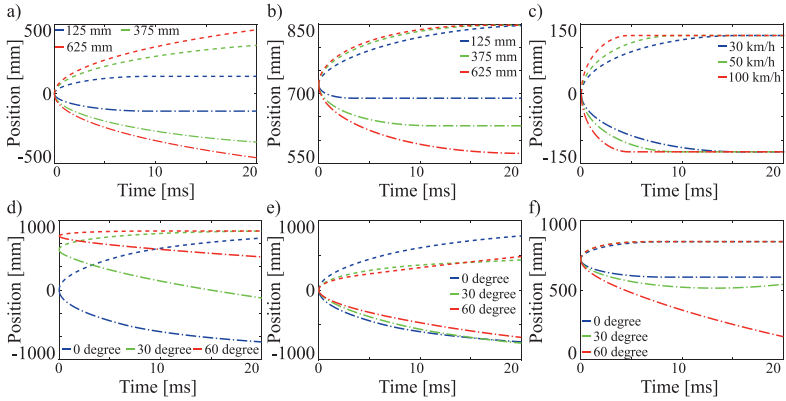
Figure 4.8: Results from the investigations of the dynamic behavior of the contact points in vehicle crash: a) crash against circle-based objects at $p_0 = 0$ mm, b) crash against a circle-based object at $p_0 = 720$ mm, c) crash against a circle-based object with $r_o = 125$ mm at different ego-velocities, d) crash against line-based objects with different angles, e) vehicle-to-vehicle crash at $p_0 = 0$ mm and different angles and f) vehicle-to-vehicle crash at $p_0 = 720$ mm and different angles. (Note the velocity of the vehicles is 50 km/h for all cases except Figure c). Also, note that the dashed line '- - - - -'denotes the position of the left contact point while the dash-dotted line '- · - · -'denotes the position of the right contact point.)

in addition to velocity, the angle α and the initial position of contact are also important.

The influence of the angle (0, 30, and 60 degrees) for $p_0 = 0$ mm and when both vehicles are traveling at a velocity of 50 km/h is shown in Figure 4.8e. Since p_0 is zero, the initial contact point is in the central arc of the ego-vehicle, which may later shift to the fillet-arc region of the ego-vehicle based on the angle. Additionally, the contact points may also transfer from one arc-region to another in opponent geometry for vehicle-to-vehicle collisions and thus change the equations for determining the positions of contact points (as described in Section 4.3.3). For $\alpha = 0$, both the contact points move symmetrically which is lost when $\alpha \neq 0$. In such cases, one of the contact points shows less change in position value as compared to the other (e.g. for positive angles the left contact point shows less change in position, see Figure 4.8e). It can be observed that as the angle increases there is not much difference in the movement of the contact points (see curves for 30 and 60 degrees in Figure 4.8e). This is due to the transfer of the contact points from the fillet-arc region to the side region of the vehicle. When $p_0 = 720$ mm, i.e. at the extreme driver side and all the other parameters are the same as in the above case, there is almost no difference in the position values of the left

85

contact point for different angles (see, Figure 4.8f). But a considerable difference in the position values of the right contact point for different angular scenarios can be observed, which can be used for distinguishing these cases.

4.5 Comparison of geometry-based prediction with the measurements from the crash test

The crash test (discussed in Section 3.4) conducted for verifying the functioning of the proposed contact-based sensor can be represented by a vehicle crash against line-based objects with $\beta = 0$ degree and $p_{lro} = 17.35$ cm (10% of the width of the vehicle, see Figure 4.9a). Since $p_0 = p_{lro}$, the predicted position value of the right contact point p_r is constant throughout the time and equal to p_0. As the sensor is installed in the foam material about 25 mm inside from the outer surface of the bumper, the predicted position values are shifted in time by an amount equal to the distance divided by the crash velocity. The predicted position value of the left contact point p_l is calculated based on the equation derived in Section 4.3.2 and its higher value is limited to a value corresponding to the length of the bumper beam on which the sensor is mounted. In Figure 4.9b, the dotted lines represent the predicted position values while the solid lines represent the position values from the crash test. It can be observed that even though there is a fluctuation in the position values measured in the crash test, the trend of the predicted and the measured curves complement each other.
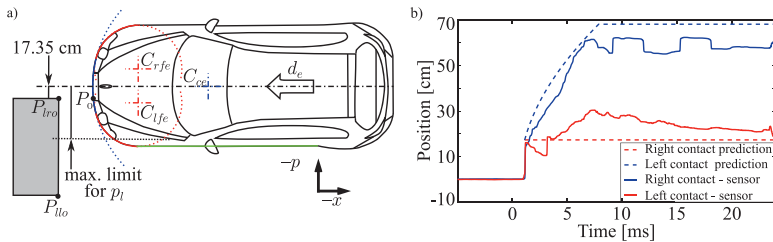
Figure 4.9: Comparison of predicted and measured values of the contact point positions: a) geometrical schematic of crash test and b)Comparison of position values of contact points.

4.6 Summary

From the above discussion, it can be concluded that the dynamic change in the position values of the contact points during the crash includes combined information about the different crash parameters such as object size and shape, velocity,

approach angle, etc. Hence, the truthfulness and the certainty about the prediction from the forward-looking sensors can be achieved by comparing the estimated dynamic change in the position values of the contact point based on these predictions (using equations derived in Section 4.3) with the measured values from the contact-based sensor described in Chapter 3. An example of such a comparison is shown in the above section. The position values of the contact points from the real-world crashes would include the fluctuations from the dynamics of the crash but the overall behavior should match with the prediction. An example of an algorithm to activate the airbags based on the comparison of the predicted and measured values are presented in [2]. Thus a methodology for combined validation of pre-crash information is proposed in this chapter and the exact thresholds for the combined validation are part of a practical implementation as per the choice of the vehicle manufacturers.

Chapter 5

Crash Severity and Restraint Strategy Prediction

Abstract

Crash severity and restraint strategy prediction using the pre-crash information is the spotlight of this chapter. This chapter is introduced with a description of the general idea with an example of a driving scenario, followed by the background knowledge to familiarize the readers with the topic of crash severity. Data being the basis of any machine-learning-based prediction model, a lot of effort and time was spent in collecting the volume of data required for the models investigated in this chapter. The data generation section explains the methodology and the adopted procedure for collecting the data at the two different levels (vehicle and occupant simulation level) with pictorial representations for ease of interpretation. Next, the architecture of the crash severity and restraint strategy is explained with the different building blocks of this architecture. In the next section, the investigation of the different machine learning models with the procedure for training and results is explained in detail. The results from the investigation demonstrate the potential and feasibility to use machine learning models to predict the crash severity parameters and also a particular safety strategy (parameters for activation of airbags) for the crash scenario identified by the forward-looking sensors. After displaying the results from the investigation of the different models, a concept for the algorithm of the concerned system is explained with the help of a flow chart. Finally, the chapter is concluded with a summary and possible future work on this topic.

A brief history of the innovations in the field of vehicle safety and the prospects are presented in Chapter 1. As mentioned previously in the Introduction Chapter, different governmental bodies are striving toward achieving the aim of Vision-Zero, which continuously inspires industries and researchers to search for new advanced methods and techniques to reduce fatalities. One approach with great potential to enhance vehicle safety is a combination of active and passive safety systems into one integrated system such as PCSS, which comprises of different subsystems (see 1.3) with a collection of these advanced methods and techniques. Crash severity and restraint strategy prediction is a vital part of this system, especially since the decision about the safety action for reducing the injuries is based on

the information provided by this sub-system. This chapter presents a unique methodology using data-based approaches and its investigation with a focus on driver injuries in the case of head-on collisions in regard to the above-discussed subsystem of PCSS.

5.1 Basic Idea

A general idea of the application of the crash severity and restraint strategy prediction is portrayed in Figure 5.1 using a driving scenario. The figure shows a driving scenario with the white car as an ego-vehicle and 5 opponent objects (two passenger cars, two pedestrians, and one cyclist) in the surrounding. The trajectory planning and inevitability module gives information about whether the collision with the objects is inevitable. The objects with which the collision of ego-vehicle is inevitable are termed as critical with a flag 'C' for criticality, as shown for the blue car in Figure 5.1. Only the critical objects are chosen for crash severity and restraint strategy prediction. The crash severity and restraint strategy prediction module predicts the requirement of activation of restraint systems such as airbags and their respective activation time windows for a predefined number of possible combinations of trajectories given by the trajectory planning and inevitability module. This information can be conceptualized as a restraint strategy matrix of ego-vehicle and concerned opponent trajectories. Each cell of the matrix contains information about the action required for all the restraint systems equipped in the ego-vehicle. For example, the figure considers 4 trajectories (T1, T2, T3, and T4) of ego and opponent-vehicle, where some combinations of trajectories lead to low severity crashes and hence do not need activation of any airbags (flag: 'N'- not required, for both airbags). However, some trajectories result in medium to severe crashes. Therefore, either driver airbag (DAB) or curtain airbag (CAB) or both are either recommended (flag: 'R') or must (flag: 'M'), with their respective activation times in milliseconds shown in brackets. Similarly, information about the other restraint systems such as passenger airbags, knee airbags, etc. can be included in the cells. Moreover, the driving scenario considers only one critical object for the explanation, there can be more than one critical object simultaneously to be considered. Similar information in the form of a matrix needs to be predicted for all the critical objects at a particular instant of cycle time. When the opponent-object is stationary, the restraint strategy matrix transforms into a vector since there are no trajectories from the opponent-vehicle.

After describing the basic idea with an example of a driving scenario, comprehensive background knowledge of vehicle safety is given in the next section to clarify the underlying concepts of vehicle safety.
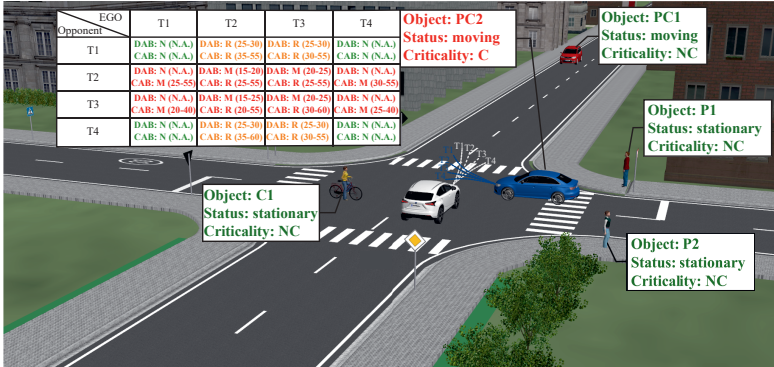
Figure 5.1: A critical driving scenario demonstrating the importance of crash severity and restraint strategy prediction in the pre-crash phase. The white car is the ego-vehicle and all other objects are opponents. The dark green color is used for non-critical objects and trajectories leading to No-Fire scenarios, the orange color is used for trajectories on the boundary of No-Fire and Fire scenarios, and the red color is used for critical objects and trajectories leading to Must-Fire scenarios.

5.2 Background

A vehicle crash is usually classified based on the location of the impact or the state of the vehicle such as frontal, rear, side, and rollover crashes. Statistics show, based on [142], that the largest percentage of occupant deaths are caused by frontal crashes (about 57%). Moreover, head-on collisions have higher severity compared to other frontal collisions. Hence, this thesis is primarily focused on head-on frontal crashes. The physics in a vehicle crash is based on Newton's law of inertia "An object will continue to be in a state of motion or a state of rest unless acted on by an external force".

In a vehicle crash, the motion of the bodies is disturbed by the three types of collision events as shown in Figure 5.2.

- The first collision event takes place between the ego-vehicle and the opponent (tree, vehicle, wall, etc.). This collision causes damage to the vehicle structure and also results in sudden deceleration or acceleration of the ego-vehicle and thus, resulting in the occupant's motion with respect to the vehicle.

- The second type of collision event is the collision between the occupant's body parts and the interior of the vehicle. The impact from the collision produces a shock wave causing stress and strain in tissues and organs leading to damage to the cells.

- Human body consists of a large number of internal organs. Some of these
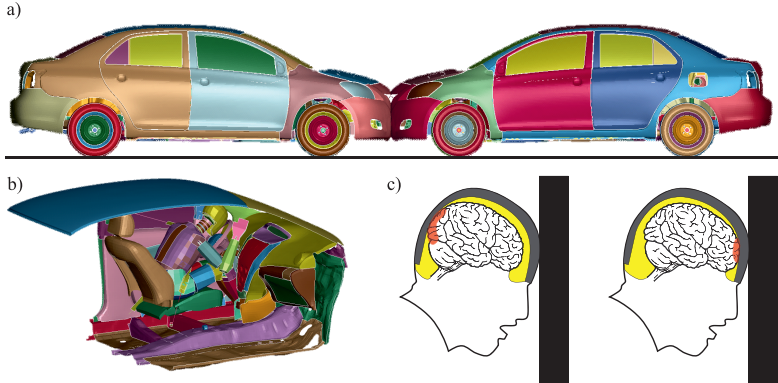
Figure 5.2: Three different types of collision in a vehicle crash: a) vehicle to opponent collision, b) occupant collision against vehicle interiors, and c) collision of internal organs (the grey area represents the skull, the yellow region is the spinal fluid in which brain is suspended, and the red region represents the injury). The rear injury to the brain is caused by the impact while the front brain injury is due to the rebound.

> organs such as the brain, lungs, etc are suspended in fluids. Similar to the occupant's motion due to the sudden acceleration or deceleration of the vehicle from the impact of the collision, the suspended organs will also move due to the sudden acceleration or deceleration of the occupant's body parts. An occupant can be injured not only by the collision of his/her body parts with vehicle interiors but also by the collision of the internal organs with their surrounding body parts (for example collision of the brain with the skull, lungs with the rib cage, etc.). Figure 5.2c illustrates the collision of the brain with the skull.

The complete field of passive safety is founded on how to make the impacts from the above three types of collision softer to safeguard the occupants. The different methods to safeguard the occupants are discussed in the below first two subsections, while the third subsection gives the details of the different occupant injury metrics.

5.2.1   Vehicle structure

The first idea to make an occupant safe in a vehicle accident was from Béla Barényi, one of the pioneers in passive safety development. He observed that some materials are soft and easy to deform, while others are rigid. He used this property of materials and designed the front and back of the vehicle with soft materials that

can deform and absorb the energy from the crash and named these regions a crumple zone, while the middle portion is termed as a passenger cell or safety cage from the rigid materials to protect the passengers. Later, with the technological development and the need for enhancing vehicle safety, softer materials such as foam were incorporated between the bumper beam and bumper (see Figure 3.3), especially to safeguard pedestrians in low-velocity crashes.
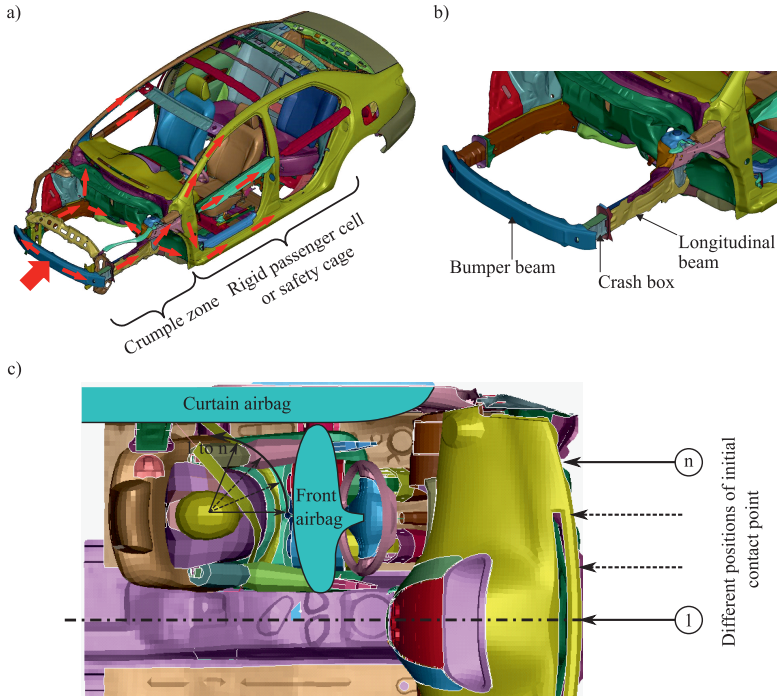
Figure 5.3: Generic structure of vehicle: a) energy transfer paths under frontal loading conditions and b) front crash management structure.

Figure 5.3a and b display a generic vehicle structure with red arrows indicating the energy transfer paths from a frontal crash loading condition. The so-called crumple zone includes the bumper beam and crash boxes, which are designed to absorb energy by deforming in a specially designed manner. In the case of a crash with energy higher than the limit of the energy-absorbing structures, the remaining energy is transferred through the longitudinal beams to the member of the passenger cell such as the sill, door members, A-pillar, etc. The passenger cell is made from stiff materials to avoid large deformation to safeguard the occupants.

However, the first idea based on the structural design of the vehicle can safeguard the occupants from low-velocity crashes, and thus supplementary systems are required to protect the occupants from medium-to-high velocity crashes which are described in the next subsection.

5.2.2 Restraint systems

In the event of a crash, the other systems which play a key role in reducing injuries by safely slowing down the occupant are restraint systems. These systems are associated with the second collision type, i.e. collision of the occupants with the interior of the vehicle. The focus is to keep the resultant forces on the occupant body, to a minimum possible level to mitigate the injuries. The two types of restraint systems used in the vehicles are described in the paragraphs below.

Seatbelt: This is a device designed to secure the occupants and restrain their motion in the event of a collision or sudden braking. According to the National Highway Traffic Safety Administration (NHTSA), three-point seatbelts reduce the risk of fatality by 45% for front-seat occupants and 44% for rear seat occupants [143]. Additional systems, known as pre-tensioners and load limiters are also installed to improve the effectiveness of seatbelts. When the seatbelts are equipped with these systems, there is an active intervention during crash scenarios. The pre-tensioner retracts the seatbelt and then proceeds to remove the slack as soon as the system senses a crash. The retractor or the load limiter keeps a check on the resultant force acting on the occupant's body due to the restraining action of the pre-tensioners and slackens the belt if the force exceeds a threshold. In cars, seatbelts equipped with pre-tensioners and load limiters have an estimated 12.8 percent reduction in fatality risk as compared to regular seatbelts [144].

Airbag: It is a supplementary restraint system that helps to slow down the occupant in addition to the seatbelt. Airbags of different forms, shapes, and sizes are installed at different places inside the vehicle. Frontal airbags installed in the steering wheel and dashboard, side airbags which include curtain airbags in side-pillars, and torso airbags placed inside seats are some of the common types of airbags used. Traditional airbags are activated by the airbag control unit based on different algorithms. Upon receiving an activation signal, the inflator ignites the propellant to start a pyrotechnic process. This process generates a pulse of gas that rapidly inflates an airbag (within 25-35 ms for driver airbag and 30-50 ms for passenger airbag).

5.2.3 Occupant kinematics and injuries

Occupant kinematics covers the analysis of how an occupant's body moves in relation to the movement of the vehicle. During a crash, the vehicle may decelerate rapidly or make an unexpected lateral movement, depending on the type of colli-

sion. In such cases, if the body of the occupant tends to stay in relative motion, it will collide with the vehicle's interior components such as steering, dashboard, inside door panel, etc. unless the restraint system prevents them from doing so. At high-velocity collisions, the time required for the occupant to travel to the surface of a fully inflated airbag might be less than the time required to detect a crash, fire, and fully inflate the airbag (about 45 to 50 ms after t_0 - first contact time). While in some low-velocity crashes, the occupant might require more time to reach the airbag surface than the deflation time of the airbag (about 150 to 200 ms after t_0). Hence, the airbag activation time should depend on the occupant's motion. Further, the direction of occupant motion within the safety cage depends on the position of impact (see Figure 5.3) and the relative approach angle. In some crash scenarios, the occupant might travel diagonally toward A-pillar in the safety cage which might lead to severe or fatal injuries unless the curtain airbag is fired in combination with the frontal airbag. Hence, occupant kinematics is also important in deciding the best occupant restraint strategy.

Researchers, governmental agencies, and automotive companies use crash test dummies (such as THOR, Hybrid III, etc.) to predict the injury of an occupant in a vehicle crash. A 50-percentile Hybrid-III dummy representing an adult male occupant is the most widely used dummy in frontal crash tests. These dummies include several sensors at specific locations on body parts to measure variables such as deceleration, crushing force, bending moment, the velocity of impact, etc. Based on these measured variables, injury criteria for different body parts are calculated [145]. These criteria for different body parts are explained below.

Head: The risk of head injury is mainly evaluated using the head injury criterion (HIC). This criterion is calculated from the resultant head acceleration of the occupant using the following formula

$$\text{HIC} = max\left[\frac{1}{t_2 - t_1} \int_{t_1}^{t_2} a(t)\right]^{2.5} (t_2 - t_1) \tag{5.1}$$

where $a(t)$ is the resultant head acceleration, t_1 and t_2 are the chosen initial and final times. The time duration $(t_2 - t_1)$ is limited by the type of criteria selected (for e.g, 36 ms for HIC-36 and 15 ms for HIC-15). Another measure of head injury is the A-3ms criterion, which is the maximum resultant acceleration of an occupant for a duration of 3 ms. This value distinguishes between hard and soft head contact.

Neck: The injury risk for this body part is determined by shear force, tension force, and extension moment. The neck shear and tension forces have time-based cumulative limits.

Chest: The evaluation of the chest injury risk is done based on two criteria. The chest compression or deformation in millimeters is the first criterion. It gives an idea of overall injury to the chest. The assessment of injury is done by consid-

ering the maximum value of chest compression. The second criterion is called as Viscous Criterion (VC) which predicts the soft tissue injury induced by impact. VC is given by the following equation

$$\text{VC} = sf \cdot V(t) \times \frac{D_{chest}(t)}{D_{constant}} \qquad (5.2)$$

where sf is the scaling factor (1.3 for 50-percentile Hybrid III dummy), $V(t)$ is the velocity of chest deformation, $D_{chest}(t)$ is the chest deformation, and $D_{constant}$ is the depth of half the rib cage (229 millimeters for 50-percentile Hybrid III dummy). The maximum value of VC is considered for evaluation.

Pelvis and upper leg: The compressive force on the femur and the knee displacement in millimeters are the criteria considered for these regions of the body.

Lower leg: The lower leg injury is examined using the Tibia Index (TI). TI is calculated based on the following equation

$$\text{TI} = \left| \frac{M_r(t)}{(M_r)_C} \right| + \left| \frac{F_z(t)}{(F_z)_C} \right| \qquad (5.3)$$

where $M_r(t)$ is the resultant bending moment of the tibia, $(M_r)_C$ is the critical bending moment, $F_z(t)$ is the compressive force on the tibia, and $(F_z)_C$ is the critical compressive force. Additionally, the compressive force on the tibia is also examined separately for their respective limits.

New Car Assessment Programme (NCAP) from different regions have mentioned the upper and lower limits for the injury criteria of different body parts in their protocols [146] and [147].

5.3 Data generation

Data is the core of any data-based prediction system. As described in the last paragraph of Section 2.6 of Chapter 1, the available crash databases based on police reporting are inadequate and lack the information to train the required prediction models. Hence, it was necessary to generate the data rather than using the available public database sources. Crash tests resemble real-world scenarios and thus performing crash tests is an ideal method to generate data. However, based on the volume of the data required for the concerned prediction problem, the resources required for performing such a large number of crash tests are humongous and thus the crash tests are economically infeasible for data generation. Simulations can serve as an alternative to crash tests for the process of data generation. There are various approaches with which the crash simulations can be implemented [104]– [107], [148]. Although the mass-spring-damper and momentum-based simulation approaches require less computing resources and time for data generation, they

cannot portray the complex physical behavior such as deformation of the structural parts, rotational responses (pitch, roll, and yaw rates), etc. in a vehicle crash. It is possible to set up simulations with input features (crash parameters) varied in desired steps using Finite Element Method (FEM) based simulations to extract the required output parameters for building the database. Moreover, the physical behavior presented by this simulation method is analogous to a real-world crash. Consequently, FEM based simulation method was chosen for generating the data.
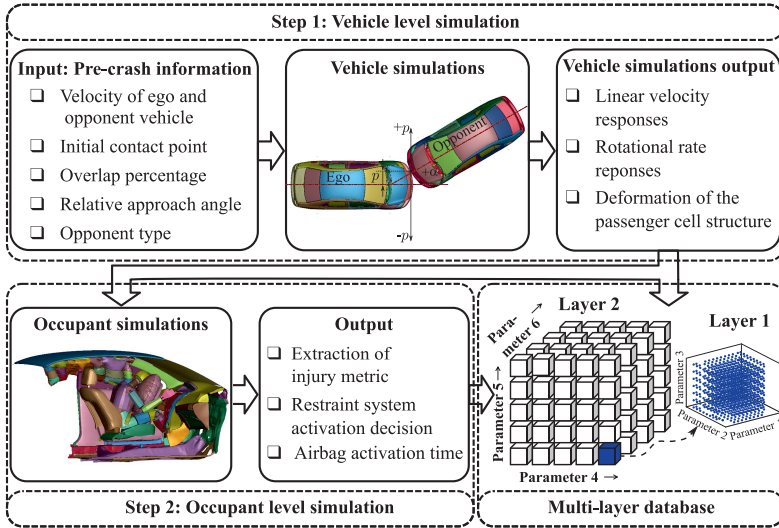
Figure 5.4: Two-step FEM-simulation methodology adopted for data generation.

5.3.1 Methodology

Figure 5.4 shows a two-step simulation methodology utilized for generating the data required for training and testing the prediction models. The advantage of using a two-step approach is the reduction in time, computing resources, and efforts by simulating the complexities of a vehicle crash just once for a particular crash scenario and transferring the results from the vehicle simulation to less complex and fast occupant level simulations where the different combinations of the airbag timings are investigated for its relation to occupant injuries. Another advantage of this approach is that once new smarter restraint systems are developed in the future, they can be easily incorporated into the occupant level model without simulating the complex and time-consuming vehicle level simulations to

upgrade the database and thus the prediction models.
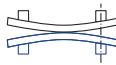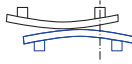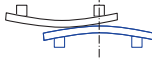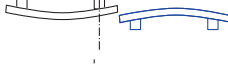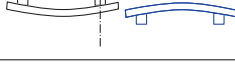
The data generated through this methodology is stored in a form of a database. The bottom left of Figure 5.4 shows an illustration of the database with two layers (considering three input parameters on each layer) as an example. Each of the blue data points in layer 1 contains information about the crash severity which has to be predicted. The three dimensions of the inner core layer (layer 1) are the major influencing parameters. These influencing parameters define the severity regions in the 3-dimensional space and thus the required safety actions and their timing. The outer layer (layer 2) includes the parameters such as the type of opponent-object (car, SUV, truck, bus, pole, tree, wall, etc.), occupant positions, road, and environmental conditions. These parameters have an indirect relationship with the crash severity. For example, a car-to-car crash might have completely different physical behavior as compared to a car-to-pole crash. This illustrated concept can be extended to a greater number of dependent parameters or reduced to a lesser number of dependent parameters as per the required complexity. In the context of this thesis, the data is generated considering the pre-crash information such as the initial position of impact, approach velocity, and relative approach angle as parameters of the inner layer with a similar vehicle as an opponent-object.

5.3.2 Vehicle level simulations

A crash simulation representing the vehicle responses and the deformation to the required accuracy needs a validated vehicle model with complex details such as vehicle structure comprising of different parts and their material models, contacts, spots welds, etc. The 2010 Toyota Yaris model [149] provided by the Center for Collision Safety and Analysis (CCSA) of George Mason University was used for this purpose. The same vehicle model was used as ego and opponent vehicles. The vehicles were arranged by using translation and rotation movements to build the required crash scenarios in the simulation environment.

Different crash scenarios are simulated to acquire the data for the training and testing set. Since the training data set should learn the behavior and the relation of the output parameters corresponding to the input parameters, evenly distributed input parameters were considered for the training data set. A front crash loading can be conceptualized as a static mechanics problem of a beam supported by two fixed points (crash boxes) with a point load at the position of impact. The ideal case would be with the impact point at the center distributing equal force on both the crash boxes and the worst case would be the impact point outside one of the boxes (small overlap crash scenarios). Based on this conceptualization of the front crash structure, 13 different positions of the initial contact point specified in Table 5.1 were chosen. The relative approach angle (α) was varied from -75 to +75 degrees with a step of 15 degrees to give 11 angular variations. A head-on collision is geometrically not possible at some extreme positions of the initial contact point and relative approach angle configurations due to the front curvature of the vehicle. Thus, 131 different crash scenarios for a particular velocity combination of ego

Table 5.1: Specifications of the positions of the initial contact point chosen for the simulations. Note that only the central and the positive positions are mentioned, the value of the negative positions are the same as the positive positions but has a negative sign indicating a passenger-side impact. The normalization of the position is done with the half-width of the ego-vehicle. The crash structure with blue lines represents the ego-vehicle while the structure with black lines represents the opponent-vehicle.

No.	Position	Normalized position	Representation of contact point
P0	0 mm	0	
P1	122 mm	0.14	
P2	245 mm	0.29	
P3	364 mm	0.43	
P4	485 mm	0.57	
P5	636 mm	0.75	
P6	720 mm	0.85	

and opponent vehicles were feasible. The magnitude of the velocity for ego and opponent-vehicle were kept the same and was varied from 20 km/h to 80 km/h in a step of 10 km/h. Altogether a total of $131 \times 7 = 917$ vehicle simulations were simulated for the training data set. In addition to the training data sets, 231 vehicle simulations with randomly chosen input parameters were simulated to form the testing data sets. The number of testing data set was chosen based on the 80%-20% distribution for training and testing data set respectively. The addition of the number of simulations for training and testing gives us 1148 as the total number of simulations. With each vehicle simulation requiring about 4.5 hours for simulation, about 5161.5 hours or 215 days of simulation resources were required just for simulations in the first step.

After performing the simulations, they were checked based on the below-mentioned general guidelines for crash simulations provided by Livermore Software Technology (LST), an Ansys company:

- energy ratio should be close to 1,

- hourglass energy should be less than 10% of peak internal energy, and

- the sliding contact energy should be positive.

After the check process, the linear and the rotational velocities from the center of gravity of the vehicle which represents the overall motion of the vehicle were extracted. These velocities are filtered with the standard vehicle crash post-processing procedure [135] of the low-pass filter (CFC-60 [150]) with a 100 Hz cut-off frequency to remove the unwanted high-frequency components. In addition to the velocities, the nodal deformation of all the parts used in the occupant simulation is recorded with the *INTERFACE_COMPONENT* [151] command during the simulations. The velocities and the recorded deformations were transferred to the occupant simulations in the next step.

5.3.3 Occupant level simulations

For a particular crash scenario (test or training case explained above), the occupant simulation receives the translational and rotational velocity responses and the nodal deformations as inputs to the simulation. The occupant model was created based on the concept of deceleration type of sled test [152], i.e. all the nodes of the model were given an initial velocity equal to the initial velocity of the vehicle simulation, and the velocity responses recorded from the vehicle level simulations were applied at the center of gravity. The occupant model consists of a less complex vehicle sled model (half vehicle model with nodes have predefined motion through nodal deformation transferred from vehicle level simulation), occupant (Hybrid III 50$^{\text{th}}$ Percentile Male Fast Dummy), and restraint systems (seatbelt with a retractor, DAB, and driver-side CAB). The occupant model is described in greater detail in Appendix D. As drivers are more close to the interior of the vehicle (due to the steering wheel) than the other occupants, they are more prone to injuries. Hence, the investigation in the occupant simulations is focused on the driver. This limitation on the occupant was set due to the time and resource constraints required for generating the data for other occupants. The same methodology can be applied to other occupants to develop similar prediction models by learning the behavior from the generated data. The occupant level simulations were performed in three stages (as shown in Figure 5.5) to collect the data regarding the activation of the restraint systems required for the particular and are explained below. Since the activation of the seatbelt retractor is based on the tension force on the seatbelt, it is not required to specifically decide on the activation of the seatbelt and its retractor.

Stage I – Belted simulations: The first stage of simulations was carried out to identify which crash scenarios from the 917 training data and 231 testing data require airbags and specifically which airbags (DAB, CAB, or both). Therefore, in
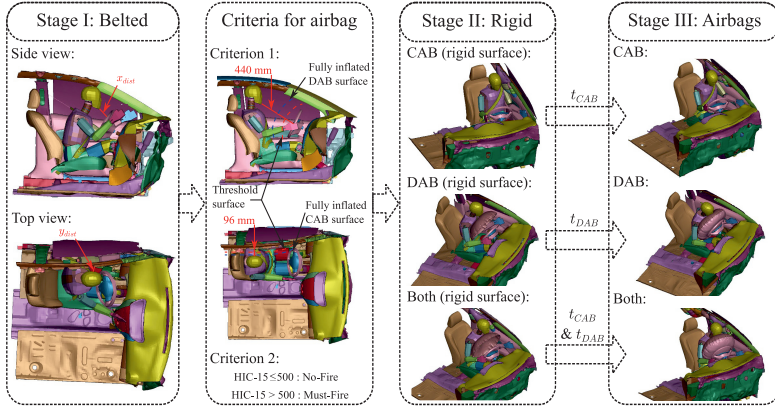
Figure 5.5: Illustration of different stages of occupant-level simulations.

this stage, the simulations were performed with just a seatbelt with the pyrotechnic retractor as restraint systems (both airbags were not included in the model). Two criteria as shown in Figure 5.5 were used to decide on the activation class of the airbag. The first criterion was based on a simple logic based on the travel of the head and whether it contacts the vehicle's interior surface was used for labeling the output parameters related to airbag activation class. The minimum separation distance between the head nodes and the front interior surfaces nodes (minimum of x_{dist} - for DAB) and the similar distance between the head and the side interior surfaces (minimum of y_{dist} - for CAB) were used for labeling the three classes as mentioned below.

- M (Must-Fire) – separation distance is near zero (≤ 5 mm),

- R (Recommended) – separation distance is greater than 5 mm and less than or equal to the threshold value, and

- N (No-Fire) – separation distance is greater than the threshold value.

A recommended class is considered for the cases in which the occupant would travel very near to the interior surfaces to safeguard the occupants against the cases near the boundary of Must-Fire and No-Fire. The threshold value for these boundary cases is the choice of the automotive manufacturer. In the investigations, a $\frac{1}{4}^{th}$ of the initial distance of the head to the interior surface was selected as the threshold value for both DAB and CAB. The values of the initial distance for front and side are mentioned in the criteria block of Figure 5.5 with the lines signifying the fully inflated surface and the recommended threshold surface.

In addition to this, the HIC-15 values were extracted from the belted simulations to take into account the second criterion. This criterion examines head

acceleration-based injuries for airbag activation. These values were classified into two classes as explained below considering the Euro-NCAP evaluation criteria.

- Class 0 - HIC-15 value is less than or equal to 500 (Safe Zone) and

- Class 1 - HIC-15 value is greater than 500 (Injury Zone).

For all the cases with HIC-15 having Class 1, the minimum separation distance of the head from front and side was compared. If the front separation distance was less than the side separation distance, the DAB activation class was changed to M else the CAB activation class was changed to M.

Stage II − Fully inflated airbag surface simulations: After identifying the required airbags (both with M and R airbag activation classes) using the belted simulations, the simulations were categorized as airbags not required, requiring just DAB, requiring just CAB, and requiring both airbags. The simulations which require at least one of the airbags were considered further for the next stage simulations. In these simulations, the fully inflated airbag surface of DAB and/or CAB based on the categorization explained above was included in the belted model. The inflated surfaces of the airbag were modeled as rigid and constrained with their base (steering wheel for DAB and A-pillar for CAB) in the model. The goal of this simulation stage was to derive the initial value for the activation time of the airbags (t_{DAB} for DAB and t_{CAB} for CAB). To calculate this value, the contact time of the head with the airbag surfaces was extracted. This initial activation time was calculated using the following equations.

$$t_{DAB} = t_{ft} - 0.035 \text{ and} \tag{5.4}$$

$$t_{DAB} = t_{st} - 0.030. \tag{5.5}$$

Where t_{ft} and t_{st} are the earliest times when the head comes in contact with the fully inflated DAB surface and CAB surface respectively. 0.035 and 0.030 are the times in seconds taken by the airbags to fully inflate after the activation signal. Additionally, the cases in which the occupant would deflect from contact with one airbag surface towards another (from DAB to CAB or from CAB to DAB) and thus demand a change in the category, were identified. The corresponding change in the category was made and the simulation was repeated to calculate the initial activation time for both the airbags.

Stage III − Airbag simulations: In the final stage of occupant simulations, the required airbag models were included in the belted model and the simulations with different airbag activation times were simulated. Since the CAB does not have vent holes and the deflation of the airbags takes place due to the porosity of the fabric material, it stays inflated for a longer duration as compared to DAB. Thus, the activation time window for CAB is not necessary and the prediction

101

of optimum activation time is sufficient. However, the DAB has a short duration (about 20 to 30 ms) during which the airbag is inflated enough (sufficient airbag pressure) for providing the restraint effect. Hence, for the DAB along with the prediction of optimum activation time, the prediction of lower and upper limit time[1] to define the window for activating the driver airbag is essential. To cater to this need, the simulations with DAB were repeated by varying the DAB activation time in a way to find lower and upper time limits with a resolution of 1 ms.

Each of the stage I simulations required about 10 minutes, each stage II simulation required about 8 minutes, and each stage III simulation required 25 minutes. About 707 cases required activation of DAB out of 1148 crash scenarios considered in the vehicle level simulation. Since approximately 20 simulations were performed for the cases with DAB by varying the activation time, overall about 6419.8 hours or 267.5 days of simulation resources were required for all the stages of occupant level simulation. After each stage of the occupant level simulations, the simulations were passed through the check process and the required data was extracted using a Matlab post-processing code. The data extracted at each stage was stored in a database sheet for further use in the investigation of the machine-learning-based prediction models.

5.4 Crash severity and restraint strategy prediction system architecture

Figure 5.6 shows a probable architecture of a crash severity and restraint strategy prediction system. In addition to the parameters defining the crash scenario (parameters such as p, α, v_{ego}, v_{opp}, etc.), the crash severity and thus the decision of activating the airbags also depend on the mass and stiffness of the opponent or collision partner. The present forward-looking sensors face challenges in accurately predicting both these parameters. One approach to consider these two parameters is to group the available objects in the surrounding into different classes and to relate the detected opponent-objects to a particular opponent class (such as a tree, light truck, heavy truck, small car, medium car, large car, SUV, etc.) based on their size and shape. This consideration assumes that all the objects in a particular opponent class have comparatively similar mass and stiffness. The architecture shown in Figure 5.6 makes use of the same approach for consideration of mass and the stiffness of the opponent-object.

The crash severity and restraint strategy system consists of different prediction models trained for the collision of the ego-vehicle against the different opponent classes possible in the surrounding. Based on the opponent class estimated by the data fusion and object parameter estimation module (refer to Figure 1.3 in Section 1.2), the system selects the corresponding prediction model and sends

---

[1]The lower time limit is the least DAB activation time with the HIC-15 value in the safe zone (i.e. below 500), while the upper time limit is the maximum DAB activation time with the HIC-15 value in the safe zone.
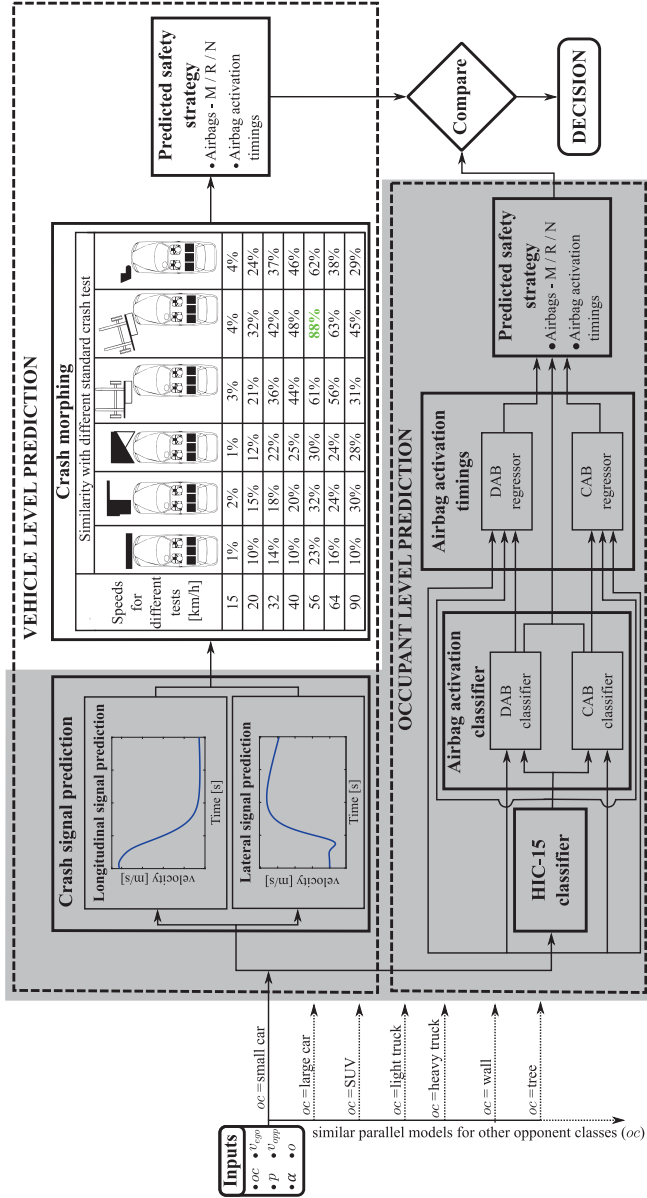
Figure 5.6: Schematic showing the architecture for crash severity and restraint system. In the figure, oc is the opponent class, p is the initial position of impact, α is the approach angle, v_{ego} and v_{opp} are the initial velocities of ego and opponent vehicle, and o is the overlap at the time of initial contact.

the remaining input parameters to the selected prediction model. These input parameters are fed simultaneously to two different levels of prediction for a more robust decision. The first level predicts the vehicle-level responses for the complete crash duration in the crash signal prediction block. These predicted responses are then matched with the responses from the different standard crash tests shown by the crash morphing block. At present, vehicle manufacturers tune the activation of restraint systems (combination of airbags and their respective activation timings) for different crash scenarios by conducting different crash tests. By matching the predicted vehicle responses to these standard crash tests, a safety strategy based on the tuned parameters for the best matching standard crash test can be determined. The second level of the prediction consists of three sub-models based on the occupant kinematics and response in a particular crash. The first sub-model classifies the HIC-15 based on the fed input parameters into either safe or injury regions. This information along with the input parameters is fed to the second sub-model, which consists of different parallel models for each airbag. This sub-model estimates the airbag activation decisions by classifying them into M, R, or N classes (refer to Section 5.3.3) for the concerned crash scenario. In this concept, as an example, only two airbags (DAB and CAB) are shown but this concept can also be applied to more airbags by increasing the number of parallel models in the airbag classification block. The last sub-model predicts the timings for the airbags which need to be activated based on the prediction of the second sub-model. Finally, the decisions of the airbag activation and their timings are accumulated to compare with the prediction from the vehicle level and make a necessary decision. This section describes the concept of the system with the help of a block diagram representing the architecture of the system and more detail on the decision is given in Section 5.5, which describes the algorithm of the concerned system with a flow chart.

The robustness of this architecture comes from the prediction based on the two different approaches used in the two different levels. The vehicle level gives a prediction based on the experimental and manufacturer know-how from the standard crash tests, while the occupant level gives a prediction based on the simulated occupant kinematic response. The shaded region in Figure 5.6 shows the blocks of the system which are investigated in this thesis. The crash morphing block requires confidential data specific to the vehicle manufacturers and thus it was not possible to investigate in this thesis. However, the methods such as the average value of absolute error, the difference in the area enclosed by the two curves, etc. can be employed to get a similarity score or percentage between the predicted responses and the response from the standard tests. Some of these methods are applied in [8] for investigating the accuracy of contour prediction algorithms. In the next section, the results from the investigation of the prediction models represented in the shaded area are briefly explained.

5.5 Investigation of different machine learning algorithms

The data collected through the different levels and stages of FEM simulations were used to investigate the different machine learning algorithms for the task of crash severity and restraint strategy predictions in the next step. During the database generation, the data collected were post-processed and labeled, which necessitates a supervised learning approach for the problem at hand. The goal of the investigations was to check the proficiency and capability of these machine learning methods and to compare the different machine learning algorithms. A two-step (vehicle-level and occupant-level) approach similar to the one used for data collection was adopted for the investigation process. The following subsections discuss these investigations and their outcomes in detail.

5.5.1 Vehicle level prediction model

As described in Section 2.1, present vehicles decide about the activation of the restraint systems during a crash based on the signals measured using different sensors. The basic signals which give a complete picture of the crash are the longitudinal and lateral velocity signals computed during the crash by integrating the acceleration signals. The acceleration signals are measured by the sensor near the center of gravity of the vehicle. Even though these signals give a complete picture of the crash, the present systems have to rely on additional sensors. This is because, in some crash scenarios, the velocity signals are slow to furnish the required indicator necessary to decide about the restraint system activation (refer to Section 3.5.1 in Chapter 3). Since the prediction is done before the crash in the pre-crash phase, predicting these signals would give the behavior of the crash before it occurs.

The decision on the severity of the crash and the required restraint action is taken based on whether the values of derived parameters (ΔV [153], Acceleration Severity Index – ASI [154], etc.) cross their corresponding thresholds. The choice of the derived parameters and their threshold is vehicle manufacturer-specific, confidential, and varies from one manufacturer to the other. Even though the information about the activation of the airbag from the manufacturers is confidential, the studies [155] and [153] give an overview of the probability of the DAB activation corresponding to ΔV. In [154], the ASI value calculated based on the longitudinal acceleration is related to the probability of the Abbreviated Injury Scale (AIS – an anatomical-based coding system) [156]. These studies suggest that in about 50% of frontal collisions with a ΔV value of 3.6 m/s to 4.0 m/s, the DAB was activated. On the other hand, the crashes with ASI values of 1.4 (calculated only on the longitudinal crash pulse) have a 50.8% probability of minor injury and 40.3% of moderate to serious injury. The summary of the results from these studies is given in the table below.

Table 5.2: Summary of the relation of the derived parameters to the activation of DAB or occupant injury [153], [154].

Summary of ΔV study		ASI	Summary of ASI study			
ΔV [m/s]	Probability of DAB deployment		Abbreviated Injury Scale (AIS)			
			Probability of occurrence			
0.9 to 1.3	10%	1.0	0	1	2	3
1.8 to 2.2	25%		20.3%	59.0%	15.4%	5.3%
3.6 to 4.0	50%					
5.8 to 6.2	75%	1.4	0	1	2	3
8.0 to 8.4	90%		9.0%	50.8%	27.7%	12.6%

For investigations, the above-mentioned velocity signals in longitudinal and lateral directions for the crash duration of 200 ms were chosen as the parameters to be predicted. The reason for choosing these signals as the prediction parameter is the flexibility to calculate the different required derived parameters from this parameter after the prediction. This subsection focuses on the potential of machine learning methods to predict the discussed signals in the case of head-on collisions with similar vehicles. The details of the derived parameters and their relation to the activation of the restraint system are out of the scope of this study. Since the outcome of the prediction requires real numbers specifying the velocity values corresponding to their crash duration (time after the first contact), this is a regression problem. Figure 5.7 shows the approach adopted for the investigation of the vehicle-level prediction models. As shown in the figure, another parameter projected overlap (o) at the time of initial contact was considered for the input feature in addition to the initial position of impact (normalized), approach angle, and impact velocities of ego and opponent vehicles. This parameter is different from the overlap (O) measured during the crash by the sensor described in Chapter 3. The difference lies in that o is predicted and has one single value, while O is dynamic and its value changes during the crash with time. The overlap was calculated for each of the simulation cases (training and testing simulations) based on the method adopted by NHTSA [157] and is explained in detail in Appendix E. Another important aspect to be noted is that the input parameters $v_{ego,c}$ and $v_{opp,c}$ are the components of the initial velocity vector. These components are resolved in the lateral or longitudinal direction of the ego-vehicle. The longitudinal components are considered for the longitudinal velocity signal prediction problem, while the lateral components are considered for the lateral prediction. Since the velocity signal to be predicted is for a duration of 200 ms of the crash, the last input parameter for the model is the time instance t in the crash duration from 0 to 200 ms. Thus, just by varying t in the required steps the complete velocity signal for the complete crash duration can be predicted for a particular crash scenario.

Learning phase (data from 917 specially chosen crash scenarios):

Position of inital contact, p
Approach angle, α
Overlap, o
Initial velocity component of ego-vehicle, $v_{ego,c}$
Initial velocity component of opponent-vehicle, $v_{opp,c}$
time instance, t

Training of different machine learning algorithms → Different prediction models
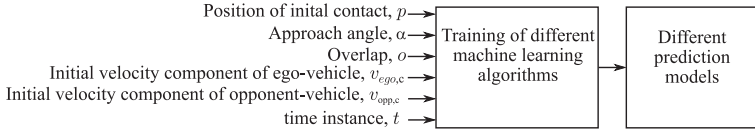
Testing phase (data from 231 randomly chosen crash scenarios):

p
α
o
$v_{ego,c}$
$v_{opp,c}$
t

Different prediction models from learning phase → Predicted velocity signals from different prediction models → Predicted evaluation metric calculation

Ground truth: Velocity signals from coressponding FEM-simulations → True evaluation metric calculation

Evaluation metric comparison → Best suited prediction model
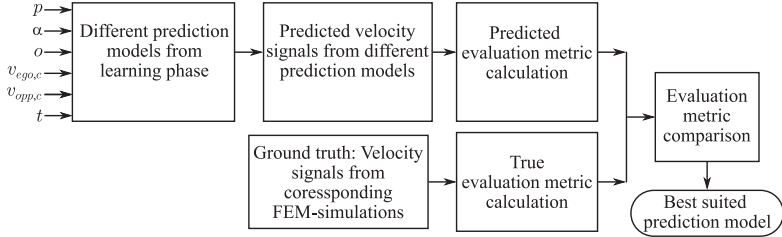
Figure 5.7: Methodology adopted for investigation of the vehicle-level prediction models. A similar investigation methodology is adopted for both longitudinal and lateral prediction, the only change is that for the longitudinal direction the initial velocities of the ego and opponent vehicles resolved in the longitudinal direction of the ego-vehicle are chosen for input parameters, while the laterally resolved velocities are chosen for lateral direction models

Multiple regressors from the most basic and simplest linear regressors to the complex neural networks were trained, optimized, and compared for investigating the concerned regression problem. Four types of regressors namely, linear, decision tree, least-squares boosted (LS-boost) trees, and bagged trees (random forest) were examined. During the training phase, a 5-fold cross-validation approach was used to protect against the overfitting of the data for the regressors. The Bayesian optimization technique was used to optimize the hyper-parameters of each regressor. Additionally, a neural network with two hidden layers each with six neurons which is equal to the number of the input parameters was considered for comparison with the above regressors.

The assessment of the different regressors was carried out in three phases. The metrics used in the evaluation process are well-known statistical terms and do not require any special description or definition. In the first phase, the Mean Absolute Error (MAE) given by the validation process during the training phase was considered for an initial judgment. The data for the validation was chosen from the training data set (917 realizations) to perform a 5-fold cross-validation for regressors other than a neural network. For neural networks, 15% of the 917 realizations in the training data set were randomly chosen for the validation process. It is not suitable to rely just on the judgment from the validation process

Table 5.3: Summary of the evaluation for longitudinal velocity signal prediction

Evaluation phase	Evaluation metrics		Linear	Decision tree	LS-Boost trees	Bagged trees	Neural network
					Models		
Training	MAE [m/s]		2.080	0.170	0.774	0.210	**0.440**
Testing	MAE [m/s]		2.277	0.892	0.812	0.614	**0.473**
	max. +ve error [m/s]		9.731	5.402	4.134	3.053	**3.989**
	max. −ve error [m/s]		-11.314	-10.716	-9.128	-8.451	**-6.772**
Derived crash severity parameters	Error in ΔV [m/s]	MAE	1.082	1.010	1.439	0.917	**0.579**
		max. +ve	3.351	7.580	8.247	6.922	**4.401**
		max. −ve	-7.361	-4.154	-1.489	-2.318	**-2.354**
	Error in ASI	MAE	0.099	0.022	0.021	0.014	**0.011**
		max. +ve	0.249	0.105	0.037	0.032	**0.045**
		max. −ve	-0.024	-0.119	-0.114	-0.102	**-0.054**

and a performance check on the unseen data set through the testing phase is essential for a better assessment. Hence, the second evaluation phase includes the assessment of the trained models on the unobserved testing data set with 231 realizations. In addition to the MAE, the maximum magnitude of the prediction error[2] for both the positive and negative error is assessed. In the final phase, the trained models are tested for their performance to predict the two mentioned crash severity parameters (i.e. ΔV and ASI) by calculating the mean, the maximum positive error, and the maximum negative error using the testing data set.

The results from the assessment of the different prediction algorithms are summarized in Table 5.3 and Table 5.4. It can be observed from the tables that the basic linear algorithm is the worst performing in all three phases of the evaluation for both the longitudinal and lateral prediction problems. The main reason for this is the non-linearity and randomness in the data and the limitation of the linear models to learn this non-linear behavior from the data. Tree-based algorithms (decision tree, boosted trees, and bagged trees) and neural networks achieve a better performance in learning the above-discussed data behavior. The investigation showed that the boosted trees algorithm ranks second-last in most of the evaluation phases. The other methods namely, decision tree, bagged trees, and the neural network give great competition to each other and have relatively close

---

[2]The prediction error in this chapter is calculated by true value minus the predicted value

Table 5.4: Summary of the evaluation for lateral velocity signal prediction

Evaluation phase	Evaluation metrics		Models				
			Linear	Decision tree	LS-Boost trees	Bagged trees	Neural network
Training	MAE [m/s]		0.994	0.156	0.655	0.288	**0.427**
Testing	MAE [m/s]		0.978	0.457	0.622	0.474	**0.424**
	max. +ve error [m/s]		4.920	3.951	5.025	4.432	**3.389**
	max. −ve error [m/s]		-4.585	-5.097	-3.679	-2.942	**-2.845**
Derived crash severity parameters	Error in ΔV [m/s]	MAE	1.041	0.734	1.482	1.114	**0.684**
		max. +ve	3.785	2.771	3.991	4.761	**2.838**
		max. −ve	-5.193	-5.998	-4.408	-4.696	**-5.225**
	Error in ASI	MAE	0.039	0.014	0.020	0.015	**0.013**
		max. +ve	0.103	0.061	0.066	0.068	**0.054**
		max. −ve	-0.122	-0.063	-0.066	-0.062	**-0.055**

prediction performance while comparing the metrics. Even though the decision tree performs the best during the training phase, the bagged trees and neural network algorithms supersede the decision tree in the evaluation during the testing phase. This is more predominantly noticed in the longitudinal velocity signal prediction where the performance of the decision tree is reduced with a larger margin. Similar behavior is also observed in the case of lateral signal prediction but with a comparatively lower margin. Based on the MAE values in the last phase of the evaluation (i.e, comparison of metrics ΔV and ASI), the neural network is better suited for prediction in both directions, with the MAE value in the range of 10^{-1} for ΔV and of 10^{-2} for ASI. Moreover, it also has overall lower magnitudes of the maximum error for both positive and negative errors for ΔV.

For a more detailed examination of the prediction performance, a further error analysis was conducted on the testing data. The counts of the prediction error falling into the different bins with a size of 0.5 m/s for longitudinal and 0.25 m/s for lateral prediction were calculated to plot the histogram. To have a complete overview of the prediction over the crash duration of 200 ms, the error was calculated for each timestamp or sample (2001 samples) of all the 231 testing cases. This gives a total count of 2001×231 (462231 samples) for the prediction error. The histograms for both the longitudinal and lateral prediction of the different prediction models are displayed in Figure 5.8. The neural network regressor shows the
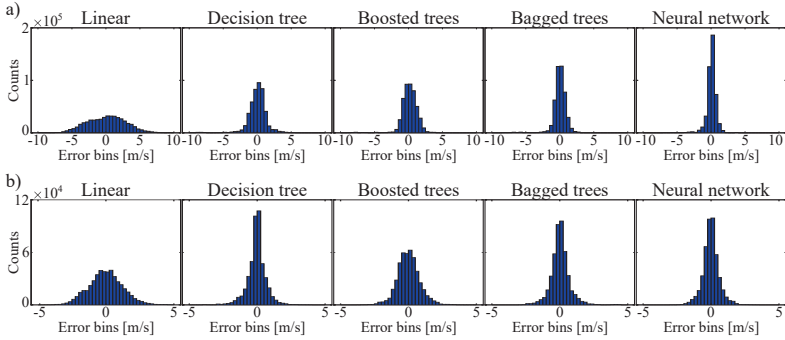
Figure 5.8: Comparison of the performance of the different vehicle level prediction models using histogram plots: a) longitudinal prediction and b) lateral prediction.
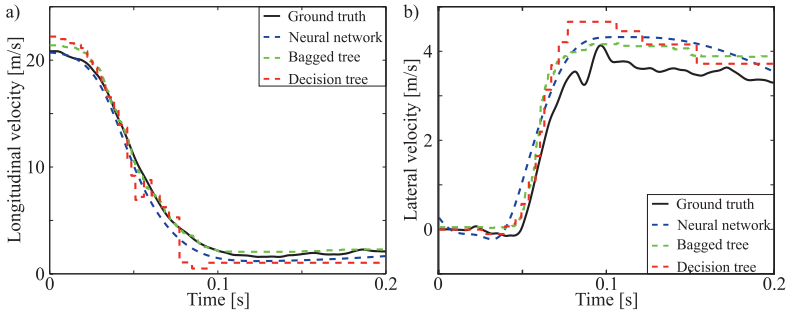
Figure 5.9: Plots showing the velocity signal from FEM simulation (ground truth) with the corresponding predictions from the three better performing models: a) longitudinal prediction ($p = 0.204$, $\alpha = -43°$, and $v_{ego} = v_{opp} = 75$ km/h) and b) lateral prediction ($p = 0.205$, $\alpha = -66°$, and $v_{ego} = v_{opp} = 63$ km/h). Note that the position p mentioned in the caption is normalized.

best overall performance out of the models for both the longitudinal and lateral prediction. About 96.4% of samples have an error magnitude less than 1.5 m/s (including the magnitude of both positive and negative error) for longitudinal prediction, while for lateral prediction about 97.3% of samples fall in the category of error magnitude with less than 1.5 m/s. It can be observed from the histogram, that the performance of the bagged trees and the decision tree is also close to the neural network for the case of lateral prediction but the neural network performs much better for longitudinal velocity signal prediction.

The evaluation would be incomplete without a visual representation of the
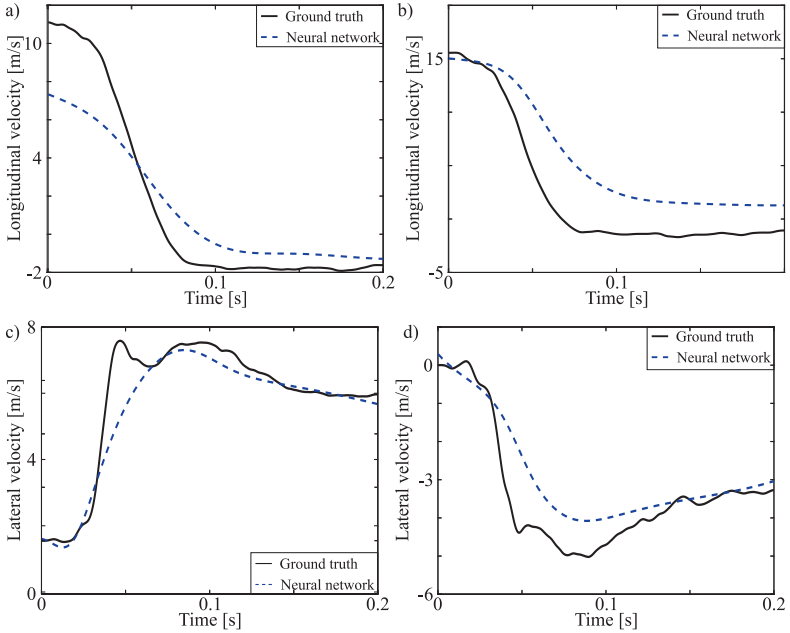
Figure 5.10: Plots displaying the exceptional test cases with maximum error magnitude: a) maximum positive error in longitudinal prediction ($p = -0.192$, $\alpha = 0°$, and $v_{ego} = v_{opp} = 25$ km/h), b) maximum negative error in longitudinal prediction ($p = 0.192$, $\alpha = 8°$, and $v_{ego} = v_{opp} = 56$ km/h), c) maximum positive error in lateral prediction ($p = -0.589$, $\alpha = -33°$, and $v_{ego} = v_{opp} = 75$ km/h), and d) maximum negative error in lateral prediction ($p = 0.491$, $\alpha = 15°$, and $v_{ego} = v_{opp} = 73$ km/h).

predictions from different models and the ground truth (i.e., the signal from the FEM simulation). Figure 5.9 displays the velocity signals of the ground truth together with the predictions from the top three models for longitudinal and lateral directions. It can be observed that all the models accomplish the task of prediction to reasonable effectiveness. The prediction from the decision tree showed a step fluctuating response which is one of the reasons for its lower performance compared to the other models. This problem is solved for the bagged trees since it is an ensemble of different decision trees which reduces this step response by combining the responses from the different decision trees. The response from the neural network was a smooth curve and showed less fluctuation as compared to the ground truth. Even though the predicted signal from the neural network is

not the same as the ground truth, it matches close enough to the ground truth for most of the testing cases. Out of the 231 testing cases, about 4% of exceptional cases were examined with some noteworthy deviation between the ground truth and the predicted signal. Figure 5.10 shows the test cases in which the maximum error magnitude was identified for the neural networks, to illustrate the worst-case prediction example. Even in these cases, the shape of the curve is maintained with the noteworthy deviation in the velocity signal only over some time duration.

5.5.2 Occupant level prediction model

The occupant level prediction model consists of three sub-models as shown in Figure 5.6. The first sub-model deals with the prediction of the HIC-15 class considering only the seatbelt retractor is activated, the second model is further a combination of different classifiers working in a parallel configuration, and the third model is concerned with the prediction of the airbag activation timings. The first two sub-models require approaches for solving the classification problem, while the third sub-model is a regression problem. The metrics used for the evaluation of classification problems are peculiar to the field of machine learning. Hence, a general description of the metrics used is given to familiarize the reader with the machine learning terminology.
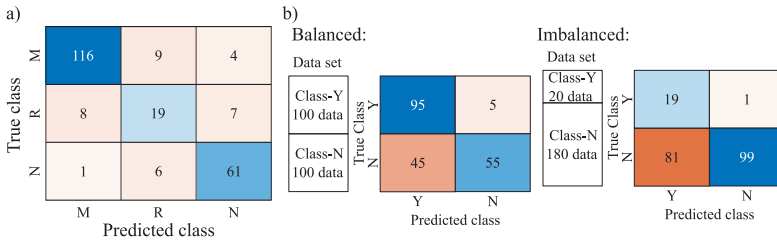
Figure 5.11: Visualization of a confusion matrix for classification models: a) an example of a confusion matrix for a three-class classification problem and b) illustration of the problem of imbalance between classes using a binary classification problem as an example.

The most basic metric which gives a visual representation of the performance of a particular classification model is the confusion matrix. Figure 5.11a shows an example of the confusion matrix structure for a multi-class problem (DAB classification into Must-M, Recommended-R, or No-N). The numbers in the left diagonal which are highlighted with blue color signify the number of true predictions for the particular class, while the numbers in the other cells of the matrix specify the false predictions. The confusion matrix is good for performance visualization but it is difficult to have a direct comparison between different classifiers based on their

confusion matrix. Hence, different quantifiable metrics which are calculated from the numbers in the cells of the confusion metrics were considered in addition to the confusion matrix. The accuracy score is the simplest and the most commonly used metric for a quick comparison, which is given by the following equation.

$$\text{Accuracy score} = \frac{\sum_{i=1}^{n} TP_i}{N} \cdot 100, \tag{5.6}$$

where, TP_i represents the number of true predictions for the ith class, n denotes the total number of the classes, while N represents the total number of realizations. The accuracy score considers all realizations the same and gives a percentage of correct responses. Accuracy score as an evaluation measure can be misleading for the data set with imbalance (the realizations is not equal across the classes). Based on the scale of the class imbalance, the dependence of the accuracy score for the evaluation changes. Consider the problem, of classifying the will of the customers to buy fully autonomous driving into 'Yes' or 'No' as shown in Figure 5.11b. The left example shows a balanced data set case, where the accuracy score for the classifier is 75%. For the example on the right side with 90% of realizations from the customers with the will 'No' and only 10% of data from the other class reduces the accuracy score to 59% which might be misleading. Hence, in the case of an imbalanced data set, a weighted F1-score is a more realistic metric to compare between the different models. This score is a weighted average of the F1-score calculated from each class with weights equal to the counts c_i of realizations in a particular class. The weighted F1-score is given by the following equation.

$$\text{weighted F1-score} = \frac{\sum_{i=1}^{n} \text{F1-score}_i \cdot c_i}{N}. \tag{5.7}$$

The F1-score for a particular class is based on the precision p and recall r of that class and the equation to calculate this score is given below.

$$\text{F1-score} = 2 \cdot \frac{p \cdot r}{p + r}. \tag{5.8}$$

The precision specifies how well the model can predict a particular class from the total realizations in that class, while the recall relates to the sensitivity of the model and is a measure of the correct prediction of a particular class from the total number of predictions of that class. The precision and recall of a particular class are calculated using the equations given below.

$$p = \frac{TP}{TP + FP} \text{ and} \tag{5.9}$$

$$r = \frac{TP}{TP + FN}, \tag{5.10}$$

where, TP, FP, and FN are the true positives, false positives, and false negatives for the concerned class. After having a brief overview of the metrics, these metrics

are used to compare the different classifiers in the upcoming paragraphs. A similar methodology of the learning and testing phase as explained in Section 5.5.1 (Figure 5.7) was used for investigating the different occupant level sub-models, the only difference is the change in the input and the predicted parameters. In all the sub-models, 5-fold cross-validation and the Bayesian optimization technique were used to protect against overfitting and to optimize the hyper-parameters of the models.

Sub-model I – HIC-15 classifier: The HIC-15 related data from the Stage-I simulations (i.e., belted simulation, refer to Section 5.3.3) was distributed in either Safe-Zone (Class 0) or Injury Zone (Class 1) during data collection. Hence, the model to be trained is a binary classification problem. Six features (p, α, o, the longitudinal component of v_{ego}, and both the components of v_{opp}) were considered as inputs for the model. Different classification approaches (regression-based, probability-based, tree-based, pattern-recognition-based, and network-based) employed in the machine learning field were examined for the task of HIC-15 classification. For the network-based model, a single hidden layer with four neurons was found sufficient for the HIC-15 classification problem. Hence a neural network with these parameters was trained and considered for comparison with the other models. The training data set consists of 429 realizations from Class 0 and 488 realizations from Class 1, while the testing data set contains 86 realizations from Class 0 and 145 realizations from Class 1.

Table 5.5: Summary of the evaluation metrics from different classifiers for HIC-15 classification.

Evaluation phase	Metrics		Models						
			Decision tree	Naive bayes	SVM	KNN	Boosted trees	Bagged trees	Neural network
Training	Accuracy [%]		91.40	88.10	92.40	92.10	91.50	92.70	**94.93**
Testing	Confusion matrix		$\begin{bmatrix} 68 & 18 \\ 13 & 132 \end{bmatrix}$	$\begin{bmatrix} 71 & 15 \\ 8 & 137 \end{bmatrix}$	$\begin{bmatrix} 76 & 10 \\ 13 & 132 \end{bmatrix}$	$\begin{bmatrix} 77 & 9 \\ 14 & 131 \end{bmatrix}$	$\begin{bmatrix} 67 & 19 \\ 11 & 134 \end{bmatrix}$	$\begin{bmatrix} 68 & 18 \\ 11 & 134 \end{bmatrix}$	$\begin{bmatrix} \mathbf{75} & \mathbf{11} \\ \mathbf{10} & \mathbf{135} \end{bmatrix}$
	Accuracy [%]		86.58	90.04	90.04	90.04	87.01	87.45	**90.91**
	Class 0	Precision [%]	79.07	82.56	88.37	89.53	77.91	79.07	**87.21**
		Recall [%]	83.95	89.87	85.39	84.62	85.90	86.08	**88.24**
		F1-score	81.44	86.06	86.86	87.01	81.71	82.42	**87.72**
	Class 1	Precision [%]	91.03	94.48	91.03	90.34	92.41	92.41	**93.10**
		Recall [%]	88.00	90.13	92.96	93.57	87.58	88.16	**92.47**
		F1-score	89.49	92.26	91.99	91.93	89.93	90.24	**92.78**
	Weighted F1-score [%]		86.49	89.95	90.08	90.10	86.87	87.33	**90.90**

The evaluation of the different classifiers is carried out in two phases. In the first phase, the accuracy of different classifiers from the validation process during the training is compared, while in the second phase a detailed evaluation is carried out on the testing data set by comparing the different metrics. The metrics
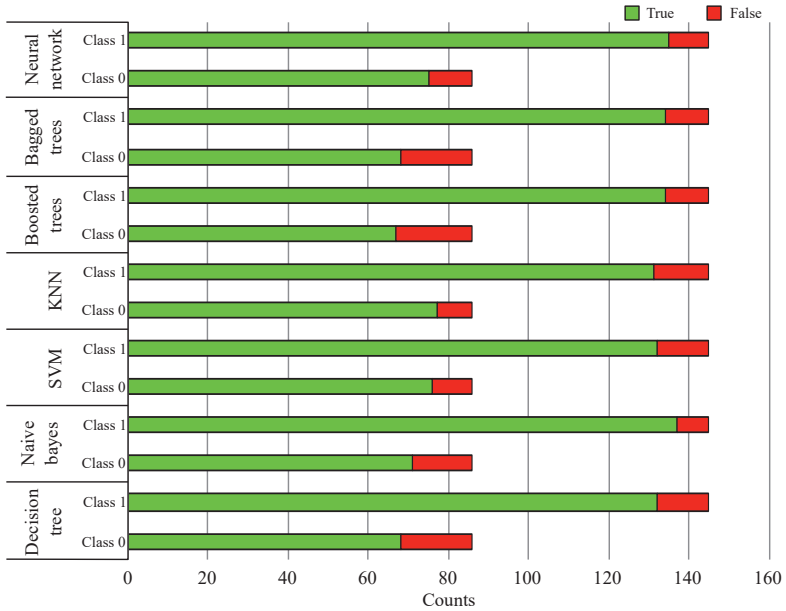
Figure 5.12: Bar graph displaying true and false predictions of the different models for the HIC-15 classification problem.

from the different classifiers in the two phases of the evaluation are listed in Table 5.5. It can be observed that though the tree-based models perform well (with an accuracy score above 90%) in the validation process of the training phase, their score is reduced in the testing phase. Since the F1-Score from both the classes are close to each other demonstrating similar performance to classify both the classes, there is not much difference in the accuracy score and the weighted F1-score from the testing phase. There is close competition between the Support Vector Machines (SVM), K-Nearest Neighbors (KNN), and neural network with all the models having above 90% scores in both the training and testing phases. The neural network wins the competition by a very slight margin and was found to be the best model suited for the HIC-15 classification on the investigated data set. Figure 5.12 displays a visualization of the true and false predictions from all the models using a stacked bar graph.

Sub-model II − Airbag activation classifier: As discussed in Section 5.3.3, the data about the airbag activation for both DAB and CAB were grouped into three classes (M / R / N). Hence, the models to be trained are a multi-class

classification problem. In addition to the six input features considered for the sub-model I, the HIC-15 class was also considered as input for the classification models for airbag activation. The same classification approaches used for investigating the HIC-15 problem were also employed for exploring the airbag classification problem. For the network-based model, a single hidden layer with the number of neurons equal to the number of input parameters was considered to address the complexity of the increased number of classes. The division of the classes in the training data set for CAB was 333, 179, and 405 realizations respective to the classes M, R, and N, while the training data set consists of 69, 45, and 117 realizations from these classes. Similarly, for DAB the number of realizations was 417, 123, and 377 for the training data set and 129, 34, and 68 for the testing data set with respect to the classes M, R, and N.

Table 5.6: Summary of the evaluation metrics from different classifiers for CAB classification.

Evaluation phase	Metrics		Models						
			Decision tree	Naive bayes	SVM	KNN	Boosted trees	Bagged trees	Neural network
Training	Accuracy [%]		76.30	72.00	**76.60**	77.00	77.90	76.3	73.19
	Confusion matrix		$\begin{bmatrix} 59 & 7 & 3 \\ 22 & 16 & 7 \\ 6 & 9 & 102 \end{bmatrix}$	$\begin{bmatrix} 52 & 9 & 8 \\ 23 & 10 & 12 \\ 1 & 7 & 109 \end{bmatrix}$	$\begin{bmatrix} \mathbf{60} & \mathbf{6} & \mathbf{3} \\ \mathbf{22} & \mathbf{16} & \mathbf{7} \\ \mathbf{6} & \mathbf{2} & \mathbf{109} \end{bmatrix}$	$\begin{bmatrix} 59 & 7 & 3 \\ 22 & 15 & 8 \\ 6 & 3 & 108 \end{bmatrix}$	$\begin{bmatrix} 60 & 7 & 2 \\ 26 & 11 & 8 \\ 5 & 10 & 102 \end{bmatrix}$	$\begin{bmatrix} 59 & 7 & 3 \\ 22 & 17 & 6 \\ 8 & 7 & 102 \end{bmatrix}$	$\begin{bmatrix} 48 & 12 & 9 \\ 15 & 20 & 10 \\ 0 & 10 & 107 \end{bmatrix}$
	Accuracy [%]		76.20	74.03	**80.09**	78.79	74.89	77.06	75.76
Testing	Precision [%]	M	85.51	75.36	**86.96**	85.51	86.96	85.51	69.57
	Recall [%]		67.82	68.42	**68.18**	67.82	65.93	66.29	76.19
	F1-score		75.64	71.72	**76.43**	75.64	75.00	74.68	72.73
	Precision [%]	R	35.56	22.22	**35.56**	33.33	24.44	37.78	44.44
	Recall [%]		50.00	38.46	**66.67**	60.00	39.29	54.84	47.62
	F1-score		41.56	28.17	**46.38**	42.86	30.14	44.74	45.98
	Precision [%]	N	87.18	93.16	**93.16**	92.31	87.18	87.18	91.45
	Recall [%]		91.07	84.50	**91.60**	90.76	91.07	91.89	84.92
	F1-score		89.08	88.62	**92.37**	91.53	89.08	89.47	88.07
	Weighted F1-score [%]		75.81	71.80	**78.65**	77.30	73.39	76.34	75.29

The same two-phase evaluation criteria used for assessing the HIC-15 models were used for assessing the performance of the models for airbag classification. A misclassification of 'Class M' is critical because a non-activation of safety action might cause injury to the occupant.'Class R' is a grey region where the activation of the safety action is desirable but a non-activation would not lead to injuries. Though a misclassification of 'Class N' has a lesser probability of fatal to severe injuries, it is not desirable from the repair costs and customer satisfaction point of view. The results from the investigation for both CAB and DAB classification are summarized in Table 5.6 and Table 5.7 respectively. It can be noticed that some of the models have higher accuracy scores during the training phase but their performance reduces in the testing phase. Observing the precision, recall, and F1-scores for each class of the models, it can be inferred that all the models faced difficulty in classifying the 'Class R' where the activation of the airbag is recommended. As explained above since this class is a grey region where the decision on activation of airbags is desirable but a non-activation would not cause

Table 5.7: Summary of the evaluation metrics from different classifiers for DAB classification.

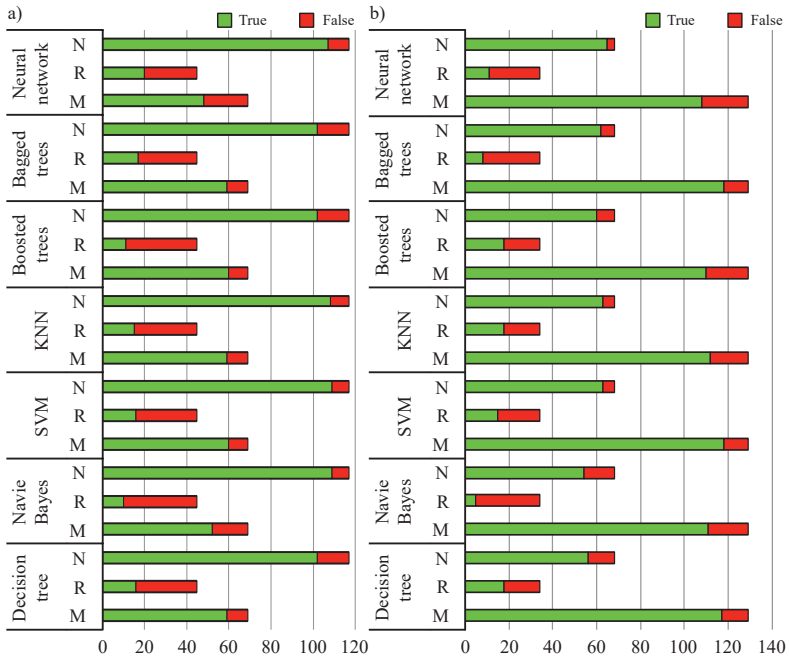| Evaluation phase	Metrics		Decision tree	Naive bayes	SVM	KNN	Boosted trees	Bagged trees	Neural network
Training	Accuracy [%]		84.10	81.20	**84.40**	84.00	84.60	84.30	89.86
	Confusion matrix		$\begin{bmatrix}117 & 11 & 1\\ 9 & 18 & 7\\ 5 & 7 & 56\end{bmatrix}$	$\begin{bmatrix}111 & 5 & 13\\ 13 & 15 & 16\\ 4 & 10 & 54\end{bmatrix}$	$\begin{bmatrix}\mathbf{118} & \mathbf{8} & \mathbf{3}\\ \mathbf{10} & \mathbf{15} & \mathbf{9}\\ \mathbf{1} & \mathbf{4} & \mathbf{63}\end{bmatrix}$	$\begin{bmatrix}112 & 13 & 4\\ 7 & 18 & 9\\ 1 & 4 & 63\end{bmatrix}$	$\begin{bmatrix}110 & 14 & 5\\ 7 & 18 & 9\\ 1 & 7 & 60\end{bmatrix}$	$\begin{bmatrix}118 & 6 & 5\\ 15 & 8 & 11\\ 3 & 3 & 62\end{bmatrix}$	$\begin{bmatrix}108 & 15 & 6\\ 13 & 11 & 10\\ 2 & 1 & 65\end{bmatrix}$
Testing	Accuracy [%]		82.68	81.20	**84.85**	83.55	81.39	83.98	79.65
		Precision [%]	90.70	86.05	**91.47**	86.82	85.27	91.47	83.72
	M	Recall [%]	89.31	86.72	**91.47**	93.33	93.22	86.76	87.80
		F1-score	90.00	86.38	**91.47**	89.96	89.07	89.06	85.71
		Precision [%]	52.94	14.71	**44.12**	52.94	52.94	23.53	32.35
	R	Recall [%]	50.00	25.00	**55.56**	51.43	46.15	47.06	40.74
		F1-score	51.43	18.52	**49.18**	52.17	49.32	31.37	36.07
		Precision [%]	82.35	79.41	**92.65**	92.65	88.24	91.18	95.59
	N	Recall [%]	87.50	65.06	**84.00**	82.89	81.08	79.49	80.25
		F1-score	84.85	71.52	**88.11**	87.50	84.51	84.93	87.25
	Weighted F1-score [%]		82.81	72.02	**84.26**	83.67	81.87	79.35	78.86

Figure 5.13: Bar graph displaying true and false predictions of the different models for airbag activation classification problem: a) CAB and b) DAB.

any impairment, the lower performance of the models to classify this class is not of concern. Since the model performance in the testing phase does not depend on the bias from the training phase, the best-suited model is selected with preference to the scores from the testing phase. For both CAB and DAB classification, SVM performs the best in the testing phase with a prediction accuracy of above 80% and a weighted F1-score above 78.5%. Also, in the training phase, the accuracy of the SVM model is among the better performing models (second highest for DAB and third highest for CAB) from the seven different methods investigated.

Sub-model III – Airbag activation timings: The objective of the last sub-model was to find the activation time for the airbags which are classified as M or R class by the previous sub-model. As discussed in the data generation section (refer to paragraph related to Stage III simulations in Section sec5.3.3), for the CAB only one activation time was considered, while for DAB, three different activation times (optimum, lower, and upper limit time) were considered for prediction. Although the input features considered were the same as the sub-model II, the output parameter (the value of the activation time) of the sub-model III makes it a regression problem. The amount of data available for both learning and testing is not the same as in the previous phases. In contrast to the multiple values corresponding to the time instance in vehicle level prediction, this sub-model has only one prediction value (activation time of the airbag) for a particular crash scenario. Moreover, only those scenarios in which the airbag activation is essential (i.e. scenarios with airbag activation classes of 'M' and 'R') are considered for the prediction of activation timing. The reduced amount of data for this sub-model facilitates the possibility to investigate Gaussian Process Regression (GPR) method in addition to the approaches examined in Section 5.5.1.

Table 5.8: Summary of the evaluation for prediction of CAB activation time

Evaluation phase	Evaluation metrics	Linear	Decision tree	GPR	Boosted Trees	Bagged trees	Neural network
Training	MAE [ms]	14.26	14.70	**12.53**	13.47	13.66	16.90
Testing	MAE [ms]	15.51	15.75	**15.22**	15.45	15.71	15.63
	max.+ve error [ms]	53.19	35.45	**56.45**	50.93	59.99	69.43
	max. -ve error [ms]	-85.70	-104.17	**-108.77**	-115.66	-87.73	-50.39

The summary of the performance investigation of the models for the prediction of the airbag activation timings is given in Table 5.8 and Table 5.9. Although there are some outlier cases with higher error magnitudes, the MAE value which describes the overall performance of the models is below 11 ms for DAB and below 15.5 ms for CAB prediction. Based on the evaluation metrics listed in the tables, the GPR model performs the best for predicting the activation time for both DAB and CAB with its MAE value the least in the testing phase and most of the

Table 5.9: Summary of the evaluation for prediction of DAB activation time

Evaluation phase	Evaluation metrics	Linear	Decision tree	GPR	Boosted Trees	Bagged trees	Neural network
			Upper limit time				
Training	MAE [ms]	12.11	14.05	**10.74**	11.96	12.60	10.43
	MAE [ms]	10.87	11.45	**8.63**	10.42	10.42	9.44
Testing	max.+ve error [ms]	40.94	54.13	**41.62**	46.30	48.36	47.17
	max. -ve error [ms]	-56.54	-55.50	**-34.71**	-39.96	-35.40	-36.24
			Optimum time				
Training	MAE [ms]	11.36	11.38	**10.38**	10.78	10.33	11.65
	MAE [ms]	9.96	10.46	**8.93**	9.56	9.11	9.33
Testing	max.+ve error [ms]	55.66	65.35	**55.28**	54.08	56.92	54.59
	max. -ve error [ms]	-29.22	-27.98	**-26.86**	-24.35	-25.08	-27.24
			Lower limit time				
Training	MAE [ms]	11.89	10.70	**9.11**	10.12	9.42	7.66
	MAE [ms]	8.26	8.21	**6.18**	8.22	6.50	7.81
Testing	max.+ve error [ms]	66.53	76.67	**61.95**	72.64	74.61	78.82
	max. -ve error [ms]	-28.54	-32.33	**-27.84**	-23.88	-21.66	-25.48

training phase. One of the reasons for the better performance of the GPR model as compared to others is its ability to work well with small data sets. Similar to the vehicle level predictions a more detailed examination of the distribution of the error is given by the histogram shown in Figure 5.14. It can be observed from the histogram plots that even though some of the models show a higher count in one of the bins near zero than the GPR model but the counts in other bins compensate for it to enhance the overall performance of the GPR model (which is also indicated by the lower MAE value in Table 5.8 and Table 5.9). The performance of the prediction can be improved by increasing the volume of the data. The increase in the volume of data might give the possibility for the other models to perform better, but the present investigation demonstrates that the GPR model is best suited for the data set under consideration. The investigation also presents the possibility to predict the airbag activation time with uncertainty in terms of prediction error. One method to deal with the uncertainty is to increase the performance of the prediction model by increasing the data volume. The other method is to compare the prediction values by prediction through another approach. One such approach to determine the airbag activation timing by matching the predicted velocity signal with the standard crash test, the so-called crash morphing, is described in Section 5.4.
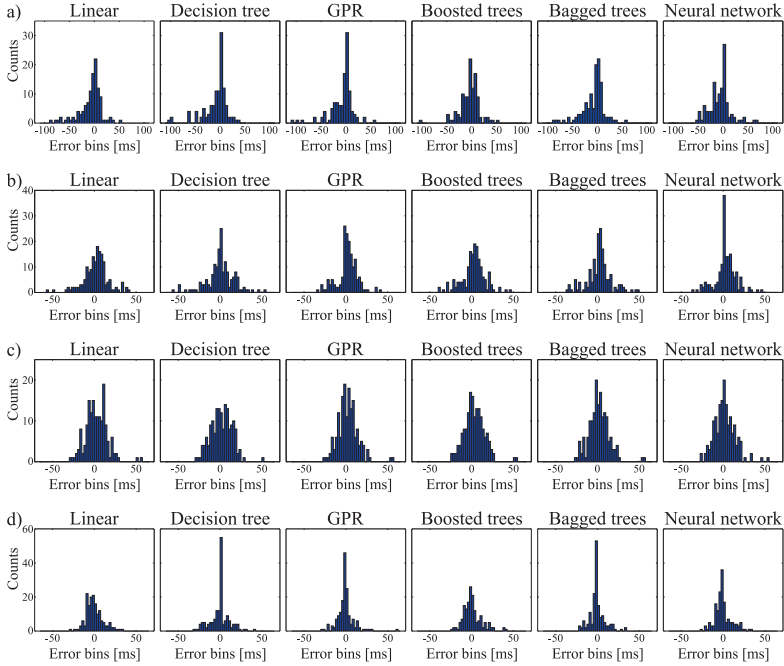
Figure 5.14: Comparison of performance of the airbag activation timing prediction models using histogram plots: a) CAB, b) DAB - upper time limit, c) DAB - optimum time, and d) DAB – lower time limit.

5.6   Algorithm for crash severity and restraint strategy prediction system

In this section, an algorithm for crash severity and restraint strategy prediction system is explained with the help of the flow chart illustrated in Figure 5.15. As explained in Section 6.1, different critical crash constellations or scenarios at a particular time step t are formed by the different critical objects and the combination of the trajectories of the ego-vehicle with the trajectories of these critical objects. A critical crash constellation C_{ijt} is specified by parameters such as the position of initial contact p_{ijt}, the velocity of ego-vehicle $v_{(ego)ijt}$ and opponent $v_{(opp)ijt}$ at the initial contact, the relative approach angle α_{ijt}, the overlap between the ego-vehicle and opponent o_{ijt}, and the opponent class oc_{ijt}. The subscripts i, j, and t represent the critical opponent object, the combination of trajectories from ego-vehicle and opponent, and the time step respectively. The above-mentioned
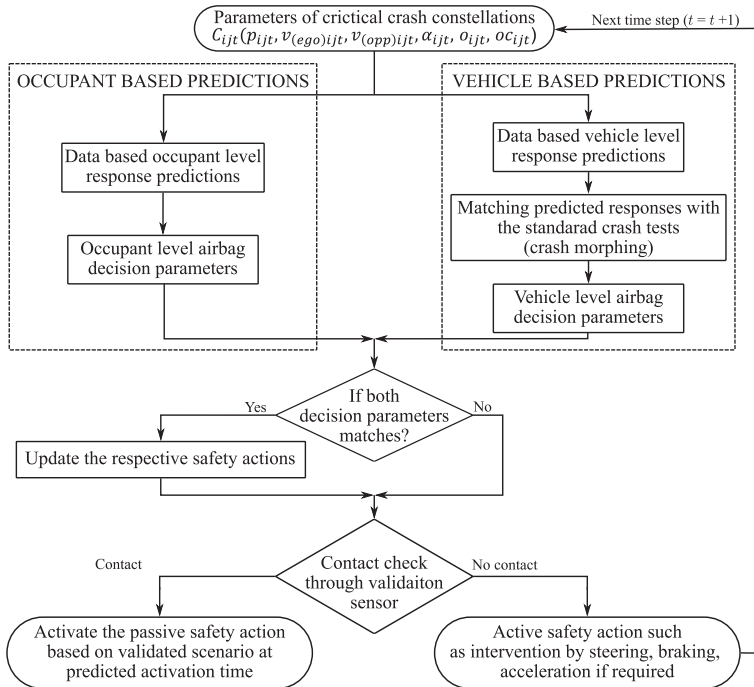
Figure 5.15: Proposed algorithm for crash severity and restraint strategy prediction system.

parameters are considered as inputs to the system, which are fed parallel to both vehicle-based and occupant-based prediction approaches. The outputs (the airbag activation class (M/R/N), the airbag activation time, etc.) from both the estimation approaches are compared with each other for robustness. If these outputs match or are within the acceptable limits, the corresponding safety actions are updated, else they are kept the same. In the next step, the occurrence of the crash is checked based on the contact check through the contact-based validation sensor described in Chapter 3. If no contact is detected, the required active driving interventions (braking, steering, and acceleration) are employed to guide the ego-vehicle towards the scenarios with reduced occupant injuries. Following the active intervention, the complete process is repeated for the next time step. If there is no considerable reduction in the occupant injuries, the active intervention is neglected for the respective time step and the process is repeated. If contact is detected, the passive safety action decision (activation of restraint systems) is

taken based on the predictions corresponding to the validated crash scenario to protect the occupants.

In the above paragraph, a possible concept with the system approach is explained. The detail for the comparison method of the outputs from the vehicle-based and occupant-based predictions approaches is a choice of the vehicle manufacturers and is out of the scope of this thesis. Moreover, other approaches such as physical-based models can be developed to offer another parallel prediction path for comparison to give additional robustness to the crash severity and restraint strategy predictions.

Chapter 6

Conclusion

Upcoming vehicles with partial or full autonomy employ forward-looking sensors to perform some or entire driving task, which is traditionally carried out by the driver. Although the ground-breaking invention of Automated Emergency Braking and other Advanced Driver Assistance Systems has already contributed to reducing fatalities and reducing injuries to a great extent, accidents do happen and also might lead to severe to fatal injuries. Thus, to safeguard the occupants against these unforeseen critical scenarios (inevitable pre-crash situations), the coupling of the information extracted from the forward-looking sensors to the crash severity and the activation of the passive safety systems is a necessity.

This thesis proposes a methodology through the concept of a Pre-Crash Safety System (PCCS) to use the pre-crash information from the forward-looking sensors for taking passive safety decisions in the case of an inevitable crash scenario. The idea is to predict the crash severity and restraint strategy based on the estimated crash parameters (velocity of ego-vehicle and opponent, angular orientation, the position of initial contact, class of opponent object, etc.) and activate the required restraint strategy after the contact-based validation. To supplement this idea, the potential of each of the sub-systems of the PCCS is demonstrated through the results from the experimental and simulative investigations in Chapter 3, Chapter 4, and Chapter 5. The results from the crash test in Chapter 3 demonstrate the feasibility of measuring the signal from the proposed validation sensor near t_0 and thus achieving the goal of triggering the irreversible restraint systems at near t_0. Moreover, the equations derived for the geometry-based prediction of the dynamic position of the contact points during the crash in Chapter 4 describe the methodology for validating the estimated crash parameters by comparing the prediction with the positions of the contact points measured by the validation sensor. By feeding the estimated crash parameters as inputs to the models investigated in Chapter 5 it is possible to predict the crash severity and required restraint strategy for the predicted crash scenarios in the pre-crash phase and on the validation of a particular crash scenario, the corresponding restraint strategy can be activated.

The studies carried out in this dissertation lays a good theoretical, experimental, and scientific foundation for future prediction-based vehicle safety systems.

The modular-based architecture of the systems allows the feasibility for modification by adding supplementary parallel approaches or modules to enhance the robustness of the prediction.

6.1   Limitations and future work

Although the concept and the methodologies described in this thesis are general, the findings of the study should be considered in light of some limitations. Firstly, the experimental investigations of the validation sensor are carried out with consideration to the frontal crash and the application of the sensor for side crash scenarios might require some structural modifications of side structure to incorporate the sensor. Secondly, the experimental investigation of the methodology for opponent-geometry estimation in Chapter 4 is limited to the three-arc template which is one of the most challenging geometry for estimation in the pre-crash phase. Finally in Chapter 5, due to the enormous resources required, the study was limited to head-on collisions between two vehicles of similar class, while the occupant level investigations were focused on the driver.

An extension of the current study in the future can be addressed to overcome the above-discussed limitations. Additionally, considering the research work carried out in the thesis as a basis the future work can also be targeted towards the series application of the methodologies presented in this thesis. The following are some of the areas which can be considered for future work.

- Cost-optimization and different regulatory tests that are required for the series introduction of the validation sensor in the vehicles.

- Extension of the validation sensors to side crash scenario.

- Enhancement of the geometry estimation algorithm to accommodate shapes from other opponents and real-time implementation of the geometry-estimation algorithm.

- Extension of the crash severity and restraint strategy prediction methodology in the first phase to crash scenarios with opponents with other classes and ultimately in upcoming phases to incorporate other crash scenarios to cover a complete 360°prediction.

6.2   Contribution

The significant contributions of this thesis are listed below.

- The idea of the validation sensor which is the outcome of this work and patented in [1].

- Different design configurations of the contact-based validation sensor and experimental investigations which are published in [2]–[5].

- A novel three-arc methodology to predict the geometry of the opponent-vehicle along with the experimental investigations and comparison with different other contour estimation methods which are described in [7]–[9]

- The geometry-based equations to calculate the dynamic positions of the contact points of the ego-vehicle and opponent-object during the crash as explained in Section 4.4.

- A two-step methodology for generating the data required for the different crash severity and restraint strategy prediction models with a detailed discussion in Section 5.3 and the initial work published in [10], [11]

- A novel modular-based system architecture for predicting crash severity and restraint strategy (please refer to Figure 5.6), along with the different machine learning models to predict vehicle crash responses, the occupant injury criteria, and the restraint strategy (i.e. the class and timing for activation of airbags) investigated in Section 5.5.

References

Self References

[1] G. Sequeira, T. Tyroller, R. Burgmeier, K. Schneider, G. Sequeira, T. Brandmeier, A. Kamann, and R. Lugner, 'Aufprallsensor mit zumindest zwei voneinander beabstandeten Elektroden sowie Verfahren zur Aufprallerkennung sowie Auslösung von Schutzeinrichtungen mit einem solchen Aufprallsensor,' pat. DE 10 2018 200 604 A1, 2018. [Online]. Available: `https://depatisnet.dpma.de/DepatisNet/depatisnet?action=bibdat&docid=DE102018200604A1`.

[2] G. Sequeira, R. Lugner, U. Jumar, and T. Brandmeier, 'A validation sensor based on carbon-fiber-reinforced plastic for early activation of automotive occupant restraint systems,' *Journal of Sensors and Sensor Systems*, vol. 8, no. 1, pp. 19–35, 2019. DOI: `10.5194/jsss-8-19-2019`. [Online]. Available: `https://www.j-sens-sens-syst.net/8/19/2019/`.

[3] G. Sequeira, K. Schneider, R. Lugner, and T. Brandmeier, 'Concepts for validation sensor for pre-crash information from forward-looking sensors,' in *Sensors and Measuring Systems; 19th ITG/GMA-Symposium*, 2018, pp. 1–5, ISBN: 978-3-8007-4683-5.

[4] K. Schneider, G. Sequeira, R. Lugner, A. Kamann, T. Brandmeier, and R. Burgmeier, 'Verification of pre-crash information for a predective activation of passive safety actuators,' in *11. VDI Tagung Fahrzeug-sicherheit*, 2017, pp. 185–196, ISBN: 978-3-1809-2312-3.

[5] G. Sequeira, M. Surve, S. Afraj, and T. Brandmeier, 'A novel concept for validation of pre-crash perception sensor information using contact sensor,' in *2020 IEEE 23rd International Conference on Intelligent Transportation Systems (ITSC)*, 2020, pp. 1–7. DOI: `10.1109/ITSC45102.2020.9294242`.

[6] G. Sequeira, R. Lugner, D. Steinhauser, and T. Brandmeier, 'Investigation of intelligent features for CFRP structure in automotive safety systems,' in *2017 2nd IEEE International Conference on Intelligent Transportation Engineering (ICITE)*, 2017, pp. 18–24. DOI: `10.1109/ICITE.2017.8056874`.

[7]   G. Sequeira, S. Afraj, R. Lugner, and T. Brandmeier, 'Lidar based pre-
diction and contact based validation of crash parameters for a preemptive
restraint strategy,' in *2019 IEEE International Conference on Vehicular
Electronics and Safety (ICVES)*, 2019, pp. 1–7. DOI: `10.1109/ICVES.
2019.8906354`.

[8]   D. M. Mothershed, G. Sequeira, S. Afraj, R. Lugner, K. Schneider, T.
Brandmeier, and V. Soloiu, 'Comparison and evaluation of algorithms for
lidar-based contour estimation in integrated vehicle safety,' *IEEE Transac-
tions on Intelligent Transportation Systems*, pp. 1–18, 2020. DOI: `10.1109/
TITS.2020.3044753`.

[9]   G. Sequeira, S. Afraj, M. Surve, and T. Brandmeier, 'Lidar point cloud
analysis for vehicle contour estimation using polynomial approximation
and curvature breakdown,' in *2020 IEEE 92nd Vehicular Technology Con-
ference (VTC2020-Fall)*, IEEE, 2020, pp. 1–6. DOI: `10.1109/VTC2020-
Fall49728.2020.9348457`.

[10] G. Sequeira and T. Brandmeier, 'Evaluation and characterization of crash-
pulses for head-on collisions with varying overlap crash scenarios,' *Trans-
portation Research Procedia*, vol. 48, pp. 1306–1315, 2020. DOI: `10.1016/
j.trpro.2020.08.156`. [Online]. Available: `http://www.sciencedirect.
com/science/article/pii/S2352146520305731`.

[11] G. Sequeira, A. Patel, S Afraj, R. Lugner, and T. Brandmeier, 'FEM-based
methodology for crash severity estimation in frontal crash scenarios,' *IOP
Conference Series: Materials Science and Engineering*, vol. 831, 2020. DOI:
`10.1088/1757-899x/831/1/012019`.

[12] R. Lugner, M. Inderst, G. Sequeira, K. Schneider, and T. Brandmeier,
'Collision prediction for irreversible pre-crash safety measures,' in *FISITA
2020 World Congress*, 2020.

[13] R. Lugner, D. Vriesman, M. Inderst, G. Sequeira, N. Pasupuleti, A. Zimmer,
and T. Brandmeier, 'Evaluation of sensor tolerances and inevitability for
pre-crash safety systems in real case scenarios,' in *2020 IEEE 3rd Connected
and Automated Vehicles Symposium (CAVS)*, IEEE, 2020, pp. 1–6, ISBN:
978-1-7281-9001-3. DOI: `10.1109/CAVS51000.2020.9334578`.

[14] G. J. Sequeira, B. Harlapur, D. O. Ortegon, R. Lugner, T. Brandmeier,
and V. Soloiu, 'Investigation of influence from variation in color on lidar
sensor for perception of environment in autonomous vehicles,' in *2021 In-
ternational Symposium ELMAR*, IEEE, 2021, pp. 71–76, ISBN: 978-1-6654-
4437-8. DOI: `10.1109/ELMAR52657.2021.9550943`.

[15] G. J. Sequeira, B. Harlapur, R. Lugner, and T. Brandmeier, 'Investigation
of three-arc contour prediction algorithm on kitti lidar raw data set,' in *2021
IEEE 94th Vehicular Technology Conference (VTC2021-Fall)*, IEEE, 2021,

pp. 1–6, ISBN: 978-1-6654-1368-8. DOI: 10.1109/VTC2021-Fall52928.
2021.9625355.

[16] G. J. Sequeira, R. Lugner, T. Brandrneier, E. Elnagdy, G. Danapal, and
      U. Jumar, 'Investigation of different classification algorithms for predict-
      ing occupant injury criterion to decide the required restraint strategy,' in
      *2021 IEEE International Intelligent Transportation Systems Conference
      (ITSC)*, IEEE, 2021, pp. 204–210, ISBN: 978-1-7281-9142-3. DOI: 10.1109/
      ITSC48978.2021.9564868.

[17] G. J. A. Sequeira, A. R. Konda, R. Lugner, U. Jumar, and T. Brandmeier,
      'Crash pulse prediction using regression algorithm with gradient descent op-
      timization method for integrated safety systems,' *SAE International Jour-
      nal of Transportation Safety*, vol. 10, no. 2, 2022, ISSN: 2327-5634. DOI:
      10.4271/09-10-02-0009.

Supervised Master Theses

[18] D. M. Mothershed, 'Quantitative performance assessment of lidar-based
      vehicle contour estimation algorithms for integrated vehicle safety applica-
      tions,' Master thesis, Georgia Southern University, Georgia, U.S.A, 2020.
      [Online]. Available: https://digitalcommons.georgiasouthern.edu/
      etd/2132/.

[19] S. Afraj, 'Lidar based prediction and contact based validation of crash
      scenarios for preemptive restraint strategy,' Master thesis, Technische
      Hochschule Ingolstadt, Ingolstadt, Germany, 2020.

[20] M. Surve, 'Crash-severity prediction under different head-on collision crash
      scenarios,' Master thesis, Univeristy of Siegen, Siegen, Germany, 2020.

Other References

[21] European Union, *Road safety statistics - characteristics at national and
      regional level*, Luxembourg, 2019. [Online]. Available: https://ec.europa.
      eu/eurostat/statistics-explained/index.php?title=Road_safety_
      statistics_-_characteristics_at_national_and_regional_level&
      oldid=450674#General_overview.

[22] Statistisches Bundesamt (Destatis), 'Verkehr: Verkehrsunfälle,' *Fachserie
      8 Reihe 7*, no. 2080700197004, 2020. [Online]. Available: https://www.
      destatis.de/DE/Themen/Gesellschaft-Umwelt/Verkehrsunfaelle/
      Publikationen/Downloads-Verkehrsunfaelle/verkehrsunfaelle-
      jahr-2080700197004.pdf.

[23]   European Commission, *2021 road safety statistics: What is behind the figures?* 9/10/2022. [Online]. Available: `https://transport.ec.europa.eu/2021-road-safety-statistics-what-behind-figures_en`.

[24]   Statistisches Bundesamt (Destatis), 'Verkehr: Verkehrsunfälle,' *Fachserie 8 Reihe 7*, no. 2080700217004, 2022. [Online]. Available: `https://www.destatis.de/DE/Themen/Gesellschaft-Umwelt/Verkehrsunfaelle/Publikationen/Downloads-Verkehrsunfaelle/verkehrsunfaelle-jahr-2080700217004.pdf`.

[25]   Statistisches Bundesamt (Destatis), *Every nine hours someone is killed in a traffic accident due to inappropriate speed in germany*, Wiesbaden, 2020. [Online]. Available: `https://www.destatis.de/EN/Press/2020/07/PE20_N039_46241.html`.

[26]   Deutscher Verkehrssicherheitsrat, 'Vision Zero: Grundlagen & Strategien,' *Schriftenreihe Verkehrssicherheit*, vol. 16, 2012.

[27]   F. Aparicio, J. Paez, F. Moreno, F. Jimenez, and A. Lopez, 'Discussion of a new adaptive speed control system incorporating the geometric characteristics of the roadway,' *International Journal of Vehicle Autonomous Systems*, vol. 3, no. 1, 2005, ISSN: 1471-0226. DOI: `10.1504/IJVAS.2005.007037`.

[28]   J. Richert, D. Coutellier, C. Götz, and W. Eberle, 'Advanced smart airbags: The solution for real-life safety?,' *International Journal of Crashworthiness*, vol. 12, no. 2, pp. 159–171, 2007, ISSN: 1358-8265. DOI: `10.1080/13588260701433461`.

[29]   R. Lugner, K. Schneider, and T. Brandmeier, 'Early activation of passive safety actuators by forward-looking crash parameter estimation,' in *crash.tech 2018*, 2018.

[30]   O. J. Gietelink, D. Verburg, K Labibes, and A. Oostendorp, 'Pre-crash system validation with PRESCAN and VEHIL,' in *2004 IEEE Intelligent Vehicles Symposium*, IEEE, 2004, pp. 913–918.

[31]   C.-Y. Chan, 'A treatise on crash sensing for automotive air bag systems,' *IEEE/ASME Transactions on Mechatronics*, vol. 7, no. 2, pp. 220–234, 2002, ISSN: 1083-4435. DOI: `10.1109/TMECH.2002.1011259`.

[32]   M. Feser, D. McConnell, T. Brandmeier, and C. Lauerer, 'Advanced crash discrimination using Crash Impact Sound Sensing (CISS),' in *SAE Technical Paper Series*, SAE International, Warrendale, PA, 2006. DOI: `10.4271/2006-01-1590`.

[33]   T. Brandmeier, M. Feser, J. Susanne, J. Paggel, S. Saulich, and P. Spannaus, 'Vorrichtung zur Detektion der Charakteristik eines Aufpralls auf ein Kraftfahrzeug,' pat. EP2279100A1, 2008. [Online]. Available: `https://patents.google.com/patent/EP2279100A1/de`.

[34] Infineon Technologies AG, *New applications for integrated pressure sensors: Application note*, Infineon Technologies AG, Ed., 2011. [Online]. Available: `https://www.infineon.com/dgdl/New+Applications+for+Integrated+Pressure+Sensors_Rev1.1.pdf?fileId=db3a3043345a30bc01345fef695e31b3`.

[35] M. Brauer and K. Krupka, 'Advanced pressure sensors with high flexibility for side crash detection,' in *Advanced Microsystems for Automotive Applications 2006*, J. Valldorf and W. Gessner, Eds., Berlin, Heidelberg: Springer Berlin Heidelberg, 2006, pp. 45–51, ISBN: 978-3-540-33410-1.

[36] C.-Y. Chan, 'On the detection of vehicular crashes-system characteristics and architecture,' *IEEE Transactions on Vehicular Technology*, vol. 51, no. 1, pp. 180–193, 2002, ISSN: 00189545. DOI: `10.1109/25.992078`.

[37] F. Garcia, P. Cerri, A. Broggi, J. M. Armingol, and A. de La Escalera, 'Vehicle detection based on laser radar,' in *Computer Aided Systems Theory - EUROCAST 2009*, ser. Lecture Notes in Computer Science, vol. 5717, Berlin, Heidelberg: Springer Berlin Heidelberg, 2009, pp. 391–397, ISBN: 978-3-642-04771-8. DOI: `10.1007/978-3-642-04772-5_51`.

[38] N. Srinivasa, 'Vision-based vehicle detection and tracking method for forward collision warning in automobiles,' in *2002 Intelligent Vehicle Symposium*, IEEE, 2002, pp. 626–631, ISBN: 0-7803-7346-4. DOI: `10.1109/IVS.2002.1188021`.

[39] A. Eidehall and F. Gustafsson, 'Combined road prediction and target tracking in collision avoidance,' in *2004 IEEE Intelligent Vehicles Symposium*, IEEE, 2004, pp. 619–624, ISBN: 0-7803-8310-9. DOI: `10.1109/IVS.2004.1336455`.

[40] A. Eidehall, J. Pohl, and F. Gustafsson, 'Joint road geometry estimation and vehicle tracking,' *Control Engineering Practice*, vol. 15, no. 12, pp. 1484–1494, 2007, ISSN: 09670661. DOI: `10.1016/j.conengprac.2007.02.010`.

[41] E. Coelingh, A. Eidehall, and M. Bengtsson, 'Collision warning with full auto brake and pedestrian detection - a practical example of automatic emergency braking,' in *2010 13th International IEEE Conference on Intelligent Transportation Systems*, Funchal: IEEE, 2010, pp. 155–160, ISBN: 978-1-4244-7657-2. DOI: `10.1109/ITSC.2010.5625077`.

[42] T. Dirndorfer, *Integrale Nutzung von Pre-Crash-Sensorik zur Ansteuerung frontaler Rückhaltesysteme im Fahrzeug – Möglichkeiten und Grenzen*. Göttingen: Cuvillier Verlag, 2015, vol. 110, ISBN: 978-3-7369-9124-8.

[43] Y.-S. Son, H.-K. Sung, and S. W. Heo, 'Automotive frequency modulated continuous wave radar interference reduction using per-vehicle chirp sequences,' *Sensors (Basel, Switzerland)*, vol. 18, no. 9, 2018. DOI: `10.3390/s18092831`.

References

[44]   M. I. Skolnik, *Radar handbook*, 3rd ed. Maidenhead: McGraw-Hill Professional, 2008, ISBN: 9780071485470. [Online]. Available: http://www.loc.gov/catdir/enhancements/fy0808/2007052691-d.html.

[45]   H. Winner, S. Hakuli, F. Lotz, and C. T. Singer, Eds., *Handbook of driver assistance systems: Basic information, components and systems for active safety and comfort.* Cham: Springer Reference, 2016, ISBN: 978-3-319-12352-3.

[46]   V. Issakov, *Microwave Circuits for 24 GHz Automotive Radar in Silicon-based Technologies*, Online-ausg. Berlin, Heidelberg: Springer-Verlag Berlin Heidelberg, 2010, ISBN: 978-3-642-13597-2.

[47]   F. de Ponte Müller, 'Survey on ranging sensors and cooperative techniques for relative positioning of vehicles,' *Sensors (Basel, Switzerland)*, vol. 17, no. 2, 2017. DOI: 10.3390/s17020271.

[48]   A. Kamann, P. Held, F. Perras, P. Zaumseil, T. Brandmeier, and U. T. Schwarz, 'Automotive radar multipath propagation in uncertain environments,' in *2018 21st International Conference on Intelligent Transportation Systems (ITSC)*, 2018, pp. 859–864. DOI: 10.1109/ITSC.2018.8570016.

[49]   W. Buller, B. Wilson, J. Garbarino, J. Kelly, N. Subotic, B. Thelen, and B. Belzowski, *Radar congestion study*, Washington, DC. [Online]. Available: www.nhtsa.gov/sites/nhtsa.dot.gov/files/documents/13790_radarstudy_092518_v2b-tag.pdf.

[50]   S. Haag, B. Duraisamy, H.-L. Blocher, J. Dickmann, M. Fritzsche, and W. Koch, 'Effects of radar interference on target tracking and sensor fusion on automotive applications,' in *2019 20th International Radar Symposium (IRS)*, IEEE, 2019, pp. 1–10, ISBN: 978-3-7369-9860-5. DOI: 10.23919/IRS.2019.8768093.

[51]   Velodyna Lidar Inc., *HDL-64E - data sheet.* [Online]. Available: https://velodynelidar.com/products/hdl-64e/.

[52]   D. Wang, C. Watkins, and H. Xie, 'MEMS mirrors for lidar: A review,' *Micromachines*, vol. 11, no. 5, 2020, ISSN: 2072-666X. DOI: 10.3390/mi11050456.

[53]   S. Chung, H. Abediasl, and H. Hashemi, '15.4 A 1024-element scalable optical phased array in 0.18µm SOI CMOS,' in *2017 IEEE International Solid-State Circuits Conference (ISSCC)*, IEEE, 2017, pp. 262–263, ISBN: 978-1-5090-3758-2. DOI: 10.1109/ISSCC.2017.7870361.

[54]   S. Hasirlioglu and A. Riener, 'Challenges in object detection under rainy weather conditions,' in *Intelligent Transport Systems, From Research and Development to the Market Uptake*, ser. Lecture Notes of the Institute for Computer Sciences, Social Informatics and Telecommunications Engineering, vol. 267, Cham: Springer International Publishing, 2019, pp. 53–65, ISBN: 978-3-030-14756-3. DOI: 10.1007/978-3-030-14757-0_5.

[55] S. Hasirlioglu and A. Riener, 'Introduction to rain and fog attenuation on automotive surround sensors,' in *2017 IEEE 20th International Conference on Intelligent Transportation Systems (ITSC)*, IEEE, 2017, pp. 1–7, ISBN: 978-1-5386-1526-3. DOI: 10.1109/ITSC.2017.8317823.

[56] F. Engels, P. Heidenreich, M. Wintermantel, L. Stacker, M. Al Kadi, and A. M. Zoubir, 'Automotive radars signal processing: Research directions and practical challenges,' *IEEE Journal of Selected Topics in Signal Processing*, pp. 865–878, 2021, ISSN: 1932-4553. DOI: 10.1109/JSTSP.2021.3063666.

[57] Bosch Mobility Solutions, *Long-range radar sensor (LRR) - data sheet.* [Online]. Available: https://www.bosch-mobility-solutions.com/en/products-and-services/passenger-cars-and-light-commercial-vehicles/driver-assistance-systems/left-turn-assist/long-range-radar-sensor/.

[58] Bosch Mobility Solutions, *Mid-range radar sensor (MRR) - data sheet.* [Online]. Available: https://www.bosch-mobility-solutions.com/media/global/products-and-services/passenger-cars-and-light-commercial-vehicles/driver-assistance-systems/predictive-emergency-braking-system/mid-range-radar-sensor-(mrr)/product-data-sheet-mid-range-radar-sensor-(mrr)-2.pdf.

[59] Continental Engineering Services, *ARS 408-21 long range radar sensor 77 GHz - data sheet.* [Online]. Available: https://www.conti-engineering.com/getattachment/ef591d58-93f5-4004-a46b-512996d5c8f7/ARS-408-21_EN_HS.pdf.

[60] Continental Engineering Services, *SRR 308-21 short range radar sensor 24 GHz - data sheet.* [Online]. Available: https://www.conti-engineering.com/getattachment/98380e1a-3789-4518-b0f6-dffe87229520/SRR308-21_EN_HS.pdf.

[61] Hexagon Autonomy and Positioning, *Electronically scanning radar - data sheet.* [Online]. Available: https://autonomoustuff.com/wp-content/uploads/2019/05/delphi-esr-whitelabel.pdf.

[62] Hexagon Autonomy and Positioning, *Delphi MRR - data sheet.* [Online]. Available: https://autonomoustuff.com/wp-content/uploads/2019/05/delphi_mrr_datasheet_052119.pdf.

[63] Hexagon Autonomy and Positioning, *Lux family - data sheet.* [Online]. Available: https://autonomoustuff.com/wp-content/uploads/2019/05/ibeo_LUX_datasheet_whitelabel.pdf.

[64] Robosense (Suteng Innovation Technology Co., Ltd.), *RS-LiDAR-M1 - data sheet.* [Online]. Available: https://www.robosense.ai/rslidar/rs-lidar-M1.

[65]   Robosense (Suteng Innovation Technology Co., Ltd.), *RS-Ruby - data sheet.* [Online]. Available: `https://www.robosense.ai/rslidar/rs-ruby`.

[66]   A.D.C. GmbH, *SRL 1 + SRL 1C - data sheet.* [Online]. Available: `https://www.continental-automotive.com/getattachment/3918b2f6-8c47-421c-80b6-8773734931f3/SRL1-SRL1C-Datasheet-EN.pdf`.

[67]   M. Ding, Z. Zhang, X. Jiang, and Y. Cao, 'Vision-based distance measurement in Advanced Driving Assistance Systems,' *Applied Sciences*, vol. 10, no. 20, pp. 1–19, 2020. DOI: `10.3390/app10207276`.

[68]   T. Kowsari, S. S. Beauchemin, and J. Cho, 'Real-time vehicle detection and tracking using stereo vision and multi-view AdaBoost,' in *2011 14th International IEEE Conference on Intelligent Transportation Systems (ITSC)*, IEEE, 2011, pp. 1255–1260, ISBN: 978-1-4577-2197-7. DOI: `10.1109/ITSC.2011.6082972`.

[69]   Bosch Mobility Solutions, *Stereo video camera - data sheet.* [Online]. Available: `https://www.bosch-mobility-solutions.com/en/products-and-services/passenger-cars-and-light-commercial-vehicles/driver-assistance-systems/lane-departure-warning/stereo-video-camera/`.

[70]   Bosch Mobility Solutions, *Multi purpose camera - data sheet.* [Online]. Available: `https://www.bosch-mobility-solutions.com/en/products-and-services/passenger-cars-and-light-commercial-vehicles/driver-assistance-systems/lane-departure-warning/multi-purpose-camera/`.

[71]   Continental Engineering Services, *Multi function camera with lidar - data sheet.* [Online]. Available: `https://www.continental-automotive.com/en-gl/Passenger-Cars/Autonomous-Mobility/Enablers/Cameras/Multi-Function-Camera-with-Lidar`.

[72]   M. Kronauge and H. Rohling, 'New chirp sequence radar waveform,' *IEEE Transactions on Aerospace and Electronic Systems*, vol. 50, no. 4, pp. 2870–2877, 2014, ISSN: 0018-9251. DOI: `10.1109/TAES.2014.120813`.

[73]   H. Rohling and M.-M. Meinecke, 'Waveform design principles for automotive radar systems,' in *2001 CIE International Conference on Radar Proceedings (Cat No.01TH8559)*, IEEE, 2001, pp. 1–4, ISBN: 0-7803-7000-7. DOI: `10.1109/ICR.2001.984612`.

[74]   T. Fersch, R. Weigel, and A. Koelpin, 'A CDMA modulation technique for automotive time-of-flight lidar systems,' *IEEE Sensors Journal*, vol. 17, no. 11, pp. 3507–3516, 2017. DOI: `10.1109/JSEN.2017.2688126`.

[75] P. Held, D. Steinhauser, A. Kamann, T. Holdgrun, I. Doric, A. Koch, and T. Brandmeier, 'Radar-based analysis of pedestrian micro-doppler signatures using motion capture sensors,' in *2018 IEEE Intelligent Vehicles Symposium*, IEEE, 2018, pp. 787–793, ISBN: 978-1-5386-4452-2. DOI: 10.1109/IVS.2018.8500656.

[76] D. Kellner, M. Barjenbruch, J. Klappstein, J. Dickmann, and K. Dietmayer, 'Wheel extraction based on micro doppler distribution using high-resolution radar,' in *2015 IEEE MTT-S International Conference on Microwaves for Intelligent Mobility (ICMIM)*, IEEE, 2015, pp. 1–4, ISBN: 978-1-4799-7215-9. DOI: 10.1109/ICMIM.2015.7117951.

[77] S. Hasirlioglu, A. Kamann, I. Doric, and T. Brandmeier, 'Test methodology for rain influence on automotive surround sensors,' in *2016 IEEE 19th International Conference on Intelligent Transportation Systems (ITSC)*, 2016, pp. 2242–2247. DOI: 10.1109/ITSC.2016.7795918.

[78] A. Kamann, S. Hasirlioglu, I. Doric, T. Speth, T. Brandmeier, and U. T. Schwarz, 'Test methodology for automotive surround sensors in dynamic driving situations,' in *2017 IEEE 85th Vehicular Technology Conference (VTC Spring)*, IEEE, 2017, pp. 1–6, ISBN: 978-1-5090-5932-4. DOI: 10.1109/VTCSpring.2017.8108194.

[79] J. Canny, *The complexity of robot motion planning*. 1988, ISBN: 9780262031363.

[80] J. T. Schwartz and C. K. Yap, *Advances in robotics: Algorithmic and geometric aspects of robotics*. Philadelphia, 1986, vol. 1.

[81] J.-C. Latombe, *Robot Motion Planning*. Boston: Springer International Publishing, 1991, ISBN: 978-1-4615-4022-9. DOI: 10.1007/978-1-4615-4022-9.

[82] O. Khatib, 'Real-time obstacle avoidance for manipulators and mobile robots,' in *Proceedings. 1985 IEEE International Conference on Robotics and Automation*, vol. 2, 1985, pp. 500–505. DOI: 10.1109/ROBOT.1985.1087247.

[83] J. Borenstein and Y. Koren, 'Real-time obstacle avoidance for fast mobile robots,' *IEEE Transactions on Systems, Man, and Cybernetics*, vol. 19, no. 5, pp. 1179–1187, 1989. DOI: 10.1109/21.44033.

[84] I. Ulrich and J. Borenstein, 'VFH+: Reliable obstacle avoidance for fast mobile robots,' in *Proceedings. 1998 IEEE International Conference on Robotics and Automation (Cat. No.98CH36146)*, vol. 2, 1998, pp. 1572–1577. DOI: 10.1109/ROBOT.1998.677362.

[85] H. Kaluđer, M. Brezak, and I. Petrović, 'A visibility graph based method for path planning in dynamic environments,' in *2011 Proceedings of the 34th International Convention MIPRO*, 2011, pp. 717–721.

References

[86] H. Choset and J. Burdick, 'Sensor-based exploration: The hierarchical generalized voronoi graph,' *The International Journal of Robotics Research*, vol. 19, no. 2, pp. 96–125, 2000, ISSN: 0278-3649. DOI: 10.1177/02783640022066770.

[87] K. Nagatani, Y. Iwai, and Y. Tanaka, 'Sensor based navigation for car-like mobile robots using generalized voronoi graph,' in *Proceedings 2001 IEEE/RSJ International Conference on Intelligent Robots and Systems. Expanding the Societal Role of Robotics in the the Next Millennium (Cat. No.01CH37180)*, vol. 2, 2001, pp. 1017–1022. DOI: 10.1109/IROS.2001.976302.

[88] J. Lee and B. Litkouhi, 'A unified framework of the automated lane centering/changing control for motion smoothness adaptation,' in *2012 15th International IEEE Conference on Intelligent Transportation Systems*, 2012, pp. 282–287. DOI: 10.1109/ITSC.2012.6338738.

[89] L. Han, H. Yashiro, H. Tehrani Nik Nejad, Q. H. Do, and S. Mita, 'Bézier curve based path planning for autonomous vehicle in urban environment,' in *2010 IEEE Intelligent Vehicles Symposium*, 2010, pp. 1036–1042. DOI: 10.1109/IVS.2010.5548085.

[90] T. Berglund, A. Brodnik, H. Jonsson, M. Staffanson, and I. Soderkvist, 'Planning smooth and obstacle-avoiding b-spline paths for autonomous mining vehicles,' *IEEE Transactions on Automation Science and Engineering*, vol. 7, no. 1, pp. 167–172, 2010. DOI: 10.1109/TASE.2009.2015886.

[91] M. F. Hsieh and U. Ozguner, 'A parking algorithm for an autonomous vehicle,' in *2008 IEEE Intelligent Vehicles Symposium*, 2008, pp. 1155–1160. DOI: 10.1109/IVS.2008.4621317.

[92] M. Werling, J. Ziegler, S. Kammel, and S. Thrun, 'Optimal trajectory generation for dynamic street scenarios in a frenét frame,' in *2010 IEEE International Conference on Robotics and Automation*, 2010, pp. 987–993. DOI: 10.1109/ROBOT.2010.5509799.

[93] B. Paden, M. Čáp, S. Z. Yong, D. Yershov, and E. Frazzoli, 'A survey of motion planning and control techniques for self-driving urban vehicles,' *IEEE Transactions on Intelligent Vehicles*, vol. 1, no. 1, pp. 33–55, 2016. DOI: 10.1109/TIV.2016.2578706.

[94] H. Winner, S. Hakuli, F. Lotz, and C. Singer, *Handbuch Fahrerassistenzsysteme.* Wiesbaden: Springer Fachmedien Wiesbaden, 2015, ISBN: 978-3-658-05733-6. DOI: 10.1007/978-3-658-05734-3.

[95] D. Schramm, M. Hiller, and R. Bardini, *Modellbildung und Simulation der Dynamik von Kraftfahrzeugen.* Berlin, Heidelberg: Springer Berlin Heidelberg, 2010, ISBN: 978-3-540-89313-4. DOI: 10.1007/978-3-540-89315-8.

[96] J. Schlichenmaier, F. Roos, M. Kunert, and C. Waldschmidt, 'Adaptive clustering for contour estimation of vehicles for high-resolution radar,' in *2016 IEEE MTT-S International Conference on Microwaves for Intelligent Mobility (ICMIM)*, IEEE, 2016, pp. 1–4, ISBN: 978-1-5090-2367-7. DOI: `10.1109/ICMIM.2016.7533930`.

[97] P. Berthold, M. Michaelis, T. Luettel, D. Meissner, and H.-J. Wuensche, 'Radar reflection characteristics of vehicles for contour and feature estimation,' in *2017 Sensor Data Fusion: Trends, Solutions, Applications (SDF)*, IEEE, 2017, pp. 1–6, ISBN: 978-1-5386-3103-4. DOI: `10.1109/SDF.2017.8126352`.

[98] F. Roos, D. Kellner, J. Dickmann, and C. Waldschmidt, 'Reliable orientation estimation of vehicles in high-resolution radar images,' *IEEE Transactions on Microwave Theory and Techniques*, vol. 64, no. 9, pp. 2986–2993, 2016, ISSN: 0018-9480. DOI: `10.1109/TMTT.2016.2586476`.

[99] T. Johansson and O. Wellenstam, 'Lidar clustering and shape extraction for automotive applications,' Master thesis, Chalmers University of Technology, Sweden, 2017.

[100] J. Schlichenmaier, N. Selvaraj, M. Stolz, and C. Waldschmidt, 'Template matching for radar-based orientation and position estimation in automotive scenarios,' in *2017 IEEE MTT-S International Conference on Microwaves for Intelligent Mobility (ICMIM)*, IEEE, 2017, pp. 95–98, ISBN: 978-1-5090-4354-5. DOI: `10.1109/ICMIM.2017.7918865`.

[101] M. Schütz, N. Appenrodt, J. Dickmann, and K. Dietmayer, 'Simultaneous tracking and shape estimation with laser scanners,' in *Proceedings of the 16th International Conference on Information Fusion*, 2013, pp. 885–891.

[102] K. Schneider, R. Lugner, and T. Brandmeier, 'Lidar-based contour estimation of oncoming vehicles in pre-crash scenarios,' in *2019 IEEE Intelligent Vehicles Symposium*, IEEE, 2019, pp. 2272–2277, ISBN: 978-1-7281-0560-4. DOI: `10.1109/IVS.2019.8813825`.

[103] K. Liu and J. Wang, 'Fast dynamic vehicle detection in road scenarios based on pose estimation with convex-hull model,' *Sensors (Basel, Switzerland)*, vol. 19, no. 14, 2019. DOI: `10.3390/s19143136`.

[104] M. Huang, *Vehicle Crash Mechanics*. CRC Press, 2002, ISBN: 9781420041866. [Online]. Available: `https://books.google.de/books?id=QYHLBQAAQBAJ`.

[105] W. Pawlus, K. G. Robbersmyr, and H. R. Karimi, 'Mathematical modeling and parameters estimation of a car crash using data-based regressive model approach,' *Applied Mathematical Modelling*, vol. 35, no. 10, pp. 5091–5107, 2011, ISSN: 0307904X. DOI: `10.1016/j.apm.2011.04.024`.

[106] D. Bohmlander, V. Yano, T. Brandmeier, A. Zimmer, L. L. Ling, C.-B. Wong, and T. Dirndorfer, 'A novel approach for intelligent pre-crash threat assessment systems,' in *17th International IEEE Conference on Intelligent Transportation Systems (ITSC)*, IEEE, 2014, pp. 954–961, ISBN: 978-1-4799-6078-1. DOI: 10.1109/ITSC.2014.6957812.

[107] Jaemoon Lim, 'A consideration on the offset frontal impact modeling using spring-mass model,' *International Journal of Mechanical and Mechatronics Engineering*, vol. 9, no. 8, pp. 1453–1458, 2015. DOI: 10.5281/zenodo.1107341.

[108] A. Das, M. Abdel-Aty, and A. Pande, 'Using conditional inference forests to identify the factors affecting crash severity on arterial corridors,' *Journal of safety research*, vol. 40, no. 4, pp. 317–327, 2009. DOI: 10.1016/j.jsr.2009.05.003.

[109] F. Rezaie Moghaddam, S. Afandizadeh, and M. Ziyadi, 'Prediction of accident severity using artificial neural networks,' *International Journal of Civil Engineering*, vol. 9, no. 1, 2011. [Online]. Available: http://ijce.iust.ac.ir/article-1-544-en.html.

[110] S. Alkheder, M. Taamneh, and S. Taamneh, 'Severity prediction of traffic accident using an artificial neural network,' *Journal of Forecasting*, vol. 36, no. 1, pp. 100–108, 2017, ISSN: 02776693. DOI: 10.1002/for.2425.

[111] M. M. Chong, A. Abraham, and M. Paprzycki, 'Traffic accident analysis using machine learning paradigms,' *Informatica (Slovenia)*, vol. 29, pp. 89–98, 2005.

[112] D. W. Kononen, C. A. C. Flannagan, and S. C. Wang, 'Identification and validation of a logistic regression model for predicting serious injuries associated with motor vehicle crashes,' *Accident; analysis and prevention*, vol. 43, no. 1, pp. 112–122, 2011, ISSN: 0001-4575. DOI: 10.1016/j.aap.2010.07.018.

[113] A. Pakgohar, R. S. Tabrizi, M. Khalili, and A. Esmaeili, 'The role of human factor in incidence and severity of road crashes based on the cart and lr regression: A data mining approach,' *Procedia Computer Science*, vol. 3, pp. 764–769, 2011, ISSN: 18770509. DOI: 10.1016/j.procs.2010.12.126.

[114] D. Vriesman, B. Thoresz, D. Steinhauser, A. Zimmer, A. Britto, and T. Brandmeier, 'An experimental analysis of rain interference on detection and ranging sensors,' in *2020 IEEE 23rd International Conference on Intelligent Transportation Systems (ITSC)*, IEEE, 2020, pp. 1–5, ISBN: 978-1-7281-4149-7. DOI: 10.1109/ITSC45102.2020.9294505.

[115] ISO, 'Road vehicles - Functional safety - Part 9: Automotive Safety Integrity Level (ASIL)-oriented and safety-oriented,' International Organization for Standardization, Geneva, CH, Standard ISO 26262, 2011.

[116] P. P. L. Regtien, *Sensors for mechatronics*, 1st ed., ser. Elsevier insights. Amsterdam and New York: Elsevier, 2012, ISBN: 978-0-12-391497-2.

[117] J. F. Vetelino and A. Reghu, *Introduction to sensors*. Boca Raton [Floride]: CRC Press, 2011, ISBN: 978-1-4398-0852-8.

[118] J. Fraden, *Handbook of modern sensors: Physics, designs, and applications*, 3rd ed. New York: Springer, 2003, ISBN: 0-387-00750-4.

[119] R. Frodl and D. Schoedlbauer, 'Modern concepts for low cost, high performance position sensors,' in *SAE Technical Paper Series*, ser. SAE Technical Paper Series, SAE International400 Commonwealth Drive, Warrendale, PA, United States, 1998. DOI: 10.4271/980172.

[120] X. Li and G. Meijer, 'A novel smart resistive-capacitive position sensor,' *IEEE Transactions on Instrumentation and Measurement*, vol. 44, no. 3, pp. 768–770, 1995, ISSN: 00189456. DOI: 10.1109/19.387328.

[121] J. Wen, Z. Xia, and F. Choy, 'Damage detection of carbon fiber reinforced polymer composites via electrical resistance measurement,' *Composites Part B: Engineering*, vol. 42, no. 1, pp. 77–86, 2011, ISSN: 13598368. DOI: 10.1016/j.compositesb.2010.08.005.

[122] N. Angelidis and P. E. Irving, 'Detection of impact damage in CFRP laminates by means of electrical potential techniques,' *Composites Science and Technology*, vol. 67, no. 3-4, pp. 594–604, 2007, ISSN: 02663538. DOI: 10.1016/j.compscitech.2006.07.033.

[123] M.-Y. Cheng, X.-H. Huang, C.-W. Ma, and Y.-J. Yang, 'A flexible capacitive tactile sensing array with floating electrodes,' *Journal of Micromechanics and Microengineering*, vol. 19, no. 11, 2009, ISSN: 0960-1317. DOI: 10.1088/0960-1317/19/11/115001.

[124] M. Pufke, F. Hilbrunner, C. Diethold, and T. Fröhlich, 'Capacitive sensor technology based on area variation for precise position detection,' in *58th Ilmenau Scientific Colloqium*, 2014. [Online]. Available: http://nbn-resolving.de/urn:nbn:de:gbv:ilm1-2014iwk-161:9.

[125] S. Taghvaeeyan and R. Rajamani, 'Magnetic sensor-based large distance position estimation with disturbance compensation,' *IEEE Sensors Journal*, vol. 15, no. 8, pp. 4249–4258, 2015. DOI: 10.1109/JSEN.2015.2413936.

[126] A. Babu and B. George, 'Design and development of a new non-contact inductive displacement sensor,' *IEEE Sensors Journal*, vol. 18, no. 3, pp. 976–984, 2018. DOI: 10.1109/JSEN.2017.2780835.

[127] M. S. Kim, S. E. Jo, D. H. Kang, H. R. Ahn, and Y. J. Kim, 'A dome shaped piezoelectric tactile sensor array using controlled inflation technique,' in *2013 Transducers & Eurosensors XXVII: The 17th International Conference on Solid-State Sensors, Actuators and Microsystems*, IEEE, 2013, pp. 1891–1894, ISBN: 978-1-4673-5983-2. DOI: 10.1109/Transducers.2013.6627161.

[128] M. Krause, U. Helbig, M. Zirkl, A. Sawatdee, P. Bodo, G. Domann, B. Stadlober, A. Boulbitch, and S. Bauer, 'Large area piezoelectric impact sensors,' in *2012 Annual Report Conference on Electrical Insulation and Dielectric Phenomena*, IEEE, 2012, pp. 681–683, ISBN: 978-1-4673-1252-3. DOI: `10.1109/CEIDP.2012.6378872`.

[129] F.-R. Fan, Z.-Q. Tian, and Z. Lin Wang, 'Flexible triboelectric generator,' *Nano Energy*, vol. 1, no. 2, pp. 328–334, 2012, ISSN: 22112855. DOI: `10.1016/j.nanoen.2012.01.004`.

[130] C. Wu, A. C. Wang, W. Ding, H. Guo, and Z. L. Wang, 'Triboelectric nanogenerator: A foundation of the energy for the new era,' *Advanced Energy Materials*, vol. 9, no. 1, pp. 1–25, 2019, ISSN: 16146832. DOI: `10.1002/aenm.201802906`.

[131] X. Ding, H. Cao, X. Zhang, M. Li, and Y. Liu, 'Large scale triboelectric nanogenerator and self-powered flexible sensor for human sleep monitoring,' *Sensors (Basel, Switzerland)*, vol. 18, no. 6, 2018. DOI: `10.3390/s18061713`.

[132] C.-M. Chiu, S.-W. Chen, Y.-P. Pao, M.-Z. Huang, S.-W. Chan, and Z.-H. Lin, 'A smart glove with integrated triboelectric nanogenerator for self-powered gesture recognition and language expression,' *Science and technology of advanced materials*, vol. 20, no. 1, pp. 964–971, 2019, ISSN: 1468-6996. DOI: `10.1080/14686996.2019.1665458`.

[133] M. S. Rasel, H. O. Cho, J. W. Kim, and J. Y. Park, 'A self-powered triboelectric sensor for wide-range pressure detection in wearable application,' *Journal of Physics: Conference Series*, vol. 1052, 2018, ISSN: 0964-1726. DOI: `10.1088/1742-6596/1052/1/012029`.

[134] ISO, 'Road vehicles - Vechile dynamics and road-holding ability - Vocabulary,' International Organization for Standardization, Geneva, CH, Standard, 2011.

[135] Euro NCAP, *Technical bulletin: Data format and injury criteria calculation*, 2017. [Online]. Available: `https://cdn.euroncap.com/media/32293/tb-021-data-acquisition-and-injury-calculation-v21.pdf`.

[136] K. A. Solomon, W.-K. Chao, and J. Kendall, *Defining the Criteria for Air Bag Activation in Passenger Vehicles*, 1. Aufl. Saarbrücken: LAP LAMBERT Academic Publishing, 2015, ISBN: 978-3659697982.

[137] European Commission, *Council directive 96/53/EC*, European Commission, Ed., 1996. [Online]. Available: `https://eur-lex.europa.eu/legal-content/EN/TXT/PDF/?uri=CELEX:31996L0053&from=EN`.

[138] The Mathworks, Inc., *pcfitplane: Fit plane to 3-D point cloud*, The Mathworks, Inc., Ed., 2015. [Online]. Available: `https://de.mathworks.com/help/vision/ref/pcfitplane.html`.

[139] The Mathworks Inc., *pcsegdist: Segment point cloud into clusters based on Euclidean distance*, The Mathworks, Inc., Ed., 2018. [Online]. Available: `https://www.mathworks.com/help/vision/ref/pcsegdist.html?s_tid=srchtitle`.

[140] S.-W. Hong, C.-K. Park, P. Mohan, R. M. Morgan, C.-D. Kan, K. Lee, S. Park, and H. Bae, 'A study of the IIHS frontal pole impact test,' in *SAE Technical Paper Series*, ser. SAE Technical Paper Series, SAE International 400 Commonwealth Drive, Warrendale, PA, United States, 2008. DOI: `10.4271/2008-01-0507`.

[141] Federal Ministry of food and agriculture, Germany, *The forests in germany*, 2015. [Online]. Available: `https://www.bmel.de/SharedDocs/Downloads/EN/Publications/ForestsInGermany-BWI.pdf?__blob=publicationFile`.

[142] Insurance Institute for Highway Safety, *Fatality facts*. [Online]. Available: `https://www.iihs.org/topics/fatality-statistics/detail/passenger-vehicle-occupants#crash-types`.

[143] C. J. Kahane, 'Comparison of 2013 VMT fatality rates in U.S. states and in high-income countries,' National Highway Traffic Safety Administration, Tech. Rep. DOT HS 812 340, 2016. [Online]. Available: `https://crashstats.nhtsa.dot.gov/Api/Public/Publication/812340`.

[144] C. J. Kahane, 'Effectiveness of pretensioners and load limiters for enhancing fatality reduction by seat belts,' National Highway Traffic Safety Administration, Tech. Rep. DOT HS 811 835, 2013. [Online]. Available: `https://crashstats.nhtsa.dot.gov/Api/Public/ViewPublication/811835`.

[145] Euro NCAP, *Data format and injury criteria calculation*, 2017. [Online]. Available: `https://cdn.euroncap.com/media/32293/tb-021-data-acquisition-and-injury-calculation-v21.pdf`.

[146] Global NCAP, *Assesment protocol - adult occupant protection*, 2017. [Online]. Available: `http://www.globalncap.org/wp-content/uploads/2018/03/assessment-protocol-Adult.pdf`.

[147] Euro NCAP, *Assesment protocol - adult occupant protection*, 2019. [Online]. Available: `https://cdn.euroncap.com/media/43372/euro-ncap-assessment-protocol-aop-v901.pdf`.

[148] S. Smit, E. Tomasch, H. Kolk, M. A. Plank, J. Gugler, and H. Glaser, 'Evaluation of a momentum based impact model in frontal car collisions for the prospective assessment of ADAS,' *European Transport Research Review*, vol. 11, no. 1, 2019, ISSN: 1867-0717. DOI: `10.1186/s12544-018-0343-3`.

[149] Center For Collision Safety And Analysis, *2010 toyota yaris finite element model validation coarse mesh*, 2016. DOI: `10.13021/G8JS5D`.

[150] B. D. Grenke, 'Digital filtering for J211 requirements using a fast fourier transform based filter,' in *SAE Technical Paper Series*, ser. SAE Technical Paper Series, SAE International 400 Commonwealth Drive, Warrendale, PA, United States, 2002. DOI: 10.4271/2002-01-0796.

[151] Livermore Software Technology (LST), an Ansys company, *LS-Dyna keyword user's manual: Volume I*, 2020. [Online]. Available: https://www.dynasupport.com/manuals/ls-dyna-manuals/ls-dyna_manual_volume_i_r12.pdf/@@download/file/LS-DYNA_Manual_Volume_I_R12.pdf.

[152] B. J. Smyth and J. W. Smith, 'Developing a sled test from crash test data,' in *SAE Technical Paper Series*, ser. SAE Technical Paper Series, SAE International 400 Commonwealth Drive, Warrendale, PA, United States, 2007. DOI: 10.4271/2007-01-0711.

[153] F. Lee, C. H. McCleery, C. Ngo, M. Limousis-Gayda, and R. Hashish, 'Probability of frontal airbag deployment in bumper-bumper and underride collisions,' in *SAE Technical Paper Series*, ser. SAE Technical Paper Series, SAE International 400 Commonwealth Drive, Warrendale, PA, United States, 2019. DOI: 10.4271/2019-01-0620.

[154] D. Gabauer and H. C. Gabler, 'Evaluation of threshold values of acceleration severity index by using event data recorder technology,' *Transportation Research Record: Journal of the Transportation Research Board*, vol. 1904, no. 1, pp. 37–45, 2005, ISSN: 0361-1981. DOI: 10.1177/0361198105190400104.

[155] H. C. Gabler and J. Hinch, 'Evaluation of advanced air bag deployment algorithm performance using event data recorders,' *Annals of Advances in Automotive Medicine / Annual Scientific Conference*, vol. 52, pp. 175–184, 2008, ISSN: 1943-2461.

[156] C. Haasper, M. Junge, A. Ernstberger, H. Brehme, L. Hannawald, C. Langer, J. Nehmzow, D. Otte, U. Sander, C. Krettek, and H. Zwipp, 'Die Abbreviated Injury Scale (AIS). Potenzial und Probleme bei der Anwendung,' *Der Unfallchirurg*, vol. 113, no. 5, pp. 366–372, 2010. DOI: 10.1007/s00113-010-1778-8.

[157] J. Saunders, M. Craig, and J. Suway, 'NHTSA's test procedure evaluations for small overlap/oblique crashes,' in *22nd ESV Conference*, 2011. [Online]. Available: https://www-esv.nhtsa.dot.gov/Proceedings/22/files/22ESV-000343.pdf.

[158] R. Reichert, P. Chung-Kyu, and R. Morgan, 'Development of integrated vehicle-occupant model for crashworthiness safety analysis,' National Highway Traffic Safety Administration, Washington DC, USA, Tech. Rep. DOT HS 812 087, 2014.

[159] ABAQUS, Inc., *Side curtain airbag impactor test*, 2006. [Online]. Available: https://classes.engineering.wustl.edu/2009/spring/mase5513/ abaqus/docs/v6.6/books/exa/default.htm?startat=ch03s03aex91. html.

Appendices

A Characteristics of forward-looking sensors

Table A.1: Characteristics of automotive radar sensors [57]–[62].

Sensor (Manufacturer)	Range w.r.t azimuth angle antenna, angle [°], range [m]	Accuracy longitudinal distance [m], relative velocity [m/s], angle [°]	Cycle [ms]
LRR4 (Bosch)	main, ±6, 200 main, ±10, 100 main, ±15, 30 main, ±20, 5 elevation, ±4.5, 200	±0.12, 0.11, ±0.1 - ±0.3	60
MRR (Bosch)	main, ±6, 160 main, ±9, 100 main, ±10, 60 elevation, ±25, 36 elevation, ±42, 12	0.12, 0.11, ±0.3	60
ASR408-21 (Continental)	main, ±9, 250 main, ±45, 100 main, ±60, 20 elevation, 14, 250 elevation, 20, 100	±0.1 - ±0.4, ±0.027, ±0.1 - ±5	72
SRR308-21 (Continental)	main, ±75, 95 elevation, 12 - 23, -	±0.2 - ±0.5, ±0.054, ±2 - ±5	40
ESR 2.5 (Delphi)	main, ±10, 174 main, ±45, 60	1.8, 0.12, -	50
MRR (Delphi)	main, 90, 160 elevation, 5, -	±0.5 (with 3% bias), ±0.3, ±1	30

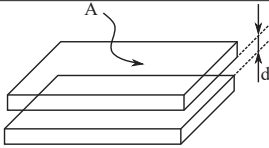Table A.2: Characteristics of automotive lidar sensors [51], [63]–[66]

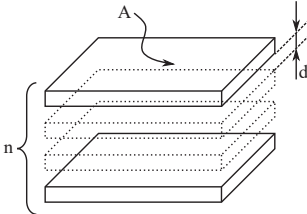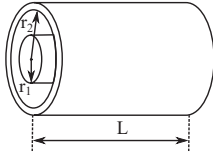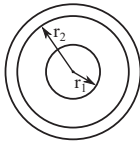| Sensor (Manufacturer)	Range [m] max. (accuracy)	Field of view [°]		Cycle [ms]
		Azimuth max. (res.)	Vertical max. (res.)	
HDL-64E S3 (Velodyne)	120 (0.02)	360 (0.35)	26.9 (0.4)	50.0
LUX 8L (Ibeo automotive)	50 (0.1)	110 (0.25)	6.4 (0.8)	40.0
RS-LiDAR-M1 (Robosense)	150 (0.05)	120 (0.2)	25 (0.2)	66.6
RS-Ruby (Robosense)	250 (0.03)	360 (0.4)	40 (0.1)	50.0
SRL 1C (Continental)	13.5 (0.005)	27 (-)	11 (-)	10.0

Table A.3: Characteristics of automotive camera sensors [69]–[71]

Sensor (Manufacturer)	Imager resolution	Range [m]	Field of view [°]		Frame rate [fps]
			Horizontal	Vertical	
Stereo video camera (Bosch)	1280 × 960	55	50	28	30
Multipurpose camera (Bosch)	2408 × 1280	150	100	48	45
Multi function camera (Continental)	840 × 630	10	40	29	20

B Geometric factors for capacitors

Table B.1: Geometric factors for different types of the capacitor (A is the area of the plates, d is the distance between the plates, n is the number of plates, L is the length of the cylinders, and r_1 and r_2 are inner and outer radii of either cylinder or sphere).

Type	Equation for G	Pictorial representation
Parallel-plate capacitor	$\dfrac{A}{d}$	
Multi-plate capacitor	$(n-1) \cdot \dfrac{A}{d}$	
Cylindrical capacitor	$\dfrac{2\pi L}{ln\left(\dfrac{r_2}{r_1}\right)}$	
Spherical capacitor	$\dfrac{4\pi L}{(r_2 - r_1)}$	

C Results from three-arc based geometry estimation experiments

Table C.1: Results from test with target aligned at 0 degree to the barrier trolley.

Distance [m] p_{min}	Angle [deg] α	Coordinates of central arc center [m]		Central arc radius [m] r_{co}	Fillet arc radius [m] r_{fo}	width [m] w_o
		p_{ce}	x_{ce}			
24.8	0.000	0.069	26.090	1.298	0.378	1.616
24.4	0.000	0.064	25.770	1.386	0.215	1.503
24.0	0.000	0.084	25.331	1.365	0.226	1.539
23.4	0.000	0.198	24.965	1.540	0.297	1.668
23.0	0.000	0.087	24.499	1.493	0.315	1.668
22.6	0.000	0.009	24.106	1.519	0.311	1.668
22.0	0.000	0.054	23.541	1.507	0.332	1.668
21.6	0.000	0.039	23.070	1.465	0.341	1.668
21.0	0.000	0.062	22.496	1.457	0.359	1.679
20.5	0.000	0.101	21.918	1.435	0.364	1.679
20.0	0.000	0.054	21.376	1.423	0.371	1.679
19.4	0.000	0.056	20.805	1.417	0.372	1.679
19.0	0.000	0.036	20.386	1.416	0.342	1.643
18.5	0.000	0.040	19.957	1.411	0.341	1.643
18.0	0.000	0.047	19.384	1.409	0.343	1.643
17.6	0.000	0.056	18.970	1.405	0.351	1.650
17.0	0.000	0.025	18.424	1.401	0.354	1.650
16.5	0.000	0.024	17.870	1.396	0.358	1.650
16.0	0.000	0.051	17.444	1.390	0.361	1.650
15.5	0.000	0.055	16.855	1.374	0.371	1.656
15.0	0.000	0.026	16.428	1.375	0.373	1.656
14.5	0.000	0.041	15.866	1.373	0.375	1.656
14.1	0.000	0.054	15.448	1.372	0.371	1.648
13.5	0.000	0.036	14.907	1.368	0.374	1.648
13.0	0.000	0.011	14.368	1.368	0.374	1.648
12.5	0.000	0.026	13.832	1.374	0.389	1.666
12.0	0.000	0.021	13.403	1.373	0.390	1.666
11.6	0.000	0.018	12.966	1.371	0.392	1.666
11.0	0.000	0.035	12.396	1.371	0.373	1.642
10.4	0.000	0.020	11.827	1.370	0.375	1.642
10.0	0.000	0.022	11.417	1.369	0.376	1.642
9.5	0.000	0.020	10.886	1.371	0.382	1.647
9.0	0.000	0.010	10.340	1.371	0.384	1.647
8.5	0.000	0.008	9.928	1.372	0.385	1.647
8.0	0.000	0.010	9.361	1.375	0.399	1.661
7.5	0.000	0.007	8.928	1.376	0.400	1.661
7.0	0.000	0.014	8.365	1.378	0.401	1.661
6.4	0.000	0.013	7.815	1.379	0.402	1.661
6.0	0.000	0.008	7.410	1.379	0.403	1.661
5.5	0.000	0.002	6.871	1.378	0.389	1.645
4.9	0.000	-0.001	6.307	1.379	0.390	1.645
4.5	0.000	0.000	5.873	1.380	0.390	1.645
4.0	0.000	-0.003	5.447	1.380	0.388	1.642

Table C.2: Results from test with target aligned at -15 degree to the barrier trolley.

Distance [m] p_{min}	Angle [deg] α	Coordinates of central arc center [m]		Central arc radius [m] r_{co}	Fillet arc radius [m] r_{fo}	width [m] w_o
		p_{ce}	x_{ce}			
25.0	-15.526	5.883	25.791	1.477	0.372	1.655
24.5	-15.310	5.698	25.381	1.448	0.458	1.676
24.0	-14.980	5.430	24.822	1.402	0.543	1.760
23.5	-15.204	5.413	24.433	1.428	0.530	1.762
23.0	-15.301	5.318	23.882	1.422	0.538	1.762
22.5	-14.788	5.018	23.416	1.446	0.522	1.762
22.0	-15.392	5.125	22.927	1.430	0.529	1.765
21.5	-14.743	4.745	22.460	1.449	0.521	1.765
21.0	-14.817	4.656	22.043	1.449	0.515	1.765
20.5	-15.347	4.756	21.470	1.454	0.487	1.730
20.0	-14.854	4.454	20.950	1.427	0.493	1.730
19.5	-14.954	4.388	20.541	1.429	0.491	1.730
19.0	-15.033	4.259	19.974	1.414	0.474	1.704
18.5	-15.011	4.193	19.557	1.418	0.477	1.704
18.0	-14.901	4.025	19.012	1.414	0.475	1.702
17.5	-14.925	3.896	18.467	1.412	0.476	1.702
17.0	-14.966	3.817	18.070	1.409	0.474	1.702
16.5	-15.171	3.729	17.527	1.409	0.469	1.695
16.0	-15.121	3.639	16.984	1.404	0.469	1.695
15.5	-15.242	3.542	16.562	1.404	0.468	1.695
15.0	-15.035	3.372	16.010	1.396	0.487	1.715
14.5	-15.445	3.364	15.569	1.393	0.485	1.715
14.0	-15.303	3.212	15.025	1.384	0.486	1.715
13.5	-15.177	3.103	14.634	1.380	0.494	1.722
13.0	-15.243	2.984	14.102	1.373	0.496	1.722
12.5	-15.173	2.834	13.580	1.371	0.486	1.708
12.0	-15.222	2.746	13.157	1.368	0.486	1.708
11.5	-15.090	2.551	12.605	1.372	0.486	1.708
11.0	-15.504	2.572	12.168	1.368	0.481	1.701
10.5	-15.447	2.431	11.632	1.370	0.481	1.701
10.0	-15.561	2.322	11.098	1.369	0.480	1.701
9.5	-15.466	2.209	10.715	1.370	0.471	1.692
9.0	-15.223	2.035	10.183	1.369	0.470	1.692
8.5	-15.077	1.914	9.777	1.370	0.470	1.692
8.0	-14.978	1.767	9.220	1.370	0.459	1.680
7.5	-15.424	1.740	8.797	1.370	0.459	1.680
7.0	-14.869	1.537	8.282	1.372	0.458	1.680
6.5	-14.788	1.383	7.753	1.373	0.458	1.680
6.0	-15.336	1.370	7.342	1.374	0.457	1.680
5.5	-15.298	1.239	6.798	1.375	0.455	1.678
5.0	-15.260	1.108	6.245	1.376	0.455	1.678
4.5	-15.288	1.006	5.826	1.377	0.454	1.678
4.0	-14.992	0.882	5.425	1.378	0.461	1.687

Table C.3: Results from test with target aligned at -45 degree to the barrier trolley.

Distance [m] p_{min}	Angle [deg] α	Coordinates of central arc center [m]		Central arc radius [m] r_{co}	Fillet arc radius [m] r_{fo}	width [m] w_o
		p_{ce}	x_{ce}			
25.0	-45.174	17.418	20.100	1.660	0.443	1.789
24.5	-45.027	17.041	19.734	1.562	0.453	1.727
24.0	-44.957	16.608	19.244	1.473	0.509	1.747
23.6	-45.296	16.399	18.778	1.404	0.534	1.747
23.0	-45.115	16.019	18.482	1.453	0.523	1.747
22.5	-45.081	15.584	18.083	1.430	0.526	1.747
22.0	-45.223	15.330	17.731	1.418	0.530	1.746
21.5	-45.349	14.998	17.274	1.401	0.537	1.746
21.0	-45.385	14.741	16.977	1.414	0.536	1.746
20.5	-45.092	14.337	16.644	1.425	0.511	1.721
20.0	-45.132	13.870	16.213	1.419	0.515	1.721
19.5	-45.349	13.720	15.883	1.439	0.507	1.721
19.0	-45.223	13.256	15.540	1.449	0.525	1.745
18.5	-45.086	12.888	15.264	1.440	0.528	1.745
18.0	-45.214	12.597	14.836	1.446	0.527	1.745
17.6	-45.262	12.261	14.510	1.444	0.522	1.738
17.0	-45.304	11.910	14.088	1.442	0.524	1.738
16.5	-45.429	11.593	13.654	1.447	0.504	1.712
16.0	-44.832	11.151	13.490	1.443	0.506	1.712
15.5	-45.224	10.864	13.010	1.443	0.508	1.712
15.0	-45.060	10.449	12.647	1.451	0.499	1.702
14.5	-45.005	10.114	12.347	1.450	0.500	1.702
14.0	-45.121	9.770	11.905	1.452	0.501	1.702
13.5	-45.639	9.579	11.513	1.451	0.485	1.682
13.0	-45.215	9.124	11.175	1.447	0.487	1.682
12.5	-45.180	8.744	10.794	1.446	0.486	1.682
12.0	-44.967	8.414	10.524	1.442	0.474	1.666
11.5	-44.967	8.027	10.123	1.439	0.475	1.666
11.0	-44.908	7.735	9.813	1.437	0.476	1.666
10.5	-44.873	7.337	9.393	1.434	0.469	1.657
10.0	-45.296	7.128	9.032	1.435	0.469	1.657
9.5	-45.260	6.738	8.633	1.435	0.466	1.654
9.0	-45.206	6.348	8.247	1.433	0.466	1.654
8.5	-45.306	6.080	7.943	1.432	0.465	1.654
8.0	-45.207	5.690	7.549	1.431	0.463	1.651
7.5	-45.445	5.340	7.108	1.429	0.462	1.651
7.0	-45.245	5.013	6.817	1.428	0.461	1.651
6.5	-45.219	4.623	6.408	1.426	0.462	1.652
6.0	-45.339	4.350	6.100	1.426	0.462	1.652
5.5	-45.079	3.955	5.724	1.424	0.462	1.652
5.0	-45.102	3.581	5.323	1.423	0.462	1.652
4.5	-45.254	3.301	5.003	1.423	0.461	1.652
4.0	-45.059	2.889	4.593	1.423	0.454	1.642

D Description of finite element model for occupant simulations

This section explains the finite element model used for occupant level simulations. The steps in which the complete model is created are explained below in detail. The occupant level simulation model consisted of the vehicle sled model, dummy model, and restraint systems (seatbelt with a retractor, driver airbag, and side curtain airbag). The mentioned models were created separately and merged to create a complete occupant model.

D.1 Vehicle sled model

As described in Subsection 5.3.2 the 2010 Toyota Yaris coarse finite element model was used as a vehicle sled model. Contrary to the vehicle model in vehicle simulations, only the vehicle interior parts were considered in the occupant model. The vehicle parts which will not make any contact with the dummy during a crash scenario were eliminated to simplify the vehicle sled model. Figure D.1 displays the vehicle sled model used to create the occupant model.
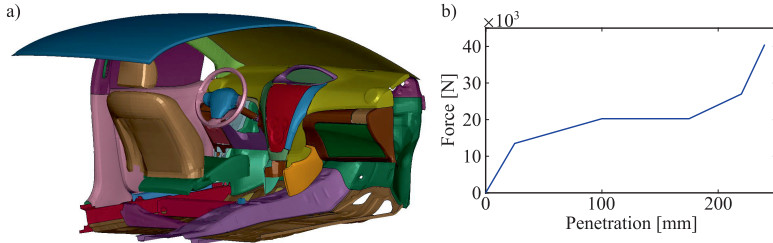
Figure D.1: Details of vehicle model: a) vehicle sled model and b) force-penetration curve.

The material card of the driver seat parts seat used in the vehicle model was changed to rigid material so that rigid body one-way contact could be used for the dummy to seat contact. With this type of contact, the dummy parts can penetrate the seat surfaces but are held together by the force-penetration curve (see Figure D.1b). The reason to use such type of contact is to reduce the simulation time by not requiring detailed modeling of the foam, springs, and other complicated parts with complex material properties. The deformation behavior of the seat part is defined by the force-penetration curve and hence this method summarizes the overall behavior of dummy-seat interaction to the required detail.

Table D.1: Coordinates for occupant positioning

Description	Coordinates by NHTSA			Transformed coordinates		
	x	y	z	x'	y'	z'
Head CG	2164.878	-412.787	-728.488	-2094.622	412.787	1286.53
Tip of nose	2261.45	-333.939	-680.328	-1998.05	333.939	1161.998
Tip of chin	2256.11	-333.158	-603.956	-2003.39	333.158	1161.998
H point	2311.02	-530.484	-32.7692	-1948.48	530.484	590.8112
Left knee	2694.393	-559.711	-185.598	-1565.107	559.711	743.64
Left ankle	2963.45	-548.03	134.6526	-1296.05	548.03	423.3894
Left heel	2973.302	-535.87	276.0135	-1286.198	535.87	282.0285

D.2   Dummy model

The Hybrid III 50th percentile male fast dummy model provided by Livermore Software Technology (LST), an Ansys company was adapted and used for the occupant simulations. The original dummy was positioned by applying the positioning coordinates provided by NHTSA [158]. The position provided by NHTSA was implemented during the full-scale crash test of the 2011 Toyota Yaris model at 56 km/h. The coordinate system considered in the crash test by the NHTSA was different than the coordinate system applied in this work. In the coordinate system used in the NHTSA report, the rearmost center of the top of the rear bumper beam was considered as a reference point. The x, y, and z axes were directed from the rear to front, left to right, and top to bottom of the vehicle respectively. However, in this work, the point near the center of the front bumper beam was considered a reference point. The x-axis direction was similar to that applied by NHTSA while the y and z axes were directed from the right to left and bottom to top of the vehicle respectively. Hence initially the coordinates provided by the NHTSA were transformed into the required coordinate system, and then the dummy was positioned using modified coordinates. Table D.1 lists the coordinates given in the NHTSA report and the transformed coordinates. Figure D.2a shows the original position of the dummy model while Figure D.2b shows the dummy model positioned by applying the modified coordinates.

D.3   Restraint systems

Seatbelt with retractor: The seatbelt model having a combination of a 1-D beam type and a fabric belt (2-D shells) as shown in Figure D.3a was considered for the occupant level simulations. The seatbelt was re-routed over the positioned dummy using the guidelines provided by LST. The sensor fire time of the seatbelt retractor is set at 1 ms in the model. This time is not the same at which the retractor locks. After the sensor firing time (i.e. 1 ms) the slack in the belt depending on the velocity of the occupant is removed and the retractor locks up and
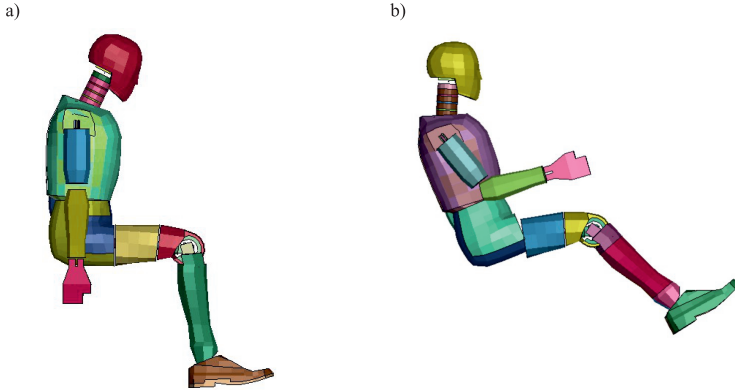
Figure D.2: Dummy model: a) original position and b) modified position.

spools out the belt based on the force-payout curve. The maximum force value is maintained at 3.25 kN. Figure D.3b displays a retractor force-payout curve with a load limited to 3.25 kN.
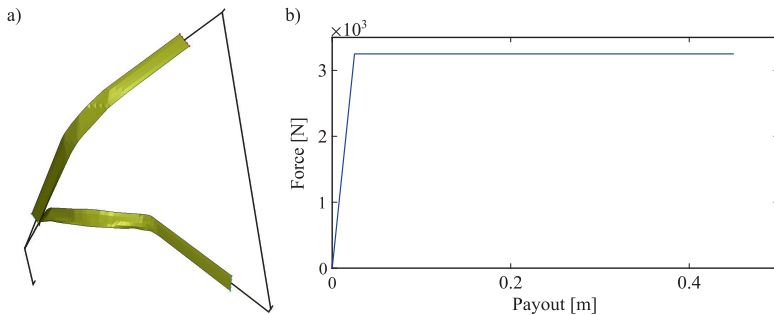

Figure D.3: Details of seatbelt model: a) seatbelt with retractor and b) retractor force-payout curve.

Driver airbag: The driver airbag model developed for the Honda Accord mid-size sedan by NHTSA was employed in the occupant simulations [158]. The model was created with a 5 mm element size using scanned CAD to get accurate deployment and smooth contact and folded using DynaFold simulations. The airbag model was then mounted into the steering wheel. Figure D.4 shows the finite element model of the driver airbag.
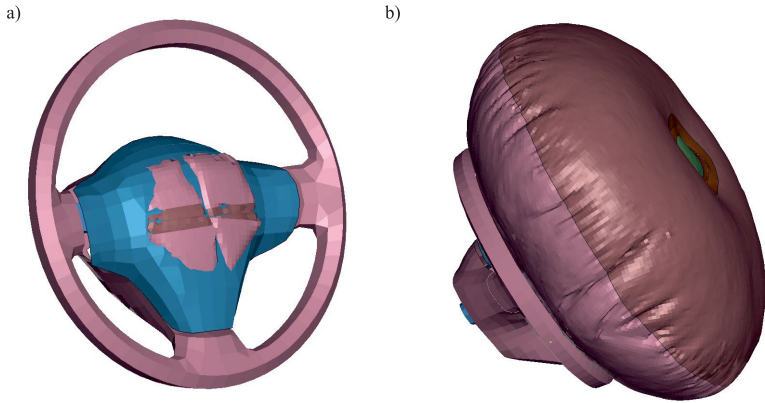
Figure D.4: Driver airbag model: a) airbag folded into the steering and b) fully inflated airbag.

Curtain airbag: The side curtain airbag model with impactor provided by ABAQUS Inc. [159] was adapted and converted into the LS-Dyna compatible model. Figure D.5a shows the folded curtain airbag model, while Figure D.5b shows the fully inflated curtain airbag.
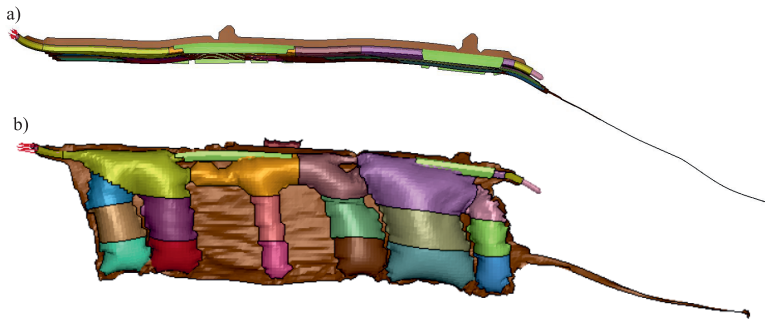
Figure D.5: Curtain airbag model: a) airbag after folding and b) fully inflated airbag.

Before including the model into the occupant model, the conversion of the model from ABAQUS software to the LS-Dyna software was validated. To validate the model, the available airbag model was first simulated in ABAQUS and

corresponding velocity and acceleration profiles of the impactor were recorded (see Figure D.6). The converted FEM model was simulated under similar loading conditions in LS-Dyna and the velocity and acceleration profiles of the impactor were compared with those extracted through simulations in ABAQUS.
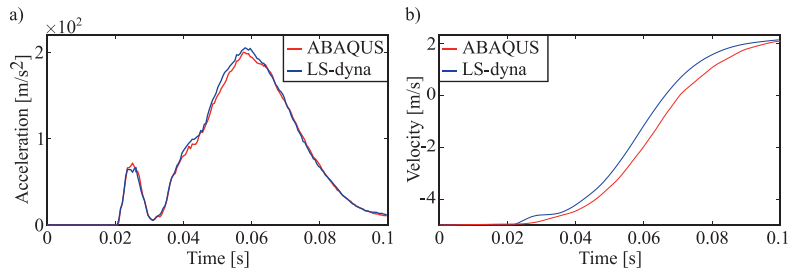
Figure D.6: Results from the validation of curtain airbag conversion: a) impactor acceleration comparison and b) impactor velocity comparison.

E Methodology for calculation of the projected overlap

Overlap is a common term used as a parameter for specifying the different standard crash tests such as moderate overlap and small overlap crash tests. Overlap in terms of vehicle crashworthiness can be visualized as the projection of the opponent-object on the ego-vehicle normalized to the width of the ego-vehicle. Thus, the overlap o in percentage is given by the following equation.

$$o = \frac{d}{w_{ego}} \cdot 100, \tag{E.1}$$

where, d is the projected length on the ego vehicle at t_0 (see Figure E.1) and w_{ego} is the width of the ego-vehicle. For the estimation of d during the calculation of the o, three reference lines are considered. Reference line 1 is the projection of one side of the opponent-vehicle. For positive α, the side closer to the passenger is considered for projection while for negative α, the side closer to the driver is considered. Reference line 2 is parallel to the longitudinal direction of the ego-vehicle and tangent to the front contour of the opponent-vehicle at the side which was not considered for reference line 1. The third reference is a line projected from the side of the ego-vehicle. In the case reference line concerning ego-vehicle, the side closer to the driver is considered for positive α and vice-versa. For estimating d, the point where the reference line 1 intersects on the ego-vehicle is considered, from this point the smallest distance parallel to the width of the ego-vehicle up to the reference line 2 and line 3 is considered as the value for d. For the investigations in Chapter 5, this distance was calculated from the nodes FEM-model of the vehicle for each of the simulation cases to be considered as an additional input feature.
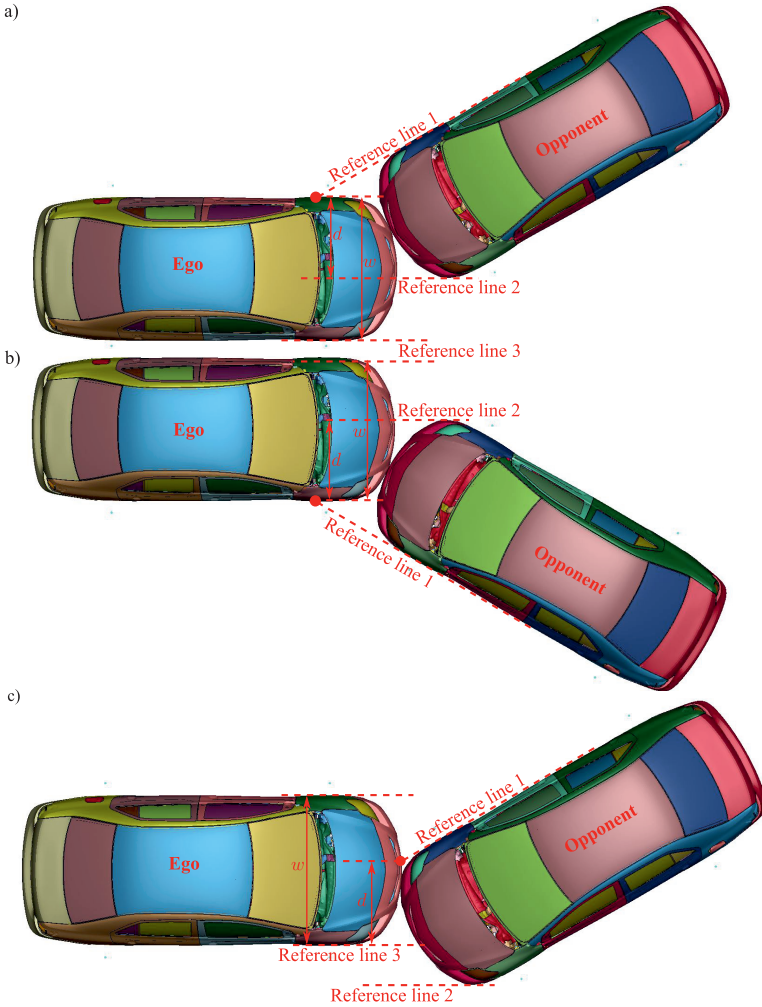
Figure E.1: Different scenarios for calculating the projected overlap: a) a scenario with positive p and α, b) a scenario with negative p and α, and c) a scenario with positive p and negative α,

Curriculum Vitae

This page is only available in the print version due to the regulations of the Otto-von-Guericke University

VDI verlag

Alle 23 Reihen der „Fortschritt-Berichte VDI"
in der Übersicht – bequem recherchieren unter:
elibrary.vdi-verlag.de

Und direkt bestellen unter:
www.vdi-nachrichten.com/shop

VDI

REIHE 12
VERKEHRSTECHNIK/
FAHRZEUGTECHNIK

BAND
1|1

VOLUME
1|1